Electron microscopy of sharp edges and corners coated by ion-assisted PVD

Eva Macak

A thesis submitted in partial fulfilment of the requirements of Sheffield Hallam University for the degree of Doctor of Philosophy

June 2003

Abstract

The thesis examines ion-assisted physical-vapour deposition (PVD) of thin coatings on non-flat three-dimensional samples, concentrating on the case of free-standing edges and corners. Changes in the electric field in the vicinity of sharp edges lead to local changes in the ion bombardment (ion flux and angle of incidence) which can significantly affect the ion-surface interaction and thus the properties and the performance of the coatings growing in the edge region. This work presents a detailed electron microscopy study of the edge-related changes in the coating properties and develops a physical model to explain and quantify the effects. The problem is studied on a system typical for industrial coating of cutting tools used in dry high speed cutting: TiAlN-type coatings (TiAlN/VN and TiAlCrYN) deposited on wedge-shaped samples by closed-field unbalanced magnetron sputtering (UBM), using high-flux, low-energy Ar^+ ion irradiation ($J_i/J_{me} \sim 4$, $E_i = 75\text{-}150$ eV). The morphology and composition of the coatings in the edge region, as a function of the edge geometry (angle and radius of curvature) and the deposition conditions (substrate bias), is studied using scanning electron microscopy combined with energy-dispersive X-ray spectroscopy (SEM+EDX). The internal structure of the coatings growing on sharp edges is examined by transmission electron microscopy (TEM). A detailed theoretical analysis of the effects, based on the simulations of the plasma sheath around the samples and the resulting ion bombardment distribution, is presented. A direct relationship between the experimentally observed magnitude and spatial extent of the changes in the edge region and the simulated characteristics of the plasma sheath around the edges is shown.

Advanced Studies

The following international conferences and research seminars were attended during the course of the PhD:

1.) European Material Research Society Meeting (E-MRS 2001), Strasbourg, France, June 2001. The presentation given received a 'Young Scientist Award'.

2.) ABS Days 2001, Sheffield, UK, July 2001. A presentation was given.

3.) Electron Microscopy and Analysis Group Meeting (EMAG 2001), organised by the Institute of Physics, Dundee, Scotland, September 2001. A presentation was given.

4.) ABS Days 2002, Sheffield, UK, July 2002. A presentation was given.

5.) MRI Seminar, July 2001. A presentation was given.

6.) MRI Research Days 2001, January 2001. A poster was presented.

7.) MRI Research Days 2002, January 2002. A poster, awarded by a prize, was presented.

The major part of the experimental work presented in this thesis was done at the Materials Research Institute at Sheffield Hallam University. The FIB sample preparation, as well as some of the TEM analysis, were performed at the Department of Materials at Oxford University.

Scientific publications

1.) E.B.Macak, W.-D.Münz, J.M.Rodenburg,
Plasma-surface interaction at sharp edges and corners during ion-assisted PVD, PART I: Edge-related effects and their influence on coating morphology and composition.
Accepted for publication in Journal of Applied Physics.

2.) E.B.Macak, W.-D.Münz, J.M.Rodenburg,
Plasma-surface interaction at sharp edges and corners during ion-assisted PVD, PART II: Enhancement of the edge-related effects at sharp corners.
Accepted for publication in Journal of Applied Physics.

3.) E.B.Macak, W.-D.Münz, J.M.Rodenburg,
Electron microscopy studies of hard coatings deposited on sharp edges by combined cathodic arc/unbalanced magnetron PVD.
Surface and Coatings Technology 151-152 (2002) 349-354.

4.) E.B.Macak, W.-D.Münz, J.M.Rodenburg,
Quantitative EDX-analysis of PVD hard coatings deposited on sharp edges.
Institute of Physics Conference Series No.168 (2001) 345-348.

5.) E.B.Macak, W.-D.Münz, J.M.Rodenburg,
Ion-assisted PVD on sharp edges and the implications for coating of cutting tools.
Materials Week 2002 proceedings.

6.) E.B.Macak, W.-D.Münz, J.M.Rodenburg,
Edge-related effects during ion-assisted PVD on sharp edges and their implications for coating of cutting tools.
Surface Engineering Vol. 19, No. 3. (2003) - in press

7.) E.B.Macak, J.M.Rodenburg,
Internal structure of TiAlN/VN coating deposited on sharp edges
In manuscript.

8.) J.M.Rodenburg, E.B.Macak,

Optimising the resolution of TEM/STEM with electron Ronchigram.

Microscopy and Microanalysis Issue 90 (July 2002) 5-7.

Acknowledgements

I would like to thank Prof. J. M. Rodenburg for his excellent guidance, support and inspiration throughout the whole course of my PhD.
I would like to thank Prof. W.-D. Münz for giving me the opportunity to do my PhD at MRI and for sharing his industrial knowledge and experience.

For helping me with the experimental work, my thanks go to Dr. R. Langford for the FIB TEM sample preparation, to Dr. P. Eh. Hovsepian for performing the coating depositions and Mr. G. Robinson for the machining of the wedge-shaped samples and performing the cutting tests. My further thanks belongs to the technical staff at MRI for their help in solving experimental problems.

The financial support of EPSRC grant agency (grant nr.2993), which enabled the research work presented in this thesis, is greatly acknowledged.

I would like to use this occasion to thank also all the teachers who, throughout my education, contributed to my knowledge and enabled me to see unknown things.

My most special thanks belong to my family, without whose love and support this thesis would have never been possible.

Contents

Chapter 1: Introduction

Ion-assisted physical vapour deposition (PVD) is a common industrial method for growing thin coatings of various interstitial nitride alloys for a wide range of applications. This type of PVD growth allows the synthesis of dense coatings at temperatures substantially lower than their melting temperature (the deposition temperature is typically between 300 and 500°C), which is crucial for many applications. However in order to obtain an acceptable quality of coatings at these low temperatures, the thermal energy required for creation of dense structures has to be substituted by ion irradiation of the growing film, which increases adatom mobility. This is most frequently achieved by plasma assisted PVD techniques such as magnetron sputtering, arc evaporation or ion plating. Necessarily, it introduces a direct relationship between the properties of the coatings and the characteristics of the ion bombardment - a relationship studied extensively during the last three decades for flat surfaces (for a review, see for example Greene, 1988).

In practical applications, three-dimensional objects containing sharp edges and corners have often to be coated uniformly. In such a case the interaction between the ions and the surface will however be different than in the case of flat samples. Despite the fact that this could significantly affect the coatings, only few related reports are published, with no detailed explanation or quantification of the effects. In industry, empirical optimisation of the deposition conditions is often done in order to decrease the unwanted effects, often compromising however on other requirements. Our research was stimulated by problems encountered during magnetron deposition of TiAlN-type coatings on industrially used cutting tools, where visible changes in the colour and homogeneity of the coatings in the cutting edge region have been observed for negative substrate biases of more than 100V (Münz, 2003). For this reason, a relatively low negative bias voltage value of ~75V is commonly used, even though increase in the deposition bias in the case of flat substrates was shown to lead to increased hardness of the coatings (Hakansson, 1987). Until the present work, no detailed examination of the coatings on the cutting edges was however done.

The work presented in this thesis examines ion-assisted PVD of thin coatings on non-flat three-dimensional samples, concentrating on sharp edges and corners. Our aim

is to establish a physical model which explains the edge-related effects and allows quantification of their spatial extent and magnitude as a function of the edge geometry and the deposition conditions. This is achieved by combining detailed electron microscopy study of the changes in the coating properties with theoretical modelling of plasma-surface interaction in the edge region.

We focus on the interaction between the samples and the plasma inside the deposition chamber. During the deposition the samples are surrounded by a region called the plasma sheath - a transition region between the quasi-neutral plasma confined inside the chamber and the negatively biased samples. The potential difference across the sheath accelerates positively charged ions from the plasma to the samples and is thus directly related to the energy of the ion bombardment. The shape of the plasma sheath - which is connected to the shape of the samples - determines the ion flux distribution which in turn affects the coating properties.

The effects are studied on a system typical for the cutting tool industry: TiAlN-type coatings deposited on sharp edges by closed-field unbalanced magnetron sputtering (UBM). Wedge-shaped samples were chosen as a simple model which would represent the real cutting edge and would allow us to change easily the edge angle. The coatings were growing under high flux low energy Ar^+ ion irradiation ($J_i/J_{me} \sim 4$, E_i = 75 - 150 eV - where J_i/J_{me} is the ion-to-metal flux density ratio at the substrate and E_i is the ion energy). The analysis was performed using scanning and transmission electron microscopy (SEM and TEM), combined with energy-dispersive X-ray compositional analysis (EDX).

The material presented in the thesis is organised into 8 chapters:

Chapter 2 describes the plasma present in PVD processes and its interaction with the samples. The research work related to ion characteristics and their effect on the properties of coatings, on both - flat and non-flat surfaces, is reviewed.

Chapter 3 presents the experimental details related to the fabrication of the samples and their analysis by electron microscopy. We also analyse the problems we had to solve during the compositional analysis.

In Chapter 4 we analyse, by means of SEM, the changes in the morphology and composition of the coatings observed in the edge region of the wedges. We examine the influence of the edge geometry and of the substrate bias used during the deposition.

In Chapter 5 we establish a model explaining the observed effects. We show the direct relationship between the characteristics of the plasma sheath, which are simulated, and the magnitude and spatial extent of the changes in the edge region observed in Chapter 4.

Chapter 6 uses TEM in order to examine the internal microstructure of the coatings, concentrating on the region right on top of the edges. The observations are connected with the ion characteristics calculated in Chapter 5.

Chapter 7 discusses the effects from the point of view of practical applications. The predictions of our model are verified on industrially-used cutting tools. We discuss the importance of the effects in common ion-assisted PVD techniques and outline the possibility for further optimisation of the deposition conditions.

Finally, Chapter 8 summarises the most important results of this work.

Chapter 2: The role of ion bombardment during ion-assisted PVD (literature review)

Ion bombardment during coating depositions is used in order to improve the coating properties. Its presence, however, introduces problems when coating 3-dimensional objects. Different electric field distributions around biased flat and non-flat surfaces will affect the characteristics of the ions drawn from the plasma towards the samples and thus the interaction between the ion and the growing coating. The problem is especially important for sharp edges and corners which strongly disturb the electric field. In this chapter we first examine the electric field distribution and its effect on the ion trajectories and distribution in the case of flat and of free-standing wedge-shaped samples, starting with the simplest case of electric field in vacuum and then examining the more complicated plasma environment present in ion-assisted PVD. We then review the relationship between the characteristics of the ion bombardment and the properties of the coatings.

2.1. The electric field around a biased object immersed into plasma

2.1.1. Flat samples

The ion bombardment used during coating depositions is most commonly generated by immersing the samples into a plasma. The plasma model presented in this section is valid for weakly ionised low pressure discharges - which represents well the conditions typically found in the vicinity of objects treated by PVD, far away from the plasma source. The plasma surrounding the samples inside a deposition chamber can, as all plasmas, be characterised by a common charged particle density $n_o \approx n_e$ (electrons) $\approx$ n_i (ions) [particles/m^3] and ion and electron temperature - T_i, T_e [eV]. Because these discharges are electrically driven and are weakly ionised (the plasma density is only a small fraction of the neutral gas density - less than 10^{-3}), the applied power preferentially heats the mobile electrons, while the heavy ions efficiently exchange energy by collisions with the background gas - hence for these plasmas $T_e >> T_i$. Typical value of T_e used in low pressure discharges is T_e = 1-10 eV and T_i is two order

of magnitude lower: $T_i = 0.05 - 0.5$ eV (Lieberman, 1994). Typical particle density n_o is in the range $n_o \approx 10^8 - 10^{13}$ cm^{-3}. The characteristics of the PVD plasmas compared with other types of plasmas are shown in Fig.2-1.

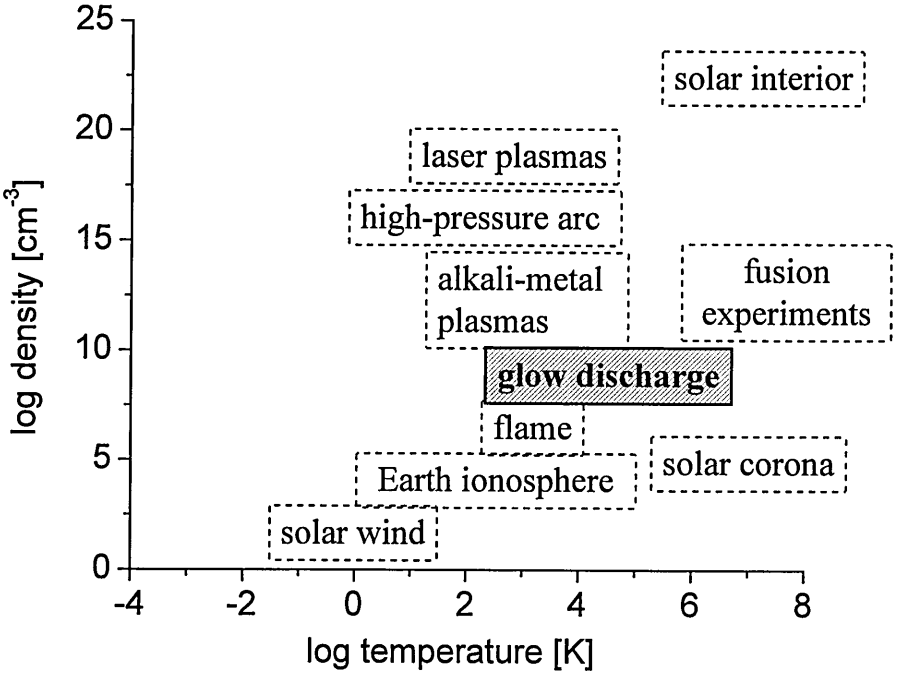

Fig.2-1: The wide range of space and laboratory plasmas compared to the low pressure glow discharge. The plasmas are classified according to the two characteristic parameters - the particle density and the electron temperature (1 eV ≅ 11 600 K).

Let us consider plasma confined between two grounded absorbing walls. On a very short timescale, part of the fast moving electrons will be rapidly lost to the walls, which means that the region close to the wall will be electron-depleted. This establishes a thin positively charged transition layer between the quasineutral plasma and the grounded walls - called the plasma sheath - which acts as a barrier for the mobile electrons. Conversely, ions that enter the sheath will be accelerated towards the walls. The potential inside the sheath thus allows the flow of the positive and the negative carriers to the wall to be balanced. The value of the plasma potential relative to the walls - U_p - is of the order of few T_e in order to confine most of the electrons.

In weakly ionised plasma processes, the energy to sustain the plasma is given by heating the electrons by a source. As these energetic electrons are drifting away from

the source, they are subjected to numerous collisions within the bulk plasma - which leads to a Maxwellian-type electron energy distribution. The density of the electrons will therefore be decreasing exponentially towards the negatively biased walls. The density distribution of the electrons inside the sheath is given by the Boltzman's relation:

$$n_e = n_o e^{\Phi/T_e} . \qquad \text{(Eq.2-1)}$$

The bombarding ions on the other hand can be considered as monoenergetic particles, as their initial energy is very low and their mean free path is large compared to the sheath dimensions. They are accelerated towards the negatively biased walls, thus their density within the sheath is (slightly) decreasing towards the walls. They hit the walls with energy given by the potential difference between the plasma and the walls, which in the case of grounded walls, is U_p. During ion-assisted PVD the samples immersed into plasma are often negatively biased in order to increase the energy of the bombarding ions, and thus affect the properties of deposited layers (the relationship is discussed in section 2.2.). If a negative substrate bias U_b (much larger than U_p) is applied, the energy of all the bombarding ions is $eU_p + eU_b \approx eU_b$.

The electromagnetic field is described by the Maxwell's equations. In the case of negligible time variation of the magnetic field, the electric field is equal to a gradient of a scalar potential ϕ ($\mathbf{E} = -\nabla\Phi$ since $\nabla \times \mathbf{E} = 0$) which combined with the other Maxwell's equation for the electric field ($\nabla \cdot \mathbf{E} = \rho/\varepsilon_o$) gives the basic equation relating the spatial variation of an electric field to the existing space charge density distribution ρ - the Poisson's equation:

$$\nabla^2\Phi = -\frac{\rho}{\varepsilon_o} . \qquad \text{(Eq.2-2)}$$

In the approximation that there are no collisions inside the sheath and that the initial ion energy (and T_e) is low compared to the applied potential (collisionless Child-Langmuir sheath model - Child, 1911 and Langmuir, 1913), the solution of Poisson's equation combined with the equations for ion energy and ion flux conservation gives the following potential, electric field and ion density distribution across the sheath:

$$\Phi = -U_b\left(\frac{x}{s}\right)^{4/3} , \qquad \text{(Eq.2-3)}$$

$$E = \frac{4}{3}\frac{U_b}{s}\left(\frac{x}{s}\right)^{1/3}, \qquad \text{(Eq.2-4)}$$

$$n_i = \frac{4}{9}\frac{\varepsilon_o U_b}{es^2}\left(\frac{x}{s}\right)^{-2/3}. \qquad \text{(Eq.2-5)}$$

The parameter s is the plasma sheath width equal to:

$$s = \left(\frac{2^{5/4}}{3}\right)\left(\frac{\varepsilon_o}{e}\right)^{1/2}\left(\frac{U_b^{3/4}}{T_e^{1/4} n_s^{1/2}}\right), \qquad \text{(Eq.2-6)}$$

where n_s is the ion density at the sheath boundary. The ion and electron densities, electric field and potential profiles inside a typical plasma sheath are presented in Fig.2-2b.* The plasma sheath region being electron depleted, there are many fewer electrons to excite the gas than in the plasma and the sheath therefore appears as dark when observed visually. Hence the sheath is sometimes denoted also as 'dark space'.

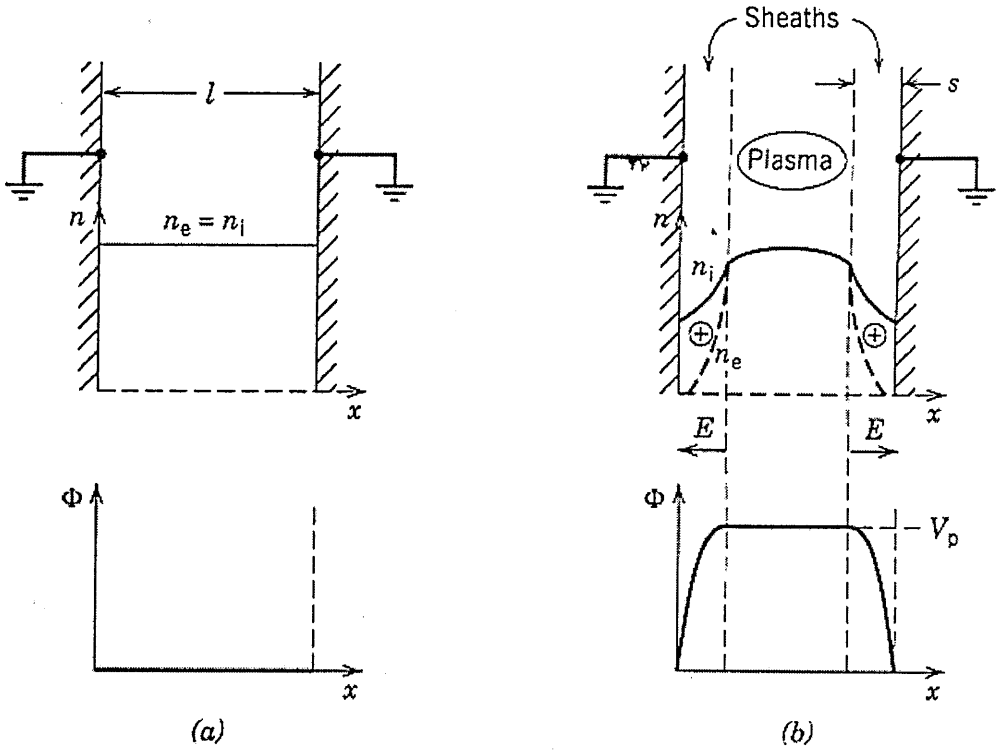

Fig.2-2: Formation of the plasma sheath: (a) initial ion and electron densities and potential; (b) densities, electric field, and potential after the sheath is established. (Taken from Lieberman, 1994.)

* As will be shown later, the typical sheath width relevant to this study was on the scale of ~1 mm.

2.1.2. Non-flat samples

Let us first consider the case of a biased edge in vacuum. The electric field in the proximity of a sharp edge or a corner can be can be calculated as the electric field close to two conducting planes intersecting at an angle α ($\alpha < 2\pi$). In vacuum, where $\rho = 0$, the corresponding Poisson's equation (in this case called Laplace's equation) can be solved analytically. The solution is a complex function which close to the edge ($r \rightarrow 0$) simplifies to:

$$E(r) \approx (-c/\beta) \times r^{(\pi/\beta)-1}, \qquad \text{(Eq.2-7)}$$

where $\beta = (2\pi - \alpha)$ and c is a constant dependent on the boundary conditions (Jackson, 1999). The electric field around a wedge-shaped sample with wedge angle α varies thus with the distance from the edge as:

$$E(r) \propto r^{(\frac{\pi}{2\pi-\alpha})-1}, \qquad \text{(Eq.2-8)}$$

which gives:

$E \propto r^{-1/2}$, for $\alpha \rightarrow 0$;

$E \propto r^{-1/3}$, for $\alpha = \pi/2$;

$E \propto r^{-3/7}$, for $\alpha = \pi/4$;

$E = const$, for $\alpha = \pi$ (flat surface);

$E \propto r$, for $\alpha = 3\pi/2$.

For convex edges ($\alpha < \pi$), the electric field close to the edge (which means for small r) is stronger than for flat samples ($\alpha = \pi$), while for concave samples ($\alpha > \pi$), it is weaker. The electric field around an edge thus depends on the edge geometry, and the applied substrate bias which determines the constant c.

The formulas derived above can help us to qualitatively understand the shape of the plasma sheath, which is governed by the electric field distribution (the field in the sheath region close to the samples being similar to that in vacuum). For wedge-shaped samples, the density of the potential lines close to the edge is higher (that is, the electric field is stronger) than above flat sample, which means that the plasma sheath will be contracted towards the edge. The density of the lines close to a groove is, on the other

hand, lower and the sheath will be dilated away from the edge. The three different situations are drawn schematically in Fig.2-3.

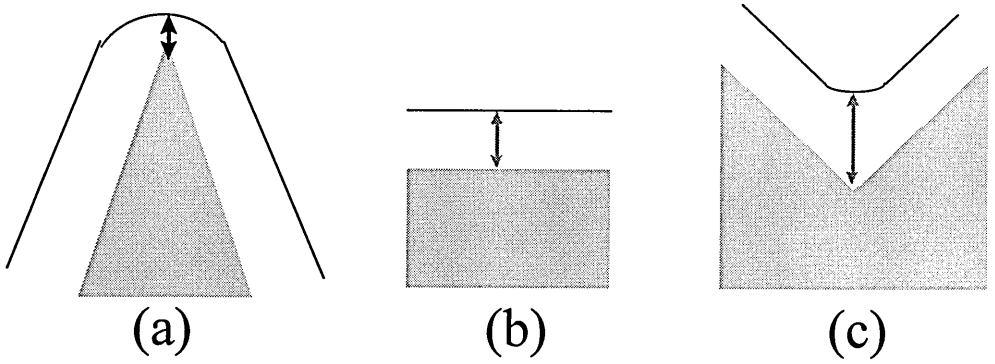

Fig.2-3: Schematic representation of the plasma sheath around samples of different geometries: the sheath is contracted towards a convex surface, and is dilated from a concave surface.

In the simplest case of an infinite flat surface immersed into the plasma the electric field can be calculated analytically - it is the Child-Langmuir sheath discussed in section 2.1.1. The complexity of the Poisson's equation in the case of non-flat surfaces in plasma means however that the solution for the potential Φ must even in the simplest case of a spherical surface be found numerically (the density of the ions on the right side of the Poisson's equation being a complicated integral involving Φ).

The problem of spherical and cylindrical objects in plasma is the basis of the plasma probe characterisation technique (analysed for example by Chen, 1965), which uses thin metal wires immersed into plasma in order to examine the characteristics of the medium. Here, under conditions of low-pressure discharges, the current collected by the probe is a function of the potential difference between plasma and the probe (Langmuir equation - Langmuir, 1926), and the characteristics of the plasma such as ion and electron density can thus be determined without the knowledge of the exact spatial distribution of the potential $\Phi(x)$. The comparison of ion currents collected by flat and by cylindrical probes have however established two important characteristics of the ion motion across a curved sheath: an increase in the ion flux entering the sheath and the possibility of non-perpendicular angle of incidence of the ions (see Fig.2-4.).

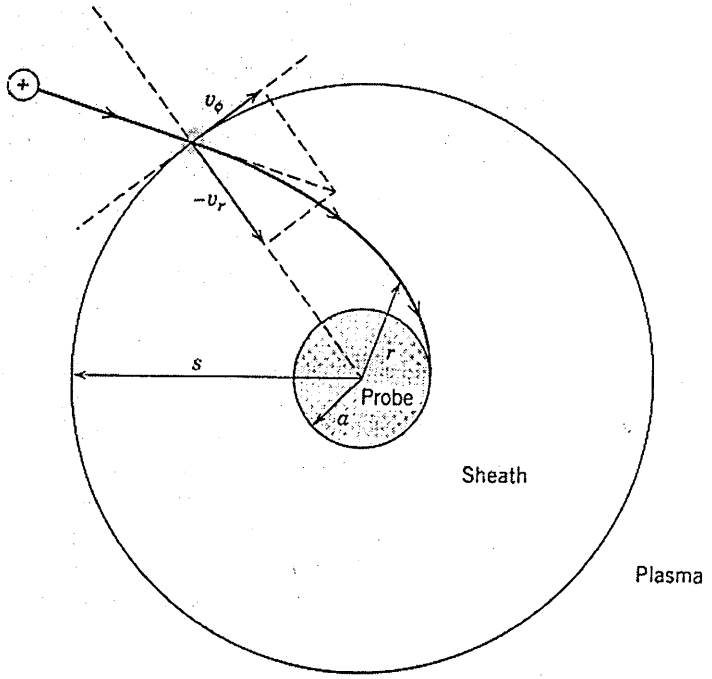

Fig.2-4: Ion orbital motion within the sheath of a cylindrical Langmuir probe. (Taken from Lieberman, 1994.)

Numerical calculations of the potential distribution around non-flat objects immersed into plasma have been done in the last 15 years in the field of plasma immersion ion implantation (PIII). This emerging technique allows the possibility of versatile surface modification of metals, semiconductors, ceramics and polymers. By applying negative high-voltage pulses to the substrates, immersed in a plasma, positive ions are extracted from the plasma, accelerated to the surface and implanted into the near-surface layer. The technique was developed to circumvent the line-of-sight restrictions of conventional beam-line implantation, as, when immersed into plasma, even complex three-dimensional objects are bombarded from all sides simultaneously which allows rapid cost-effective treatment. The problem of non-uniformity of ion dose near sharp edges and corners has, however, soon arisen, and because the treatment of such objects is the main advantage of the technique, it lead to both theoretical and experimental work examining the characteristics of the plasma sheath around non-planar surfaces.

Numerical simulations of the steady state Child-Langmuir sheath around free-standing wedge-shaped objects were performed by Watterson (1989). The work

numerically calculates the potential distribution around a square ($\alpha = 90°$) and a knife edge ($\alpha \rightarrow 0°$) from Poisson's equation coupled with the motion of the ions across the sheath. The calculations are done in dimensionless form which allows scaling of the results to a particular set of parameters such as substrate bias or plasma density. The results shows the contraction of the plasma sheath towards the edges due to stronger electric field in the region and its effect on the ion trajectories across the sheath. The non-uniformity of the plasma sheath is shown to cause a continuous change of the angle of incidence of the ions from perpendicular to the surface far from the edge (which is the planar case described in section 2.1.1.) to along the wedge plane of symmetry at the edge. The shallower impact of the ions will affect the ion-surface interaction in the edge region - it can lead to reduced implantation but enhanced sputtering. It also has a rather surprising effect on the ion flux density at the surface of the wedge - while the ion flux entering the sheath in the edge region is increased, and so is in general the ion flux density hitting the surface, there will be a region close to the edge in which the surface will receive less bombardment due to the ions being almost parallel with the surface. The simulations done by Watterson (1989) form the bases of our simulations presented in Chapter 6, where we establish a simplified model in order to extend the two-dimensional case to three dimensions. The scaling of the problem allows its application to a range of ion energies. The results are therefore relevant for a wide range of techniques.

The increasing power of computers has recently enabled the simulation of the plasma sheath around objects of a more complicated geometry - for example U-shaped samples (Keller, 2001), L-shaped samples (Paulus, 1999), a wafer on a stage (Kwok, 1999) or bearings (Zeng, 1999).

We should emphasise that all the discussion of the electric field around wedge-shaped samples presented so far assume that the edges are 'infinitely sharp'. In practice however, the edges have always a certain radius of curvature. To a good approximation, the analysis for infinitely sharp edges can be used for edges with a radius much smaller than the dimensions of the plasma sheath. The changes in the electric field in the case of edges with a relatively big radius of curvature will be discussed in Chapter 6 (section 6.1.2.c).

In the case of ion-assisted PVD, the characteristics of the ion bombardment (ion flux, energy, angle) are tightly bound with the properties of the growing coatings. Non-uniformity of the bombardment which can happen in the case of non-flat samples therefore implies non-uniform coating properties. The situation is discussed in the next section.

2.2. The effect of ions on coating properties

The growth of a coating can be described as composed of three successive steps (Thorton, 1986):

1.) Transport of the coating species to the substrate.

2.) Adsorption of these species onto the surface of the growing coating, their diffusion over this surface and finally their incorporation into the coating or their removal from the surface by sputtering or evaporation.

3.) Movement of the coating atoms into their final positions within the coating by processes such as bulk diffusion.

Due to the non-equilibrium nature of PVD techniques, the growth of the coatings and thus the resulting coating properties will strongly depend on the deposition conditions. In the case of sputter deposition, the transport step (step 1) is controlled by chamber geometry and working gas pressure, while the steps 2 and 3 - diffusion, nucleation and resputtering processes - are dependant on the substrate temperature and can be significantly influenced by energetic particle bombardment.

2.2.1. Flat samples

a.) General models

Extensive research has been done to examine the relationship between the deposition conditions, including the ion bombardment, and the properties of PVD deposited coatings. The vast majority of studies examine the problem in the case of ideal flat samples.

The general characteristics of the relationship between deposition conditions and coating microstructure are described in the literature in the form of structure-zone models. Adatom mobility of the ions is the primary correlation process in all cases. The first such model was published by Movchan and Demchishin (1969) who found that the microstructure of several evaporated coatings could be represented as a function of homologous temperature (substrate temperature relative to the coating melting temperature T/T_m) by three zones, each with its own characteristic structure and physical properties. The model is shown in Fig.2-5a. The transition from one zone into another is related to the three important steps in the growth of the coating mentioned above. The low temperature zone 1 structure consists of columnar grains separated by voids. In this zone the atomic mobility is low, the incident atoms adhere where they impinge, and atomic shadowing - influenced by the transport of atoms towards the substrate (step 1) - is thus the dominant mechanism for growth. At higher temperatures the surface diffusion of the atoms (step 2) becomes significant which leads to dense columnar zone 2 structure. In zone 3, at still higher temperatures, the bulk diffusion (step 3) becomes activated which enables recrystallisation of the grains leading to fully dense equiaxed coating structure. The Demchishin-Movchan (DM) model was established for coating depositions without (significant) ion bombardment, the temperature being varied by heating the substrate. The influence of ion bombardment on the growing coating is however similar to increasing the substrate temperature, as the ions deliver energy to the adatoms and thus enhance the surface and bulk diffusions (Hultman, 1991). The ion bombardment, under suitable conditions, thus results in densification of the coatings and enhanced renucleation (which will be discussed in more detail later).

The DM zone model was extented by Thorton (1974) to magnetron sputtered films by adding an axis to account for the effect of working gas pressure (Fig.2-5b). Messier (1984) further extended the zone model by replacing the pressure axis with substrate bias axis, which directly shows the role of ion bombardment. Increasing bias voltage increases the energy of the bombarding ions, thus enhancing the adatom mobility (providing the energy is not too high). Consequently, increase in the bias voltage during the deposition can suppress the voided zone 1 structure and thus leads to densification of the coating. A structural zone model based on the mobility of

individual grain boundaries was proposed by Grovenor (1984) (Fig.2-5c). Increase in the temperature increases the mobility of the grain boundaries - which enables the growth of larger grains at the expense of smaller and leads to dense coating structure.

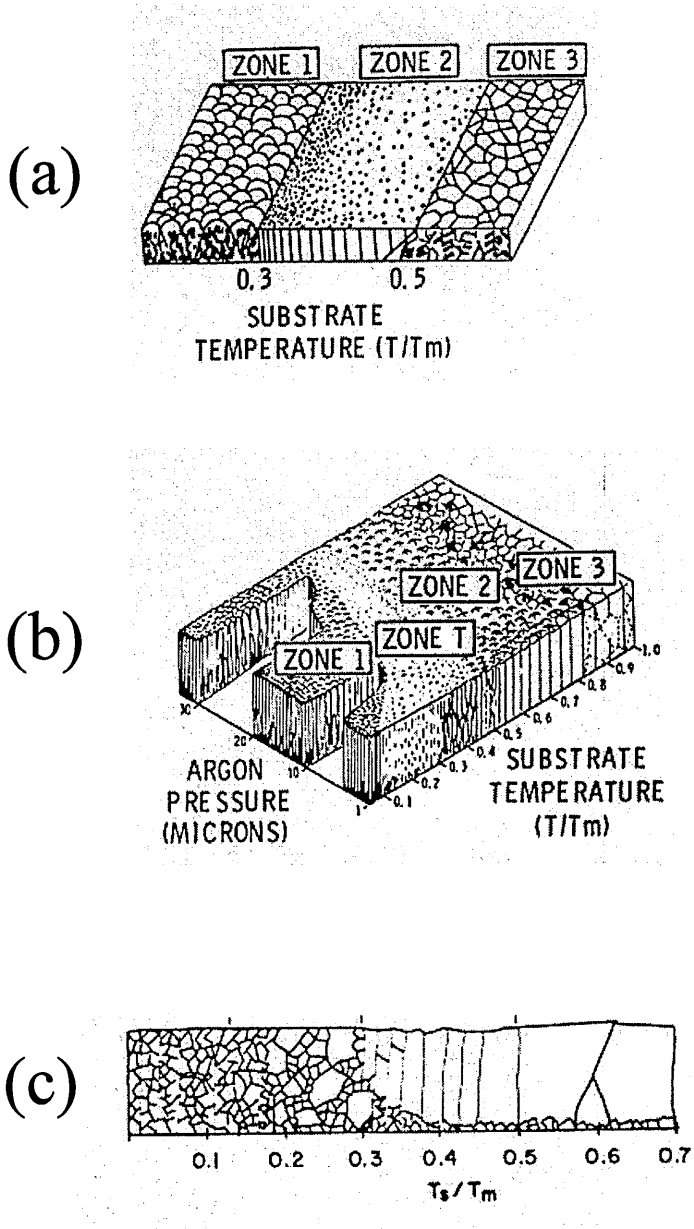

Fig.2-5: The structural zone models for coating growth proposed by: (a) Movchan and Demishin (1969), (b) Thorton (1974), and (c) Grovenor, Hentzell and Smith (1984).

The relationship between the density of the coatings and adatom mobilities which is the bases of the zone models is supported by theoretical simulations. Monte Carlo (Muller, 1985 and 1986) and molecular dynamics (Muller, 1987) simulations of

the film growth have shown that porous microstructures form because of shadowing on the atomic size scale due to low adatom mobility. Simulations also predict that films grown under low-energy ion irradiation should have a density increasing almost linearly with the ion-to-atom flux ratio.

The utility of structural zone models stems from their simplicity and generality (Messier, 1986). In the case of ion bombardment which induces a range of different effects (besides the enhanced adatom mobility) the relationship between the microstructure of the coatings and the deposition conditions is, however, more complex. Extensive research work in the last 20 years has shown that the interaction between the ions and the growing coatings can cause:

a.) resputtering of the adatoms, which competes with the growth (when the atoms receive enough energy from the ions to be detached from the surface)

b.) fundamental changes in the growth kinetics due to:

- enhanced surface diffusion (enhanced mobility of the adatoms combined with alterations in surface binding energies and the size of adatom clusters)
- production of defects in the growing surface
- incorporation of trapped ions into the coating
- alteration of the chemical reactions between the atoms.

The effects which dominate in a particular case depend on the ions characteristics - energy, flux, angle of incidence, mass - as well as the substrate and coating materials, their crystallographic orientation, coating growth rate and growth temperature. Ion irradiation during growth can thus have beneficial effects, such as enhanced diffusion of the adatoms leading to coating densification. On the other hand, it can also lead to residual damage of the coatings due to ion-induced defects and ion implantation, and its partial or complete removal by the resputtering of the adatoms. In practical applications, careful balance of the deposition conditions is therefore required.

b.) TiN and TiAlN coatings

The structure-properties relationship in nitride-based coatings is of particular importance since nitrides have high melting temperature and the films are usually deposited far from thermal equilibrium conditions. (The melting temperature for TiN

and TiAlN is >2000°C.) Furthermore even small deviations from a particular microstructure can have detrimental effects during usage in an actual application. The relationship is, however, complicated due to the complex nature of the deposition process and the large number of parameters imposing kinetic limitations on the growth process.

Extensive work has been done to examine the influence of ion bombardment on the properties of TiN and TiAlN coatings, often by varying the ion energy and/or the ion flux. The ion characteristics in some of the most detailed studies are summarised in Table I.

Work by:	**coating**	J_i/J_{me}	U_b	T_s	**ions**
Sundgren (1983)	TiN	0-4	0-700 V	500° C	Ar^+ (+ N_2^+)
Hultman (1988)	TiN	1.3	0-500V	550-850° C	N_2^+
Hultman (1991), Valvoda (1991)	TiN	0.3-7.1	100 V	350° C	Ar^+ (+ N_2^+)
Petrov (1992)	TiN	0-0.6	0-1800 V	360-500° C	Ar^+
Hultman (1995)	TiN	1-15	20 V	350° C	N_2^+
Hakansson (1987)	TiAlN	1	0-250V	250° C	Ar^+ (+ N_2^+)
Adibi (1993), Petrov (1993)	TiAlN	1-10	20-100 V	250° C	N_2^+

Table I: Summary of the deposition conditions from selected studies examining magnetron sputtering of TiN and TiAlN coatings.

Without the use of ion bombardment, at substrate temperatures less than 500°C, both TiN (Sundgren, 1983 and Petrov, 1992) and TiAlN (Hakansson, 1987) were found to have voided underdense structure. The formation of this type of microstructure as a result of low adatom mobility and atomic shadowing was demonstrated by Monte Carlo and molecular dynamic simulations, described above. Closer examination (Petrov, 1993) has shown furthermore that the growth without ion bombardment is competitive - which results in non-uniform columnar structure (the column width of some columns increases with the thickness of the film while others grow out of existence) and in

kinetics-controlled (111) preferred orientation of the grains. The open voided structures obtained in these conditions cannot support large vertical loads and hence have relatively low hardness (Hakansson, 1987).

To obtain dense TiN or TiAlN films without the use of ion bombardment, temperatures significantly higher than 500°C (Sudgren, 1983) would be required. The films grown at high temperatures have more uniform and denser columnar structure and exhibit thermodynamically driven (002) texture (Hultman, 1995). These temperatures are however too high for most of the applications. In the case of cutting tools made from high speed steel for which the tempering temperature is ~550°C, the high temperatures would induce unwanted changes in the structure of the steel. In order to keep the substrate temperature below 500°C and obtain dense high quality films, ion irradiation during growth has thus to be employed.

The use of ion bombardment during growth introduces two fundamental parameters which affect the film microstructure, and hence properties - the energy of the ions (E_i) and the flux of the ions relative to the flux of metal atoms incident at the substrate at the same time (J_i/J_{me}). The importance of considering the ratio J_i/J_{me} rather than purely J_i was shown by Hultman (1991). Under some conditions the coating properties can be correlated with the product of E_i and J_i/J_{me} - which is related to the average energy brought by the ions per atom (Harper, 1984 and Huang, 1985). The increase in both - ion energy and ion/metal flux ratio - can lead to densification of the coatings, as the adatoms receive in total more energy. In general, however, the ion-irradiation-induced changes in film microstructure and properties were found to follow distinctively different mechanistic pathways depending upon whether E_i or J_i/J_{me} was varied (Petrov, 1993).

Even a relatively modest increase in the ion energy above 20-40 eV (at low temperatures, in the case of N-ions or Ar-ions) leads to creation of ion-induced defects. Some of these defects can, however, be annealed out because of the simultaneous enhancement of the adatom mobility. The balance between the two processes depends upon the ion energy which determines how deep the ions can penetrate, and how many defects they can create (Hultman, 1988). For low substrate biases ($U_b < 100V$ in the case of TiAlN studied by Hakansson, 1987) where the collision cascade is localised in the outermost surface layers, the residual defect density is relatively low (provided the

ion flux is not too high). At higher bias voltages however the increased energy of the ions and the increased depth of collision cascades causes a larger fraction of the defects (point defects, dislocation loops), as well as ions, to remain trapped in the lattice. This causes continuous renucleation during the growth (disrupting the columnar structure of the coating) and changes the stress inside the coating from tensile to compressive, increasing with the ion energy - especially for the usual case of deposition in mixed Ar/N_2 discharges (Hultman 1988, 1991 and 1995). In the case of very high ion energies (in the keV range) the main effect of the ion bombardment becomes the implantation of the ions into the material. A review of ion-surface interaction in these conditions is presented for example in Sharkeev (1994).

Increase in the ion/metal flux ratio has a different effect on the growing coating. If the energy of the ions is kept sufficiently low, the collisions happen near the surface and their primary role is to enhance the adatom mobilities. The effect of increasing the ion flux in these conditions is thus similar to increasing the substrate temperature. TiAlN coatings deposited at low substrate temperatures (T_s = 250°C) under conditions of low ion energy E_i = 20 eV and low ion/atom ratio J_i/J_{me} = 1, were found to have (111) texture, evolving gradually by competitive growth, and develop a porous columnar structure. On the other hand, films deposited under the same conditions but at higher ion flux Ji/Ja > 5, exhibited complete (002) texture and a dense columnar microstructure - closely resembling TiAlN coatings obtained by increasing substrate temperatures from 250°C to >400°C, without ion bombardment and thus without ion-induced defects (Adibi, 1993). A similar trend was observed for TiN coatings in (Hultman, 1995).

Another (unwanted) effect related to the use of ion bombardment during the growth is the resputtering of the atoms from the growing layer by the ions, which can lead to reduction in the thickness of the coatings and in severe cases complete removal. This effect depends on the total energy delivered by the ions per atom, and is thus enhanced by both increase in the energy of the ions and/or increase in the ion flux. If relatively low ion energies are used, the resputtering can be reduced, provided however that the ion flux is not too high.

The growth of TiN and TiAlN high-quality films with reduced epitaxial temperatures thus requires a careful balance, utilising the beneficial effects of ion

irradiation, such as enhanced diffusion, while minimising residual damage and resputtering of the coating - which can be achieved by selecting low ion energy and relatively high ion/atom flux ratio. In these conditions, high quality dense films with good mechanical properties can be obtained. In practical applications, growth rates of a few μm/h, ion current densities in the mA/cm^2 range and ion energies between 25 and 100 eV (and temperatures below 500°C) are used (Adibi, 1993 and Hultman, 1995). The typical ion/metal ratio is thus ~1-10 The demand for a deposition method which would allow a significant increase in the ion flux incident at the substrate, as well as independent control of the substrate ion current density and the substrate bias, lead to the development of unbalanced magnetrons with magnetic plasma confinement (described in more detail in Chapter 3).

In the case of flat samples, the relationship between the ion characteristics and the coating properties is examined by comparing different samples, each deposited at different conditions. The relationship is in principle the same in the case of non-flat samples, but here different conditions can occur within one sample - leading to local changes in the coating properties. As discussed in section 2.1.2. for free-standing wedge-shaped samples, a sharp edge will induce changes in the ion flux and the angle of incidence of the ions. Due to the gradual change in the conditions of the ions bombardment we can expect changes in the ion-surface interaction and thus in the properties as a function of the distance from the edge. Despite the importance of the problem in practical applications where three-dimensional objects have to be coated, only few related reports, offering no detailed explanation or quantification of the effects, have been published. They are discussed in the next section.

2.2.2. Non-flat samples

a.) Changes due to non-uniformity of the plasma sheath

Magnetron sputtering and arc deposition

Johansson (1984) has examined the TiN thickness variations on non-flat substrates (sharp wedges, U- and L-shaped samples) coated by DC magnetron and RF

sputtering. In the case of wedges coated by magnetron depositions with ion/metal flux ratio ~0.6, changes in the thickness as a function of the distance from the edge were found which were strongly dependent on the ion energies. For $U_b < 150V$ the thickness was increasing, at $U_b = 200V$ it was decreasing, and at $U_b > 350V$ complete resputtering of the coating near the edge was observed. The effects were attributed to higher ion flux near the biased edge leading to enhanced resputtering in the edge region, increasing with the ion energy.

Rother (1997) and Jehn (1997) reported on magnetron (double and unbalanced) and arc deposited TiN coatings on sharp wedges and grooves. They have observed thickness and hardness variations, as a function of the substrate geometry. In the case of magnetron deposition, changes in the colour of the coating could be seen as well. The experiments were done at conditions of $J_i/J_{me} \sim 1$, $E_i \sim 50\text{-}100$ eV.

Kvasnicka (1999) and Novak (1999) have studied homogeneity and adhesion of TiN coatings deposited on blades (with angles 20° and 90°) by magnetron and arc sputtering at Ei = 0-60 eV (J_i/J_{me} not being specified). Degradation of the coatings in the edge area was observed - lowered adhesion, in some cases desintegration. The effects were observed to depend on the substrate bias (0-60 V) and the edge radius of curvature (5-80 μm).

Changes in properties of CrN coatings deposited on sharp wedges (with angles 30°, 60°, 90°) by cathodic arc were examined by Kim (1998). Substrate bias was varied between 100 and 400 V (J_i/J_{me} not being specified). He observed an accumulation of macroparticles near the edges - indicative of higher ion flux. The density of the accumulated particles increased with the sharpness of the edge. Changes in the thickness, composition and hardness of the coatings in the edge region were detected as well.

Plasma immersion ion implantation and plasma nitriding

In the keV energy range, ion bombardment results in implantation of the ions into the material being bombarded. The resulting modification of the material properties in a distinctive surface layer is used in techniques such as plasma nitriding and PIII. Here also, the treatment of non-flat samples is related to the problem of non-uniform

ion bombardment leading to non-uniform implantation, and thus non-uniform material properties.

In the field of plasma nitriding, where N ion irradiation with energy ~500 eV is used to create a modified N-enriched surface layer (in order to increase the adhesion of subsequently deposited coatings and improve corrosion resistance), non uniform nitrided layers were observed on non-flat samples. Ataide (2003) has observed a modified region near the edges of nitrided cylindrical samples, discussed in relation with non-uniform ion flux due to electric field variations and with surface diffusion. In this region N-concentration in the surface layer and its microhardness were altered. Nayal (1999) examined the uniformity of nitriding in the case of industrially used drills. Changes in the N-concentration and hardness in the cutting edge area were observed.

Ensinger (1997 and 1998) has measured the ion implantation concentration during the PIII process (described in section 2.1.2.) as a function of the distance from the edge, for wedges with different edge angles. For all the wedges he found a decrease in the implantation concentration towards the edge in agreement with the effects simulated by Watterson (1989) and others - reduced implantation depth (shallower implantation) and increased resputtering of the near-surface layer due the oblique angles of incidence of the ions, as well as decreased ion flux density on the surface near the edge (discussed in section 2.1.2.). The observed gradient was found to increase with the sharpness of the wedge.

b.) Changes due to other effects

The electric field in the vicinity of non-flat surfaces is different than in the case of flat surfaces (equation 2-8). The geometry of the sample (whether for example the edge is free-standing or there are several adjacent edges) and the plasma sheath width (whether it is comparable with the surface variations or much bigger) determine how much the plasma 'feels' the alteration in the electric field, and thus how much it will change. Our research which will be presented in the following chapters, and thus the discussion presented so far, is concentrating on the case of free-standing convex samples. The effects we study - non-uniformity of the ion bombardment and thus of the coating properties - are a consequence of non-flat plasma sheath which follows the

shape of the non-flat surface. There are however also papers reporting changes observed on non-flat samples due purely to the relative orientation between the ion flux and the sample surface. Examples of this type of studies are discussed in this section.

In the case of convex surfaces such as wedges, the sheath of any width bends around the surface if it is free-standing. When, however, several wedges are placed next to each other, it is possible to smear out the plasma sheath, if the plasma sheath width is not very small. In these cases, local changes in the properties of the coatings are created because of the changing angle of incidence of the ions - the ions come all from one direction but meet the oblique surface at different angles (see Fig.2-6a). An example of this type of situation is the work of Jonsson (1999) who studied sloped surfaces (composed of adjacent wedges) coated by magnetron sputtering. The dimensions of the surface variations being much less than the plasma sheath width (μm vs. mm-scale), the ions flux could be regarded as unidirectional, hitting the sloped surface at different angles depending on the position. The resulting gradual change in the composition of magnetron sputtered coatings was studied, both experimentally and theoretically.

In the case of concave surfaces, such as trenches and grooves, the degree to which the plasma sheath will be affected in their vicinity depends on the relative dimensions of the features and the plasma sheath width. If the substrate variations are much less than the plasma sheath dimensions, which is often the case for coating applications on microelectronics devices, the plasma sheath above the surface is practically planar. Here again the ion flux can be described as unidirectional and changes in the coating properties will be created as a result of different orientations of the surface relative to the ion incidence (see Fig.2-6b). Detailed numerical and experimental studies of the coating uniformity in the case of trenches with different geometries (aspect-ratios) coated by magnetron sputtering was done for example by Hamaguchi (1996).

There are also coating techniques which, instead of immersing the samples into plasma, use a focused beam of ions directed towards the sample in order to influence the coating condensation. Here the ions are directed to arrive unidirectionally and again changes in the coating properties are created when they hit non-flat surface due to the different angles of incidence. An example are the works of Enders (1994) and Klatt

(1995) which study the thickness variations on cylindrical samples coated by 'ion-beam-assisted deposition' (IBAD).

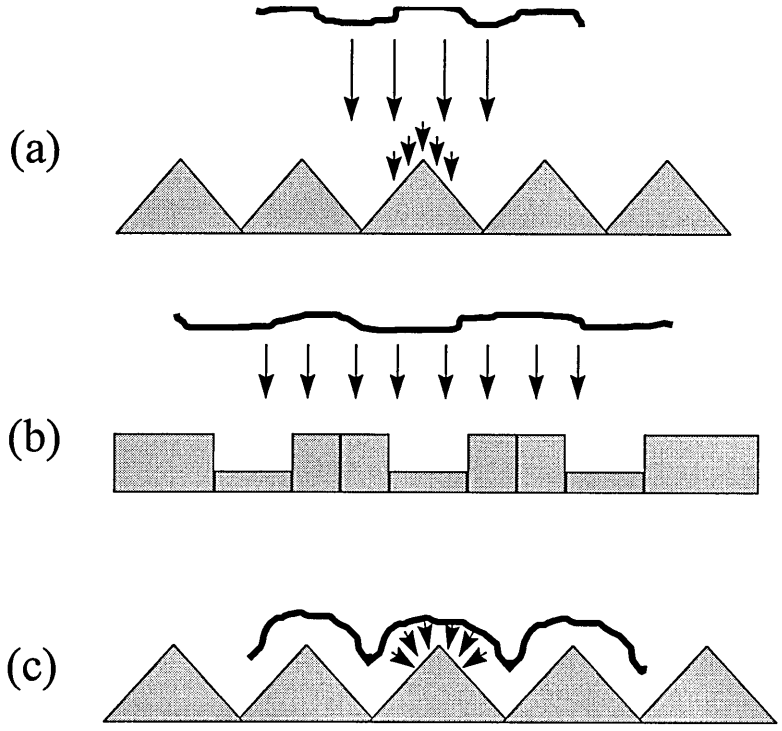

Fig.2-6: Schematic representation of the plasma sheath and the ion bombardment in the case of adjacent wedges and groves. If the dimensions of the surface variation are much smaller than the plasma sheath width - figure (a) and (b) - the plasma sheath and thus also the ion flux and incidence are similar to the case of a flat surface. If however the dimensions of the surface variation are similar to sheath width, the plasma and the ions are altered by the non-uniform electric field in the vicinity of the surface - figure (c).

Chapter 3: Fabrication and analysis of the samples

In this chapter we summarise the experimental detail related to the fabrication of the samples: preparation of the wedge-shaped samples and subsequent coating deposition by combined cathodic arc/unbalanced magnetron process. We then discuss the analytical methods we have used to study the coatings on the wedge-shaped samples, and present detailed analysis of the problems encountered during compositional measurements using SEM+EDX and their possible solution.

3.1. Fabrication of the samples

3.1.1. The geometry of the samples

Wedge-shaped samples were chosen as a simple model which would represent the real cutting edge and would allow to change easily the edge angle and radius of curvature. This geometry was also well suitable for theoretical modelling of the plasma sheath. The wedges were machined from stainless steel and carefully mirror-polished (to roughness ~10 nm). A schematic view of the wedges is presented in Fig.3-1.

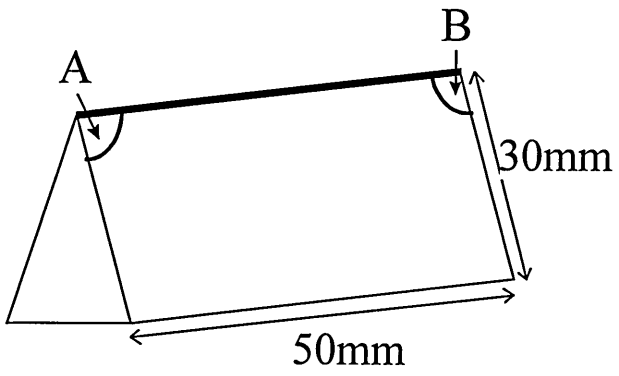

Fig.3-1: Schematic representation of the wedge-shaped samples. Marked by the letters A and B are the two corners of the wedge.

We have varied the wedge geometry (angle and radius of curvature - see Fig.3-2), as well as the deposition conditions (substrate bias). Two different coatings were applied on the wedges. The different samples are summarised in Table II.

	Coated with TiAlN/VN:	Coated with TiAlCrYN:
Angle	30°, 45°, 90°	30°, 45°, 60°
Radius of curvature	10 μm	2 μm, 250 μm
Deposition bias	-75, -105V, -150 V	-75V

Table II: Summary of the different wedge-shaped samples examined in this study.

For the wedges coated with TiAlN/VN, three different wedge angles, spanning the angular range typical for cutting tools, were chosen: 30°, 45° and 90°. The radius of curvature of all the wedges was ~10 μm. The wedges were coated at three different substrate bias values: -75V, -105V and -150V.

In the case of TiAlCrYN coating, wedges with angles 30°, 45° and 60° were coated. The deposition bias was -75V. Two sets of wedges were fabricated. The first set was polished very carefully to leave the edges as sharp as possible, the second set was ground and polished extensively to produce rounded edges. In this way, for each angle two very different radii of curvature - 2 μm and 250 μm - could be examined.

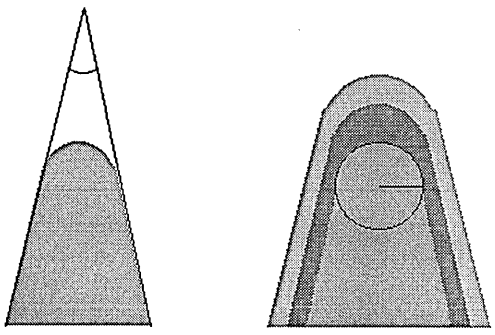

Fig.3-2: The two parameters describing the edge geometry - the angle and the radius of curvature of the edge. While the angle is fixed, the radius of curvature changes during the coating deposition (increases with increasing the thickness of the coating).

In order to be able to compare the model wedge-shaped samples with real cutting tools, industrially used ball-nosed end mills (Marwin tools, HSC16 2B, 8 mm diameter) were coated at the same time as the wedges and analysed.

3.1.2. The coatings

The edge-related effects were studied on two different state of the art coatings used in cutting tool industry: $Ti_{0.5}Al_{0.5}N$/VN and $Ti_{0.47}Al_{0.48}Cr_{0.03}Y_{0.02}N$. These type of sophisticated coatings help in the development of cutting tools suitable for dry machining - a promising technology which avoids the use of cooling and lubricating fluids connected with ecological and economical problems (environmental pollution and problems concerning waste disposal.)

TiAlCrYN has the same attractive properties as TiAlN - high mechanical hardness, good wear and oxidation resistance - benefiting from further improved oxidation and corrosion resistance by the small additions of Cr and Y (Donohue, 1999). It is used for example to coat cutting tools for dry high speed cutting of die steels or for the protection of aerospace Ti alloys.

TiAlN/VN on the other hand has the advantage over TiAlN of being a superlattice - a material composed of nanolayers of two different materials. This type of 'ordered mixing' allows one to take advantage of the characteristic features of each material and also to obtain synergetic effects. The use of multilayers was shown to improve the adhesion between the coating and the substrate and increase the strength and hardness of the deposited films (Helmersson, 1987). The TiAlN/VN coating is used as a low friction wear resistant general purpose coating for cutting tools used in the machining of high speed and high alloy steels. The period of the superlattice was typically 3.0 nm (Münz, 2000).

Both coatings had a thin base layer which improved the adhesion of the coating to the substrate - 0.2 μm thick TiAlCrN in the case of TiAlCrYN and 0.2 μm thick TiAlN in the case of TiAlN/VN. Additionally, the top of the TiAlCrYN coating was protected by a specially designed thin oxide layer. More details can be found in (Münz, 2000).

3.1.3. The deposition process

The coatings were deposited by industrially used combined cathodic arc/unbalanced magnetron sputtering process (CA/UBM). The combination of arc deposition with magnetron sputtering, introduced by Münz (1992), offers several advantages over other deposition techniques. Magnetron sputtering eliminates the problem of droplet formation associated with arc discharges, while cathodic arc deposition provides significantly higher ion fluxes. The use of arc ion-etching of the substrates prior to coating deposition produces high quality coating/substrate interface (Schönjahn, 2000). The subsequent unbalanced mode during the main coating deposition provides low energy high flux ion irradiation, which was shown, in the case of flat samples, to greatly improve the properties of the coatings (as discussed in section 2.2.1.).

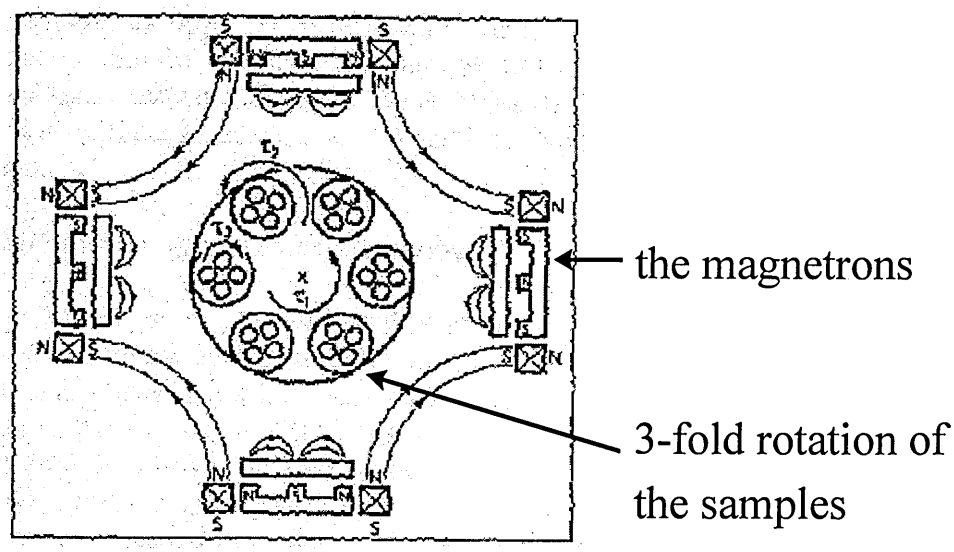

Fig.3-3: Schema of the CA/UBM industrial deposition chamber.

The depositions were performed in an industrial size Hauzer Techno Coating HTC 1000-4 ABS combined CA/UBM sputtering system, shown schematically in Fig.3-3. The growth chamber consists of four (19x60 cm) vertically mounted targets which can function in either UBM or CA mode - depending on the positioning of the permanent magnets. The cathodes are magnetically coupled in close-field manner by electromagnets surrounding the targets. This allows sputtering to be carried out in a

magnetically 'unbalanced' mode in order to provide higher ion currents to the substrate. During deposition, the substrates undergo 3-axis planetary motion, at an average distance from the targets of 25 cm. A typical deposition sequence consists of substrate heating and degassing, target sputter-cleaning, CA substrate etching, and UBM coating deposition.

Sputtering conditions typical for industrial depositions on cutting tools were used: target power 8 kW, substrate temperature 450°C, sputtering gas (Ar) pressure ~2×10^{-3} mbar and deposition time ~4 hours. The growth rate, measured on a flat substrate, was ~1 μm/hour. The characteristics of the ion bombardment were measured by plasma probes. The average ion to atom flux ratio was ~4. The plasma density, in the vicinity of a flat substrate, was in the range of 10^{16} m^{-3} and the average plasma temperature was ~3eV. The energy of the ions (given by the substrate bias) was varied from ~75 eV to 150 eV. Prior to the magnetron sputtering, a short cathodic arc etching step was used to clean the sample surfaces and to create a high quality interface for subsequent film growth - the samples were etched for 20 min at -1200V by V-ions (for TiAlN/VN) or by Cr-ions (for TiAlCrYN). Detailed description of the deposition processes can be found in (Petrov, 1997).

The deposition took place in a reactive Ar+N_2 atmosphere at total pressure of ~3×10^{-3} mbar:: Ar pressure ~2×10^{-3} mbar + N_2 pressure ~1×10^{-3} mbar. The N_2 fraction in the gas was thus ~0.3. Under these conditions, the dominant ion species present in the chamber were Ar^+. Detailed analysis of the fluxes of ion and neutral species during magnetron sputtering can be found in Petrov (1994).

3.2. Scanning and transmission electron microscopy

3.2.1. Principle of the techniques

The interaction between a high energy electron beam (in the keV-energy range) and a solid material generates a range of possible signals which can be detected and used for structural and compositional analysis (Fig.3-4). Some of the incident electrons cause emission of secondary electrons and characteristic X-rays from the material. These type of signals are detected by scanning electron microscopes combined with X-

ray spectrometers - the intensity of the secondary electrons is used to create an image of the sample, while the energy of the X-rays allows identification of the elements present. The transmission electron microscopes examine the electrons passing through the samples - directly transmitted and elastically or inelastically scattered. Necessarily the samples need to be very thin - typically < 200 nm (unlike in SEM where bulk samples can be analysed) and the energy of the beam is 10-100 times higher than that used by SEM instruments.

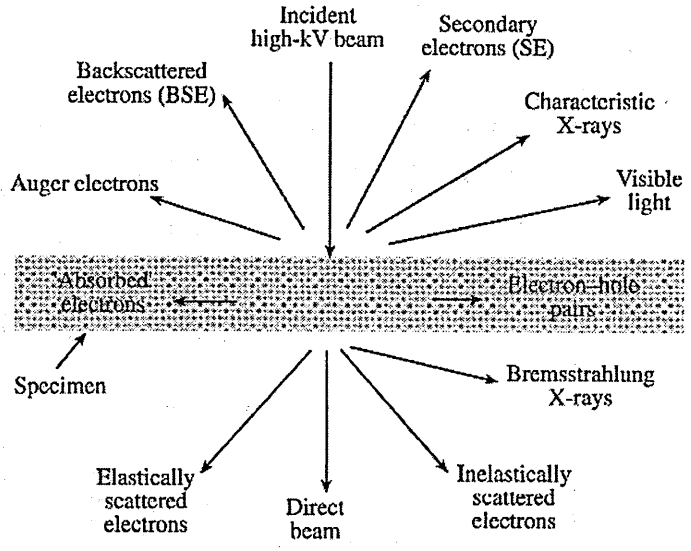

Fig.3-4: The range of different signals produced by the interaction between high-energy electrons and a solid material. (Taken from Williams, 1996.)

The major components of a transmission electron microscope are shown in Fig.3-5: there is a source of electrons, a system of condenser lenses to collimate the electron beam on to the specimen, an objective lens to provide a first focused and magnified image, and a projector system (composed of several lenses) which magnifies the image to its final size and projects it to a viewing screen. The structure of the instrument is analogous to a transmission optical microscope, using electromagnetic lenses instead of the optical ones.

In the back focal plane of the objective lens all electrons diffracted by the specimen in a specific direction will be collected to a point (Fig.3-5). This point will represent a family of lattice planes in the crystal lattice and is hence a reciprocal lattice

point. The diffraction pattern (the collection of the reciprocal lattice points) can be imaged on the fluorescent screen on the bottom of the TEM by changing the focus of the uppermost projection lens from the image plane of the objective lens to its back focal plane. The selected area aperture is used to select the area from which the diffraction information is obtained.

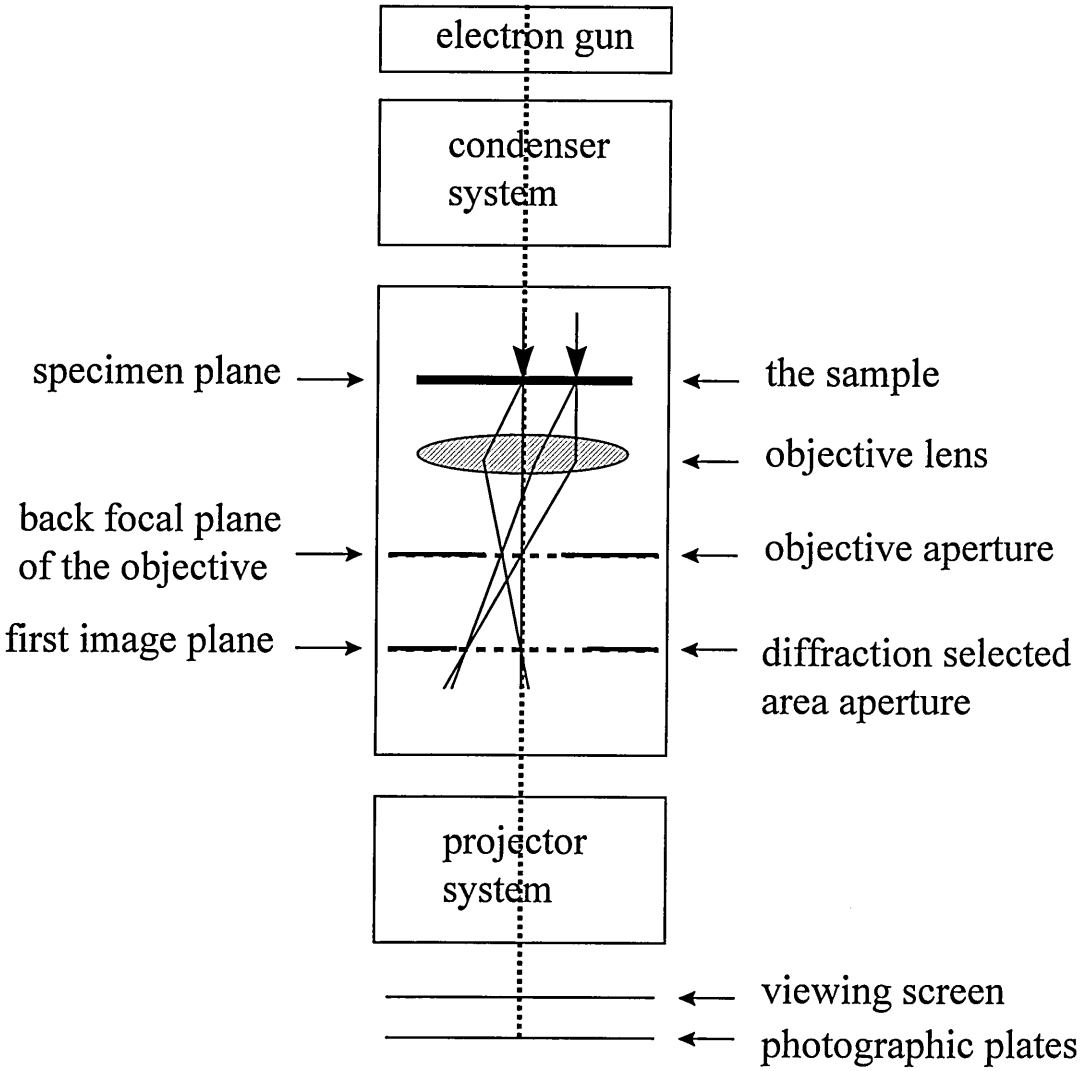

Fig.3-5: Schematic representation of the main parts of a transmission electron microscope, arranged along the main axis of the instrument.

The contrast in the imaging mode arises both from inelastically as well as elastically scattered electrons. The contrast between the inelastically scattered electrons is related to the sample thickness, the density or atomic number within the sample. The

far more important contrast mechanism is created by the diffraction of the elastically scattered electrons. The objective aperture (placed in the back focal plane of the objective lens) can be used to block all the diffracted electrons, which creates a bright-field image, or select electrons diffracted in a certain direction - the resulting image is called dark-field image. The size of the condenser aperture controls the intensity of the electron 'illumination'.

The SEM instrument is essentially the top part of the TEM, with the addition of scanning coils (placed above the objective lens) which scan the electron beam across the sample. The secondary electrons are collected by a detector positioned at an off-normal angle. The reflected primary electrons can be collected by another detector placed at near-normal incidence. The detected electron current is magnified and swept over a TV-screen simultaneously with the scanning electron probe. The contrast in the image is dependent on the secondary electron yield difference over the sample surface.

The maximum resolution in a SEM, typically ≥ 5 nm, depends on the diameter of the electron probe combined with the dimensions of the excitation volume of the signal being detected. In the case of a TEM, it is also influenced by the electron wavelength and the lens characteristics and can be < 0.5 nm.

3.2.2. Analysis of the coatings

The main tool of the analysis in our study was scanning electron microscopy - its big advantage being the possibility to assess big areas on the wedged-shaped samples and immediately see the differences as a function of the distance from the edge. Without difficult sample preparation, extensive information about the morphology, thickness and topography of the samples at different places could be collected. The combination of SEM with EDX allowed us to measure the composition at the same time. Here the linescan mode (detection of characteristic X-rays along a given line drawn on the sample) has shown to be especially useful - continuous change in the composition as a function of the distance from the edge could be detected. However, in order to get reliable results we had to analyse problems related to the EDX method - such as preferential absorption of some of the X-rays in case of multi-component material. The analysis is presented in section 3.3.

Transmission electron microscopy, on the other hand, was used to get detailed localised information about the internal structure of the coatings. It allowed us to study the grain structure of the coating right on top of the sharp edge (using the bright-field and dark-field imaging) and the preferred orientation of the grains (using the electron diffraction). Its main drawback was the difficult sample preparation, which is discussed in the section 3.2.3.

The wedges were analysed in three different situations shown in Fig.3-6. The whole wedges were studied by SEM+EDX from the top and from the side (Fig.3-6a). Furthermore cross-sectional samples from the edge region were prepared (Fig.3-6b) and studied by SEM and, after further preparation, by TEM.

The SEM analysis was performed using Jeol JXA-840A instrument at the accelerating voltage 20kV. The TEM analysis was performed using Philips CM20 STEM at 200 kV and Jeol JEM4000 TEM at 400 kV.

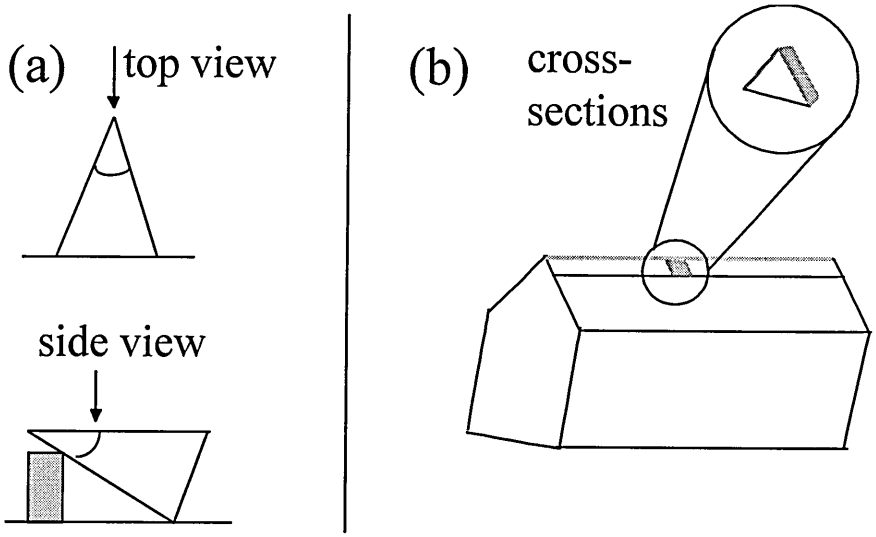

Fig.3-6: (a) The two different sample positions during the SEM analysis. (b) Schematic view of the cross-sectional samples, which were cut out from the edge region in the middle of the wedges.

3.2.3. Sample preparation

a.) SEM

The first step in the preparation of the cross-sectional samples is shown in Fig.3-6b. Small pieces - with dimensions ~2 by 2 mm and thickness ~1 mm - were cut from the edge area using Buehler ISOMET 4000 Linear Precision Saw. The cutting machine could be used to cut the stainless steel wedges, but not the much harder cemented-carbide end-mills. In this case spark erosion had to be used to separate the pieces from the edge area. The cross-section sides of all the samples were then mechanically mirror-polished.

b.) TEM

Two different TEM sample preparation techniques were used: ion beam milling using Gatan PIPS 691 and focused ion beam lithography using FEI FIB 200 instrument.

For the ion beam milling, cross-sections were first prepared in the same way as for the SEM analysis. They were then ground to a thickness of ~20 μm, polished and mounted on a supportive copper grid. The final thinning to electron transparency was done using high-energy Ar-ion bombardment inside the PIPS instrument. The energy of the ion beam was 5 keV and the average current was ~16 mA. The ion guns were positioned at 5° relative to the sample surface, in order to assure uniform thinning of the material (Helmersson, 1986). In our case, it was however very difficult to position the beams exactly at the sharp edge, and to thin the area uniformly. The process had to be interrupted at regular intervals and the sample removed and examined in the SEM - in order to check the thinning progress. Using the information from SEM, fine adjustments of the sample position relative to the beams had to be done by hand - which again was a major difficulty.

The FIB, on the other hand, was well suited for the preparation of our samples. The principle of FIB is very similar to a scanning electron microscope, except that a focused beam of ions, used instead of the electrons, can 'cut' the sample material along selected lines. The high precision of the focused beam allowed us to easily select the

region of interest. The process could be checked continuously (in-situ) with the attached imaging mode. The whole selected area could be thinned uniformly, up to a thickness ~80 nm. Here the critical part was the last stage of the preparation, when the extremely small sample, with dimensions ~10 by 10 μm and 80 nm thin, had to be collected from the chamber and plucked onto a supportive copper grid.

The FIB sample preparation of a cross-sectional sample from a 30° wedge is shown in Fig.3-7, taken inside the FIB chamber during the thinning process. We can see the rectangular groove situated on the edge from which, layer after layer, the material was cut away by the focused ion beam leaving a very thin cross-section in the middle of the groove. The major part of the thinning was done using ion beam with energy 30 keV and ion current 1 nA. In the last stage (when the sample thickness was ≤200 nm) the energy was decreased to 5 keV and the current to 100 pA - in order to reduce damage to the material by the focused ion beam. When the cross-section reached the final thickness (~80 nm), lines perpendicular to the cross-section were cut at the borders and the thinned area was detached from the rest of the sample. The dimension of the cross-section thus obtained were ~10 by 10 μm.

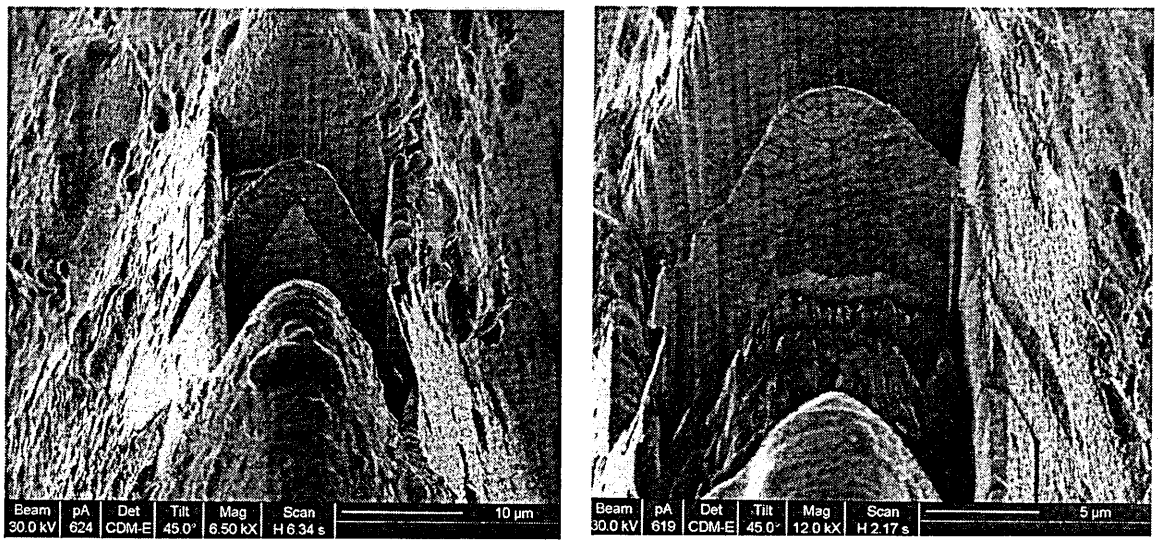

Fig.3-7: Micrographs (at two different magnifications) showing the FIB sample preparation. The coating around the edge is clearly visible in the thinned region.

3.3. EDX analysis - absorption problems

3.3.1. Inside the coating

During the compositional analysis of our TiAlN-type coatings we have been concentrating on the relative ratio of the two main elements - Al and Ti. In this section we would like to analyse the relation between the X-ray intensity of Al and Ti and their concentration inside the coating. We then discuss whether we can use the change in the Al/Ti X-ray ratio as an approximate direct measure of the change in the compositional ratio of this two elements.

The characteristic X-ray intensity is, to a first approximation, proportional to the mass concentration of a particular element (Reed, 1993). This is related to the fact that the incident electrons lose their kinetic energy mainly through interactions with orbital electrons of the target atoms, the number of which is approximately proportional to atomic mass. In reality however there are several effects which can disturb this simple assumption and need thus to be accounted for:

- absorption of characteristic X-rays emerging from the specimen
- loss of X-rays owing to incident electrons being backscattered out of the specimen
- variation in the efficiency of X-ray production, as governed by the 'stopping power' of the specimen
- enhancement of the characteristic X-ray intensity due to fluorescence by other lines and by the continuum.

These effects may be represented by separate factors: F_a (absorption), F_b (backscattering), F_s (stopping power) and F_f (fluorescence) and the overall correction factor F is given by the product of all the factors:

$$F = F_a F_b F_s F_f \,. \qquad \text{(Eq.3-1)}$$

The calculation of the correction factors is called 'ZAF analysis' - A stands for absorption, F for fluorescence and Z for atomic number (as both, the scattering and the stopping power, are function of the atomic number).

We have done the calculation for Al and Ti radiation inside pure TiAl alloy with Al/Ti atomic ratio 1:1, which means mass ratio ~0.58. The full calculation is presented and explained in the appendix. The absorption correction for the Al-Kα radiation in the

alloy was found to be 50% higher than that for the Ti-Kα radiation. All the other corrections were relatively small - backscattering ~1%, stopping power ~3% and fluorescence ~1%. Similar absorption correction was found for TiAlN. The ratio of the correction factor $F_{Ti/Al}$ inside $Ti_{0.5}Al_{0.5}$ was calculated to be ~0.75. If the atomic ratio of Al and Ti is 1, their mass ratio is: 13.1/22.6 = 0.58 - which is equal, in the first approximation, to the ratio of the emitted X-rays. Multiplying this by the correction factor, which accounts for the higher absorption of Al radiation, we get the corrected value of the Al/Ti X-rays ratio: 0.58×0.75=0.44. This is in good agreement with the experimentally measured values. For flat $Ti_{0.47}Al_{0.48}Cr_{0.03}Y_{0.02}N$ coating, the Al/Ti X-ray ratio (undisturbed by the presence of the substrate - section 3.3.2.) was measured to be ~0.46 (see Fig.3-11) , which is ~5% different from the value calculated using the simplified system. In the case of the $Ti_{0.5}Al_{0.5}N$/VN coating, the Al/Ti X-ray ratio measured far from the edge is ~0.50 (see for example Fig.4-6 in Chapter 4), which is ~12% different.

In our study we have been measuring the relative Al/Ti ratio at different positions along the samples. The relationship relating the change in the Al/Ti X-ray intensities ($I_{Al/Ti}$) to the actual change in Al/Ti composition ($c_{Al/Ti}$) can be written as:

$$\frac{(c_{Al/Ti})_1}{(c_{Al/Ti})_2} = \frac{(I_{Al/Ti})_1 \times (F_{Al/Ti})_1}{(I_{Al/Ti})_2 \times (F_{Al/Ti})_2}, \qquad \text{(Eq.3-2)}$$

where $F_{Al/Ti}$ is the ratio of the correction for Al to that for Ti and index 1 and index 2 denote two different positions. All the individual corrections which are included within the factor F are a function of the composition of the sample (see the calculation in the appendix). If the composition at the two places is different, the correction factor will thus also change. We need therefore to establish how big the difference will be for the range of compositions present in our samples.

Instead of several further ZAF calculations, we have done modelling of the EDX measurements using CASINO Monte Carlo simulation programme (Hovington 1997a, 1997b and Drouin, 1997). Fig.3-8 shows the typical schema of the simulations - electron beam (shown as red arrow) is bombarding the material and the trajectories of the primary and secondary electrons are calculated as well as any X-ray emissions during the interactions. We have simulated the EDX measurement on a TiAlN coating for a range of Al/Ti compositions. The corresponding intensity ratios in the

compositional range relevant for our coatings are shown in Fig.3-9. We can see that the relationship is to a good approximation linear, which means that in our conditions:

$$\Delta c_{Al/Ti} \approx \Delta I_{Al/Ti} . \qquad \text{(Eq.3-3)}$$

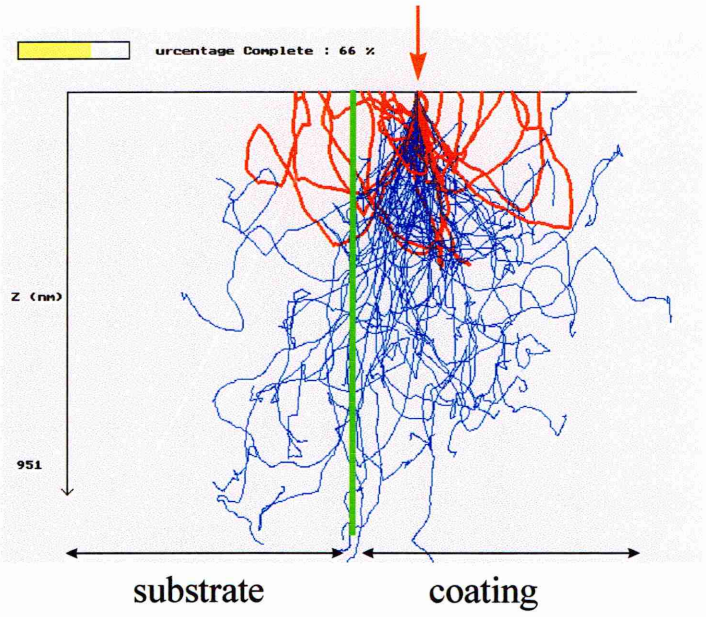

Fig.3-8: The figure shows a typical CASINO simulation. The electron beam (represented by the arrow) is scanned across the surface (the substrate-coating interface) and the electron trajectories for a series of positions are calculated. The pear-shaped excitation volume from which X-rays are emitted is clearly visible.

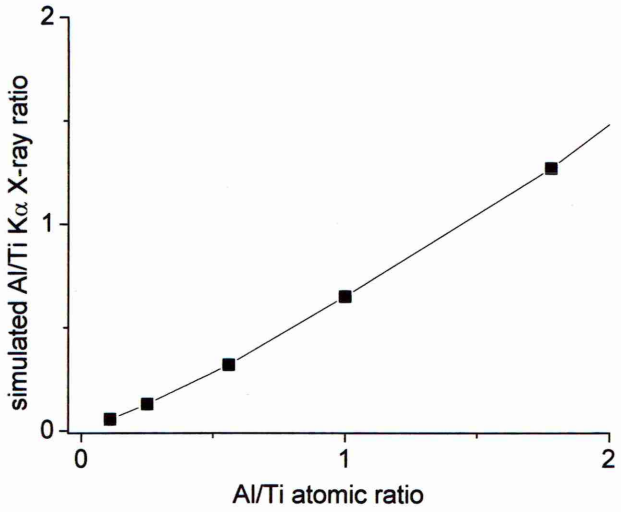

Fig.3-9: The ratio of simulated Kα Al/Ti X-ray radiation emitted from $Ti_{0.5}Al_{0.5}N$, as a function of the compositional ratio of the two elements (CASINO).

3.3.2. At the substrate-coating interface

We have seen in the previous section that Al radiation is much more absorbed by the coating material than that of Ti. The difference is however even greater when considering the substrate material. The corresponding ZAF calculation (the appendix) shows that the absorption factor for Al Kα radiation in Fe, which is the main component of our stainless steel substrates, is 2.2 times greater when compared to Ti radiation - a much bigger difference than in the case of the coating material. This effect, combined with the big excitation volume typical for SEM - 1 by 1 μm (Reed, 1993), can lead to problems related to the position of our samples with regard to the detector. Figure 3-10 presents Al/Ti linescans measured on a cross-section from a coated flat sample, where we know that the composition across the coating should be constant. When the sample is positioned so that the substrate is facing the detector (left side of the figure), the X-rays emitted from close to the substrate-coating interface are travelling through the substrate before reaching the detector. This is due to the enhanced absorption of Al X-rays inside the substrate material and leads to lowering of the Al/Ti detected intensity ratio. The problem starts to manifest itself at ~1.5 μm from the interface and the preferential absorption is continuously increasing as the interface approaches. (The slight slope of the Al/Ti intensities measured at distances >2 μm from the interface, where the ratio should be constant, was caused most probably by experimental problems during the analysis.) When the coating is facing the detector (right side of the figure) we get the non-disturbed uniform linescan. The different lines in the figure correspond to different tilting of the sample relative to the detector. As the sample in position A is tilted away from the detector (positive values), the path of the X-rays through the substrate is longer and thus the effect gets more significant - the Al/Ti X-ray ratio is decreased more and the region where it disturbs the measurements is increased.

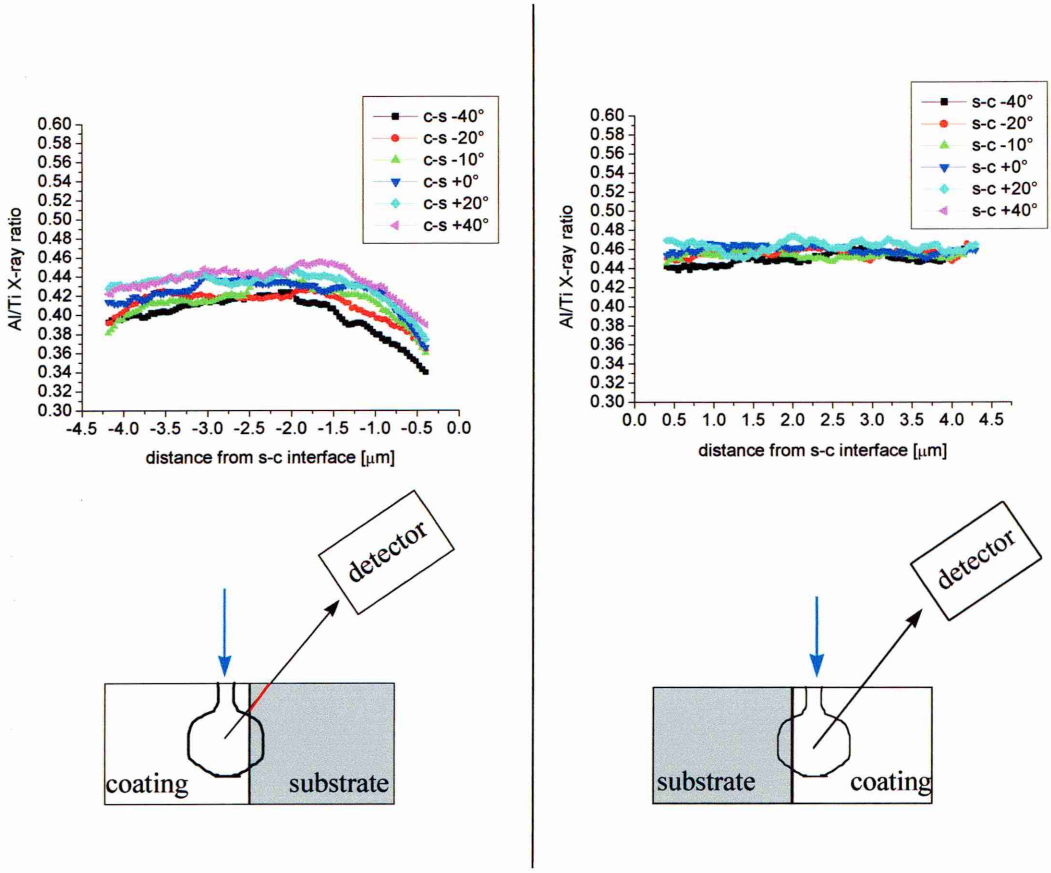

Fig.3-10: Al/Ti X-ray ratio emitted from the coating as a function of the distance from the substrate-coating interface - measured for different positions of the coating relative to the substrate and the X-ray detector. Additionally, the sample was tilted in the plane of the paper, in clockwise (positive angles) and contra-clockwise (negative angles) direction.

For comparison we have simulated similar situations using the CASINO program - Fig.3-11. Here instead of changing the tilting of the sample, we could change the tilting of the detector (with the sample always staying horizontal). The angle 40° corresponds to the standard situation inside the SEM chamber - and we can again see the difference between the two possibilities due to the absorption effect. The smaller the angle is, the longer are the X-rays travelling through the substrate and thus the effect is enhanced. When the detector is perpendicular to the plane of the sample (angle 90°), the effect disappears as all the X-rays emitted upwards are going directly to the detector. The change in the sample-detector geometry corresponding to the tilting of the sample and the tilting of the detector is shown schematically in Fig.3-12.

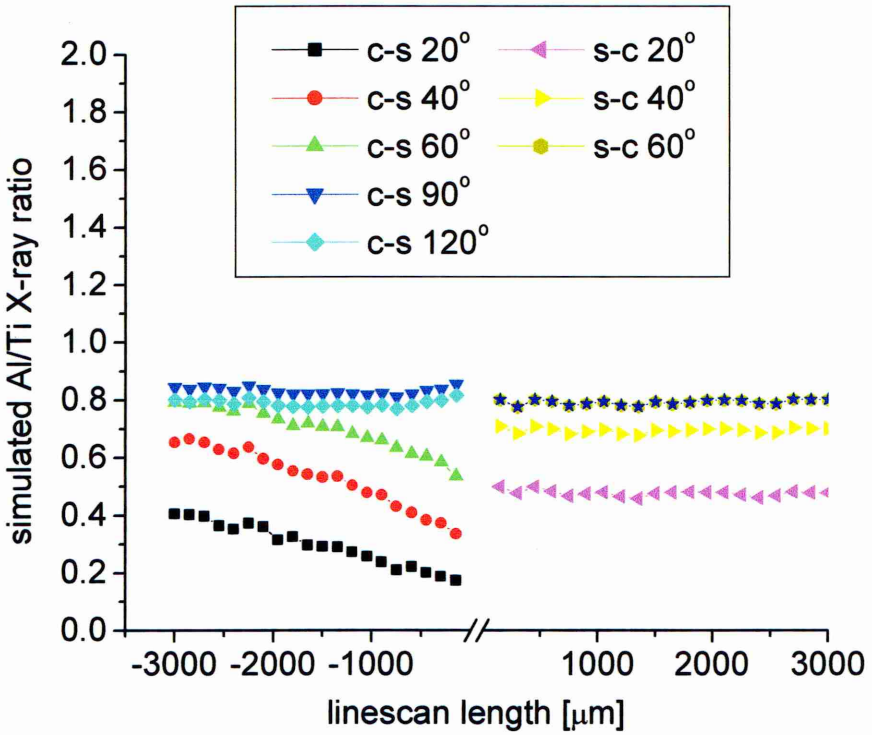

Fig.3-11: Simulated Al/Ti linescans for different positions of the coating relative to the substrate and the X-ray detector (CASINO). The positioning of the sample is similar to that shown in Fig.4-6, but in this case the position of the detector was rotated. The angle 90° corresponds to X-ray detector being positioned perpendicularly to the sample surface.

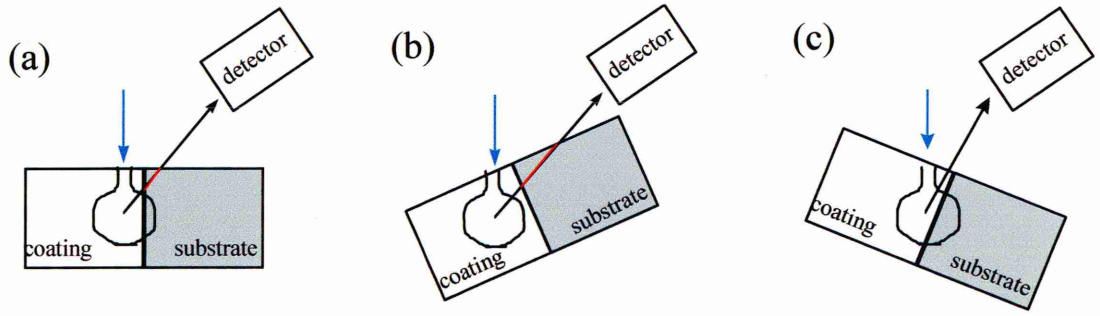

Fig.3-12: Schematic drawings showing the path of the X-rays from the excitation volume to the detector, the sample being: (a) in the standard position, (b) tilted away from the detector, (c) tilted towards the detector.

In order to avoid disturbing the measurements due to effect of preferential absorption of Al X-rays discussed above, all the linescans presented in the thesis were measured with the coating directly facing the detector, the same orientation being carefully selected for all the samples.

Chapter 4: Changes in the morphology and composition of coatings growing on sharp edges and corners

A schematic view of the plasma sheath around biased wedge coated by ion-assisted PVD is shown in Fig.4-1. Due to the shape of the sheath, which is curved and contracted towards the edge, there will be more ions bombarding the edge region and their angle of incidence will change from perpendicular to the substrate (far from the edge) to parallel to the wedge axis of symmetry (right at the edge). The change towards more oblique angles of incidence near the edge will increase the sputtering yield of the ions (Andersen, 1981), which combined with the higher ion flux will increase the sputtering rate of the ions. We can therefore expect that there will be a region close to the edge in which the growing coatings will be subjected to increased ion bombardment. The impact it will have on the coating properties is analysed in this chapter. We examine separately the edge region in the middle of the wedge-shaped samples (section 4.1.) and the region close to the corners (section 4.3.) - both marked in Fig.3-1.

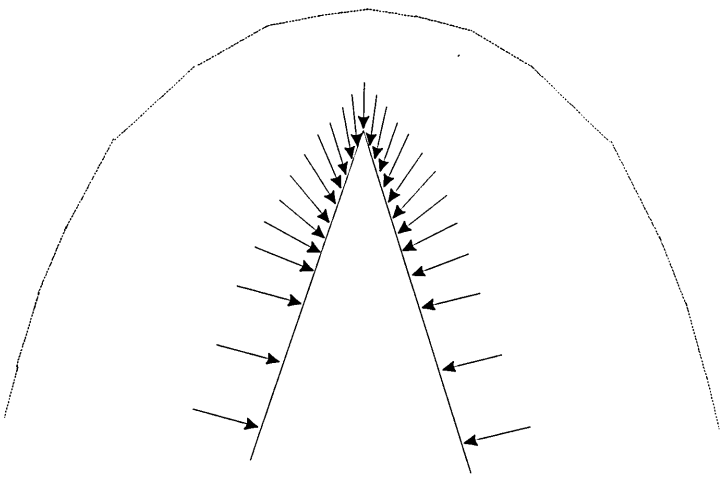

Fig.4-1: Schematic drawing of the two-dimensional plasma sheath around a biased wedge. The plasma sheath boundary (represented by the solid line) is contracted towards the edge and the ions (represented by the arrows) hit the surface in the edge region at changing angles of incidence.

4.1. Changes as a function of the edge angle and the substrate bias

Fig.4-2 presents top-view of wedges with different edge angles coated at different substrate bias values. Under same conditions, a coating deposited on flat samples is homogenous. In the edge region of the wedge-shaped samples we observe three different morphologies:

- homogenous coating (90° wedge coated at -75V and 45° wedge coated at -75V)
- coating breaking (at some places) along the edge line (30° wedge coated at -75V, 45° wedge coated at -105V and 90° wedge coated at -150V)
- coating missing completely from the edge area (30° wedge coated at -150V and 45° wedge coated at -150V).

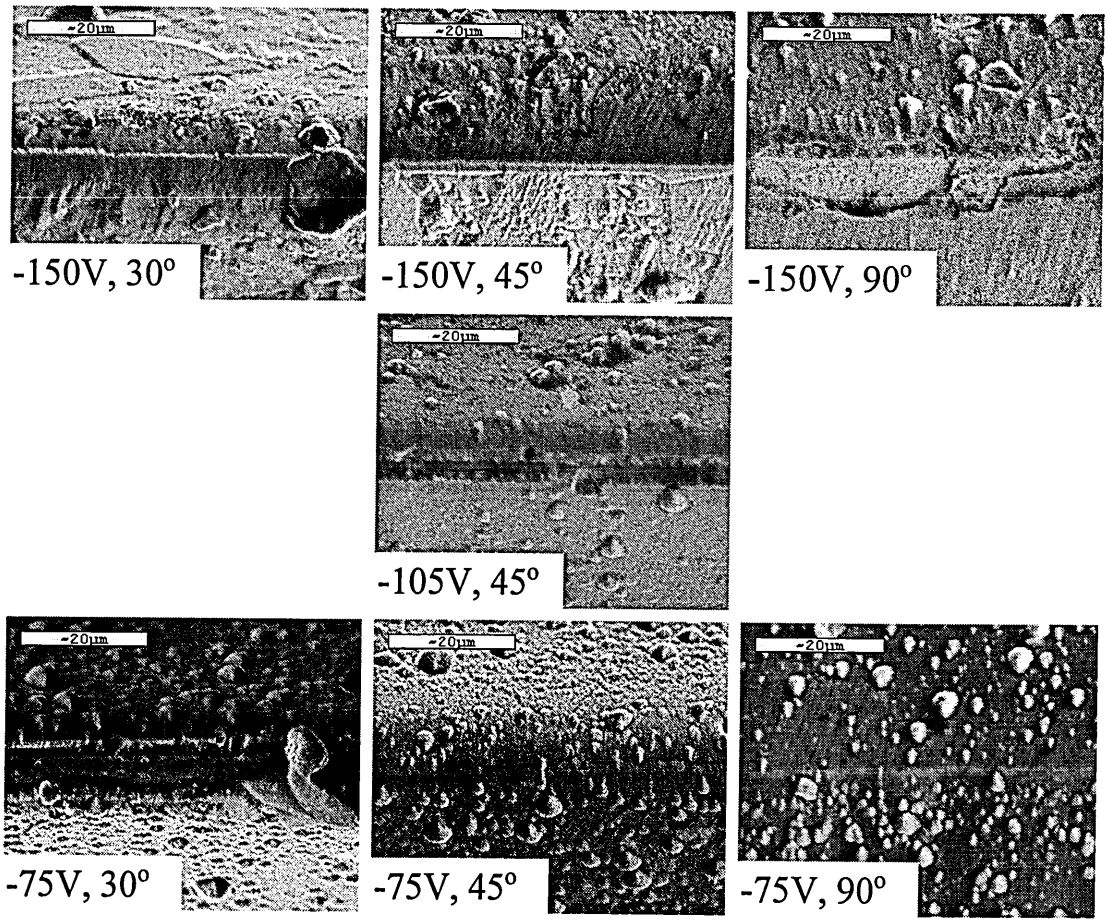

Fig.4-2: Top view of the coated wedges. The horizontal line in the middle of the images is the edge line. The small spherical objects spread all over the pictures are coating defects called droplets.

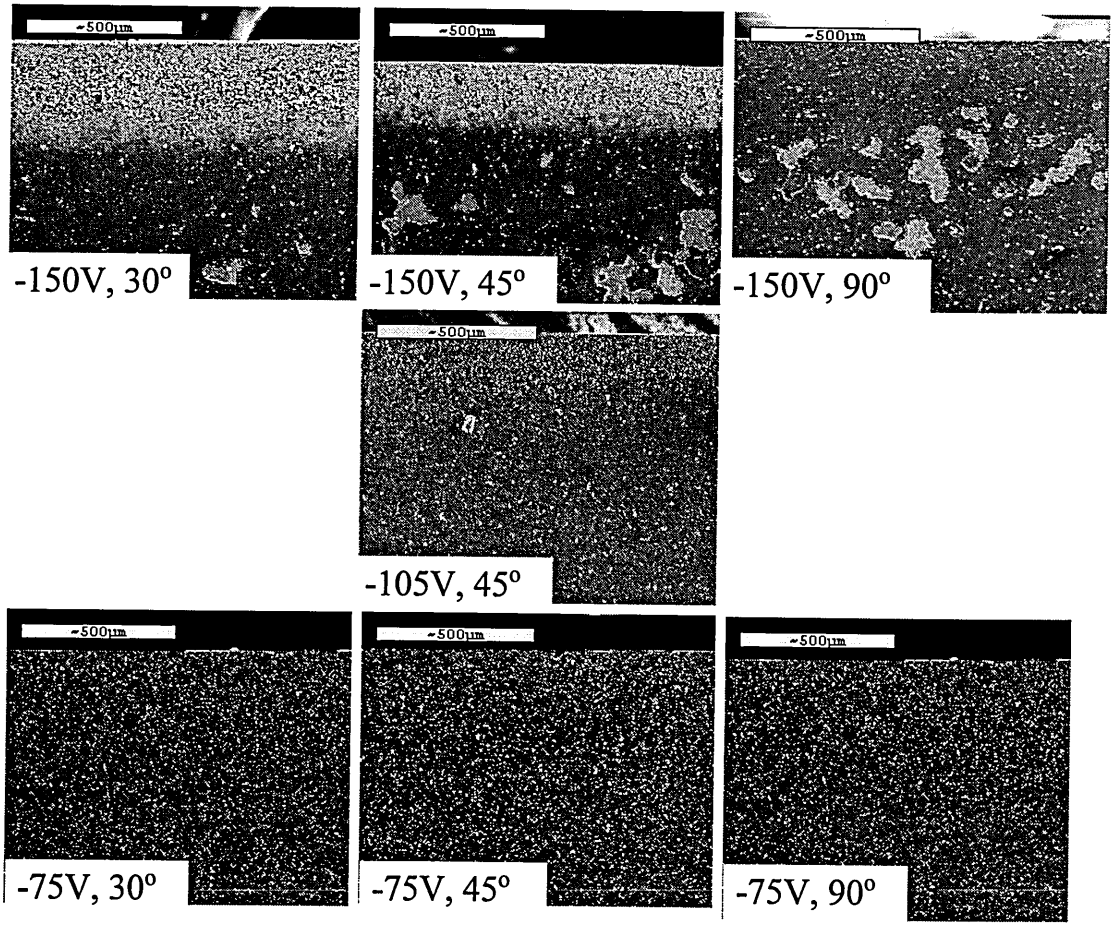

Fig.4-3: Side view of the coated wedges. The edge line is the horizontal line in upper part of the image.

Side-view analysis of the wedges, presented in Fig.4-3, reveals that the morphological changes are not limited to the edge itself, but extend to the area around the edge. This can be clearly seen on samples coated at -150V, where further changes in the coating morphology can be observed as a function of the distance from the edge (d). They are shown in more detail in Fig.4-4 for the 30° wedge coated at -150V: the coating is homogenous for $d > 1$ mm, the coating partially delaminates for $1 \text{ mm} > d > 0.5$ mm, and the coating is missing completely for $d < 0.3$ mm. The situation is similar for the 45° wedge coated at -150V, as shown in Fig.4-4 where For the 90° wedge coated at -150V, the side-view shows the coating delaminating at some places. For other samples the coating looks homogenous from the side.

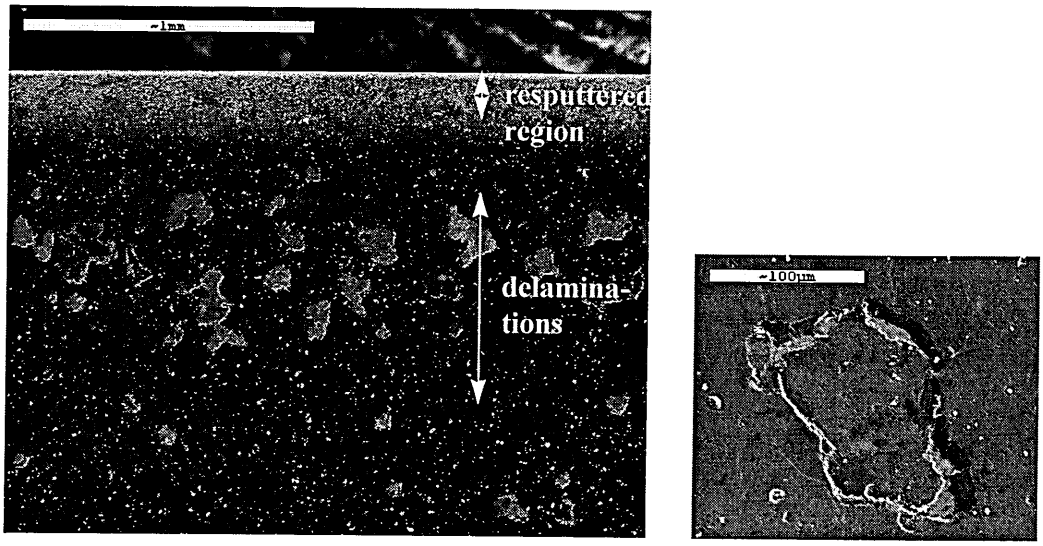

(a) (b)

Fig.4-4: Side-view of 30° wedge coated at -150V. The edge line is the horizontal line in upper part of the image. The brighter areas correspond to exposed substrate.

The composition of the coatings in the edge region was studied by EDX. Since Al has higher component sputtering yield than Ti or V (Andersen, 1981), we can expect that Al will be preferentially resputtered from the growing film and that this effect will be enhanced in the edge region. In order to assess the Al depletion we have chosen to compare the Kα X-ray signal ratio from Al and from Ti. By comparing the Kα(Al)/Kα(Ti) ratio measured far from the edge with the same ratio measured in the edge region, a direct estimate of the change in the Al/Ti mass concentration could be obtained (as discussed in section 3.3.1.). Fig.4-5 shows a typical set of EDX linescans measured on the 90° wedge coated at -150V. The X-ray signal from Al is decreasing towards the edge while the Ti signal is slightly increasing. This indicates that the Al concentration in the edge region is indeed lowered and that the Al-atoms are to some extent replaced by Ti (and V). Fig.4-6 shows the Al/Ti X-ray ratio as a function of the distance from the edge for all wedges. We can see that the Al depletion can be observed on all the samples and that it is enhanced with increasing the substrate bias and/or decreasing the wedge angle. The change is maximal for the 30° wedge coated at -150V, where the value of the Al/Ti ratio at ~ 0.3 mm from the edge is lower by ~ 60% compared to the value far from the edge. Closer to the edge, the coating was resputtered completely therefore the signal is missing in this part of the graph.

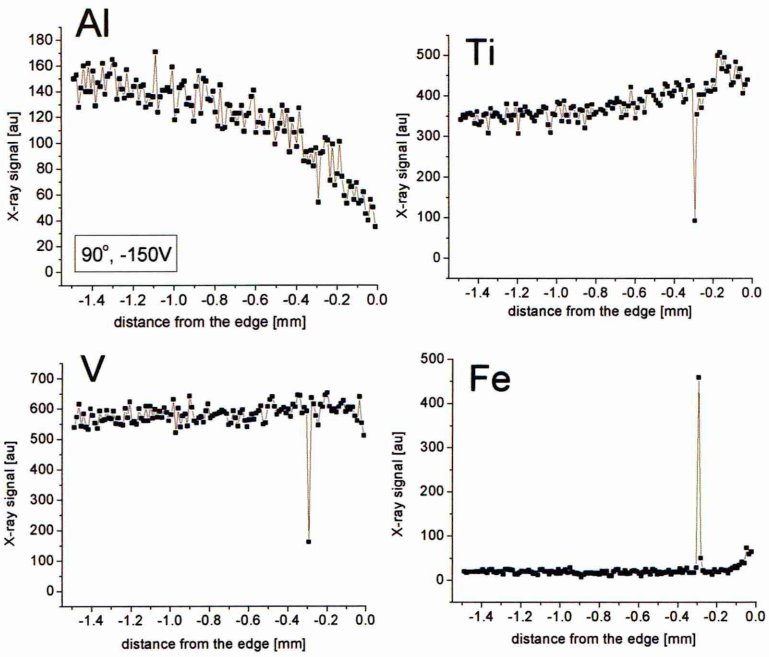

Fig.4-5: EDX linescans measured on 90° wedge coated at -150V. The concentration of Al is decreasing, while that of Ti is increasing, towards the edge.

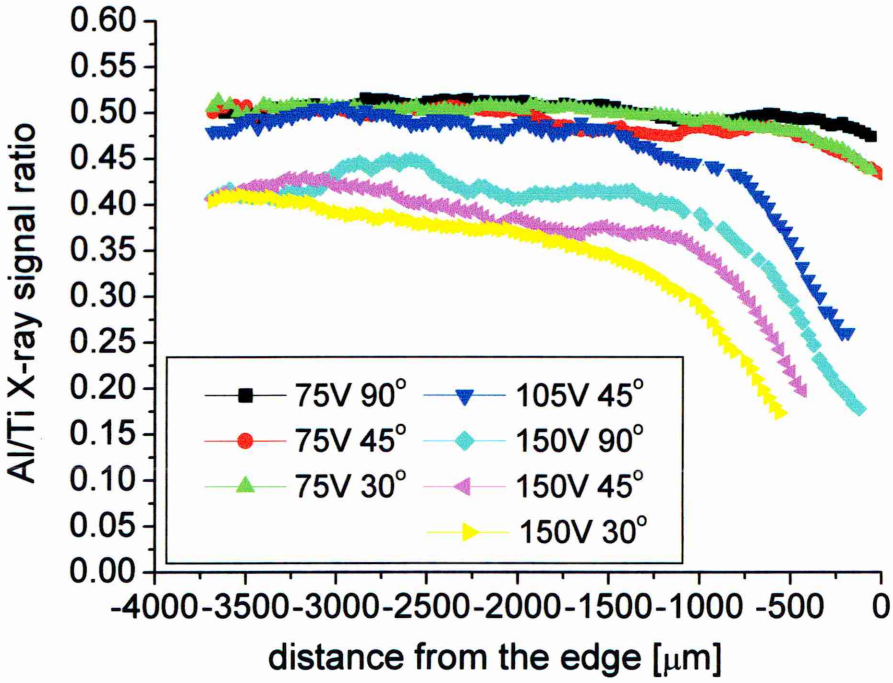

Fig.4-6: The Al/Ti Kα X-ray ratio as a function of the distance from the edge for all the wedges.

The change in the composition is accompanied by a change in the thickness of the coatings. Cross-sectional samples prepared from the 45° wedge coated at -105V and the 90° wedge coated at -150V have shown decreasing thickness in the edge region. In Fig.4-7 the coating thickness as a function of the distance from the edge is plotted together with the corresponding Al/Ti ratio. It shows clearly the distinctive region - starting at ~1 mm from the edge for the two wedges shown - in which the coating properties are changing. The spatial extent of this 'edge-affected region' for all the samples is shown in Fig.4-8. At a certain distance from the edge, the edge-related effects appear - the composition of the coating, as well as the shape of the droplets (see section 4.4), start to change. This distance, which is specific for each sample, marks the beginning of the edge-affected region in which the properties of the coatings are altered. The figure shows that the extent of this region is a function of the substrate bias and the geometry of the wedge. The length of the edge-affected region is ranging from ~300 μm for the 90° wedge coated at -75V to ~1250 μm for the 30° wedge coated at -150V. The extent of the region in which the coating is delaminating on the wedges coated at -150V is also marked in the figure. The delaminations start together with the other effects at the beginning of the edge-affected region and at a particular distance closer to the edge they disappear. For the 30° and 45° wedges coated at -150V, the spatial extent of the completely resputtered region close to the edge is shown as well. The length of this 'critical region' is ~200 μm for the 45° wedge and ~300 μm for the 30° wedge.

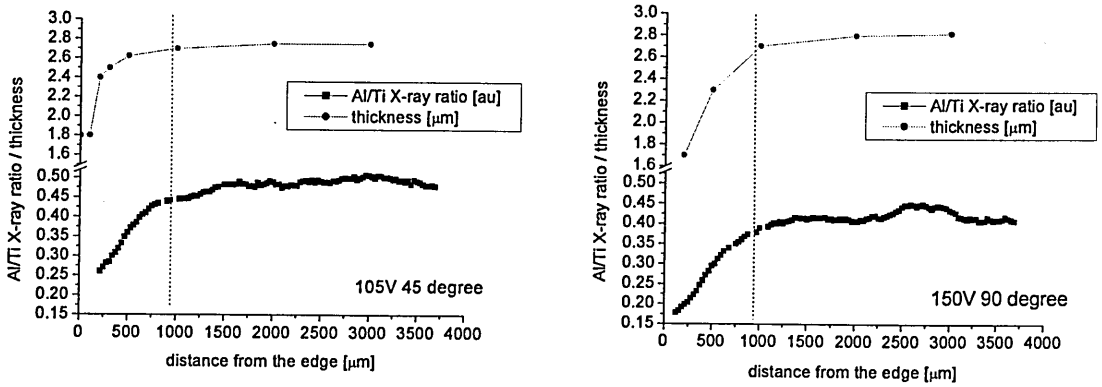

Fig.4-7: Changes in the thickness of the coating as a function of the distance from the edge, plotted together with the compositional profile, observed on: (a) 45° wedge coated at -105V, (b) 90° wedge coated at -150V.

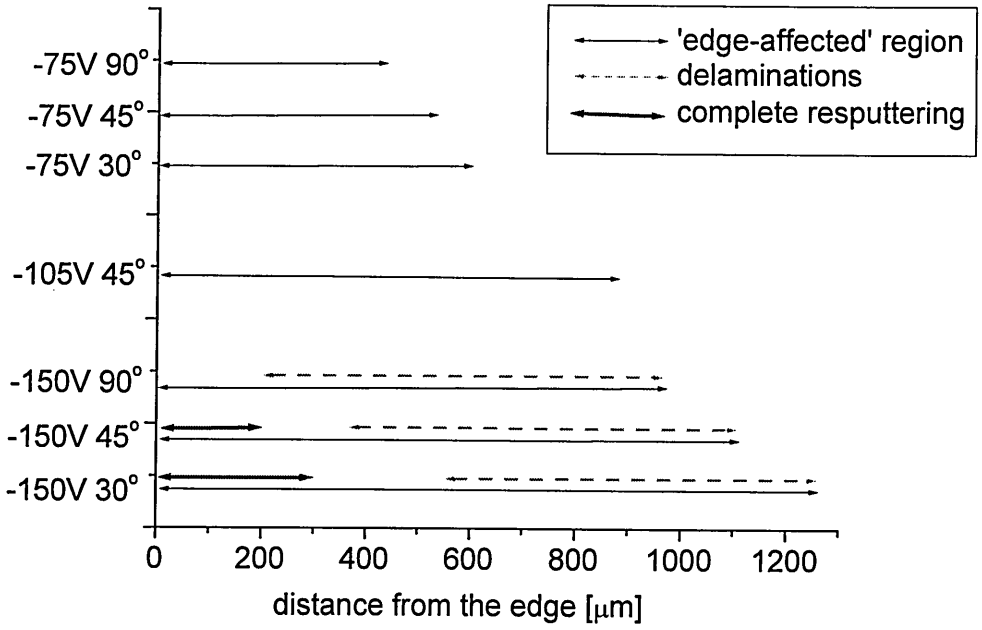

Fig.4-8: The spatial extent of the distinctive regions observed on the side of the wedges: the edge-affected region (solid line), the delaminations region (dashed line) and the completely resputtered region (bold line).

In order to elucidate the influence of the different parameters on the changes in the edge region, we have summarised the different morphologies observed in form of a 'zone diagram' presented in Fig.4-9. In this diagram each 'zone' corresponds to one of the morphologies described above. At low substrate biases, for less sharp edges, the coating formed in the edge region is homogenous - this corresponds to the 'zone 1'. At high substrate biases, for very sharp edges, there is no coating at all close to the edge - this is characteristic for the region of the graph denoted as 'zone 3'. In between these two extremes, the 'zone 2' represents the situation when the coating is present in the edge area but is breaking (completely or partially) along the edge line.

Both the parameters - the edge angle and the substrate bias - are affecting the magnitude of the ion bombardment and are therefore changing the proportion of the resputtering of the growing coating by the ions relative to its growth. By increasing the substrate bias, the energy of the ions will be increased which means higher sputtering yield. In the case of a curved plasma sheath this will also slightly increase the ion flux since higher substrate bias means larger plasma sheath width (see Eq.2-6 in Chapter 2) -

which means that ions from a larger area will be attracted to the edge region. The increase in ion flux and in ion energy will both cause an increase in the amount of resputtering. By increasing the sharpness of the edge (which means decreasing the wedge angle), we increase the ion flux (the sheath will be 'more curved') and the angle of incidence of the ions (because of the change in the geometry) - which again enhances the resputtering. This corresponds to the trend visible in Fig.4-9 - as we increase the substrate bias and/or decrease the angle of the edge, the resputtering becomes more and more significant leading finally to a situation where it completely hinders the growth. Hence the three different situations:

1.) The coating in zone 1 is uniform. The amount of resputtering is relatively low at this bias and geometry. However the ions still affect the internal properties of the coating. We have seen the change in the composition (Fig.4-6). The changes in the microstructure of these coatings will be analysed in Chapter 6.

2.) The coating in zone 2 grows under higher amount of resputtering. This causes a much more significant change in composition (Fig.4-6) and the examination of cross-sections from the wedges reveals that because of the high amount of resputtering, the thickness of the coatings near the edge is reduced. Both the change in the thickness and in the composition lead to a change in the stress inside the film, which is critical at the edge where the coating is curved. This can cause the coating to break along the edge line.

3.) In the zone 3 the effect of the ions is the most spectacular. Here, as the properties of the coatings start to change at the beginning of the edge-affected region, the stress becomes already critical and the coating starts to disintegrate. At a certain distance close to the edge, the stress starts to decrease - the delaminations disappear. This can be connected to the change in the film thickness which is decreasing rapidly towards the edge. The 'critical thickness', for which the stress inside the coating decreases, is reached at ~200 μm from the edge for the 90° sample, at ~350 μm for the 45° and at ~550 μm for the sharpest 30° wedge where the coating thickness decreases the most rapidly. In a specific region close to the edge, the sputtering rate becomes so high that it completely overpowers the growth - there is no coating deposited in this region. The severe ion bombardment in these conditions will also significantly alter the substrate topography (which will be analysed in Chapter 5).

The spatial extent of the edge-affected region is related to the magnitude of the effects - the greater the relative contraction of the plasma sheath is at the edge, the more far from the edge the disturbance can be felt. The spatial extent thus follows the same trend and increases with the substrate bias and/or the sharpness of the edge (Fig.4-8).

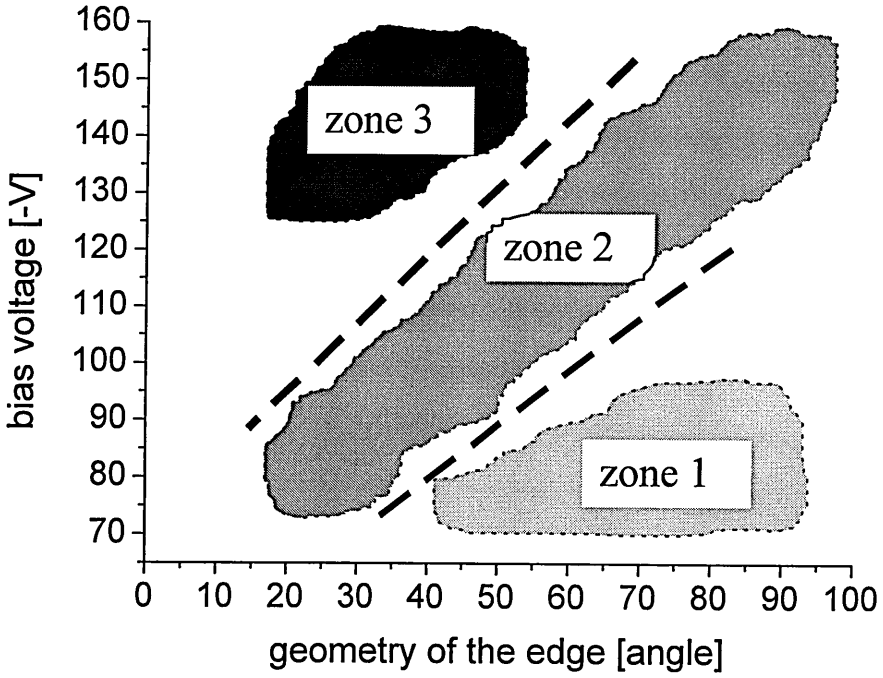

Fig.4-9: Zone diagram summarising the different morphologies observed in the edge region as a function of the wedge angle and the substrate bias. In the edge region of samples situated in 'zone 1' the coating is homogenous. For the samples from 'zone 2' the coating breaks along the edge line. On the samples from 'zone 3' there is no coating left in the edge area.

4.2. Changes as a function of the edge radius

The effect of the radius of curvature of the edge on the edge-related changes was examined on cross-sectional samples from the region on top of the edge. Wedges with angles 30°, 45° and 60°, coated with TiAlCrYN at -75V, were used in these experiments. A cross-section from the 30° wedge is shown in Fig.4-10a. By measuring the EDX compositional profiles across the coating (as marked in the figure), we were able to measure the composition in layers with different radii of curvature. At the

substrate-coating interface, the radius of the surface is very small - less than 1 μm, while near the top of the coating, the radius of the growing surface is increased to ~5 μm. The EDX linescan across the coating in the edge region was compared with a linescan across a flat coating - shown in Fig.4-10b.

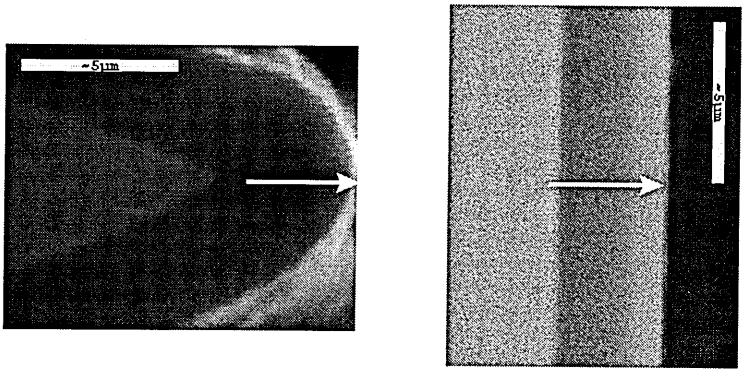

(a) (b)

Fig.4-10: Schema of the EDX measurements in the case of cross-sectional samples. The electron probe was scanned: (a) across the coating on top of the wedge, (b) across a flat coating.

The compositional profiles are presented in Fig.4-11. The gradient in the composition across the flat coating is due to the changes in the deposition process with time, most probably due to slow target poisoning during the deposition. The relative values, unaffected by this effect, are also shown in the figure. The greatest Al-depletion can be observed close to the interface, where the growing surface is the sharpest: ~14% for the 30° and ~10% for the 60° wedge. The depletion is decreasing towards the flat coating value as the radius increases (that is, as the distance from the substrate-coating interface increases). For the sharpest 30° wedge, the composition even near the end of the coating is however still ~12% different from composition of the flat coating.

The effect of a significantly different radius of curvature of the edge was also studied. Fig.4-12 shows the compositional profiles across the coating for two wedges having the same angle - 60° - but two very different initial radii: ~2 and ~250 μm. The composition values measured on the rounded edge - which disturbs the electric field in its vicinity much less than a sharp edge - are very close to the values corresponding to the flat coating.

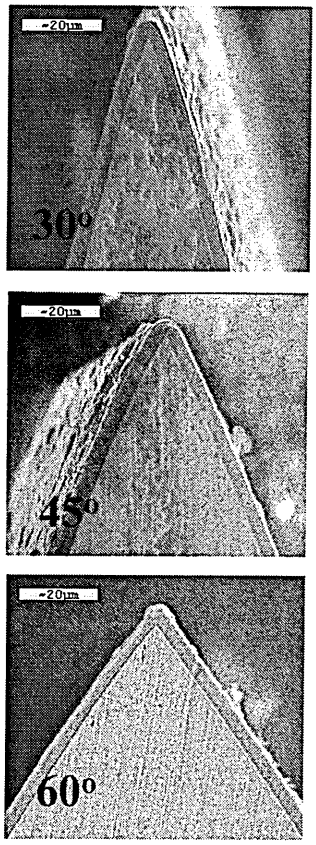

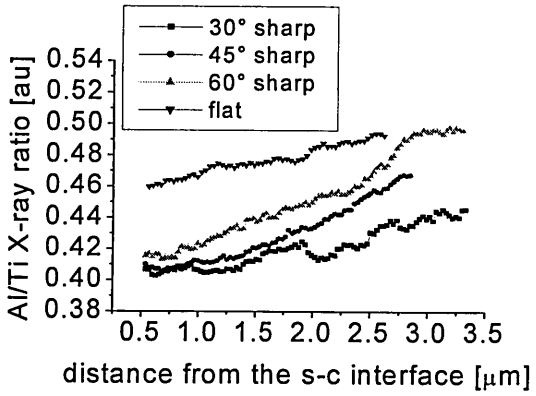

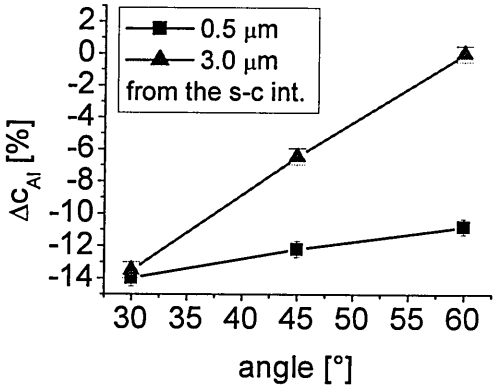

Fig.4-11: Al/Ti Kα X-ray ratio scanned across the coating on top of sharp wedges with angles 30°, 45° and 60° (shown on the SEM micrographs), and across a flat coating. All the samples were coated at -75V.

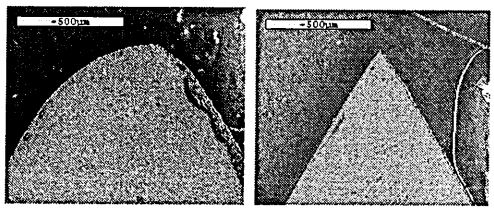

60°: 100μm vs. 2μm

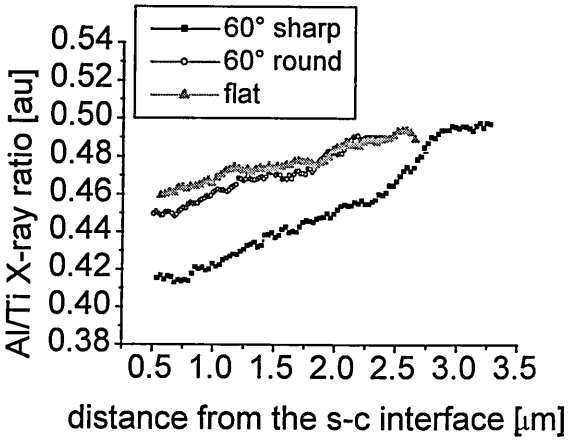

Fig.4-12: Al/Ti Kα X-ray ratio scanned across the coating on top of wedges with angle 60° and radius of curvature (a) 100μm, (b) 2 μm; compared with the profile measured across a flat coating. The wedges were coated at -75V.

4.3. Enhancement of the changes at sharp corners

A comparison between the morphology in the edge region and in the corner region for different wedges is presented in Fig.4-13.

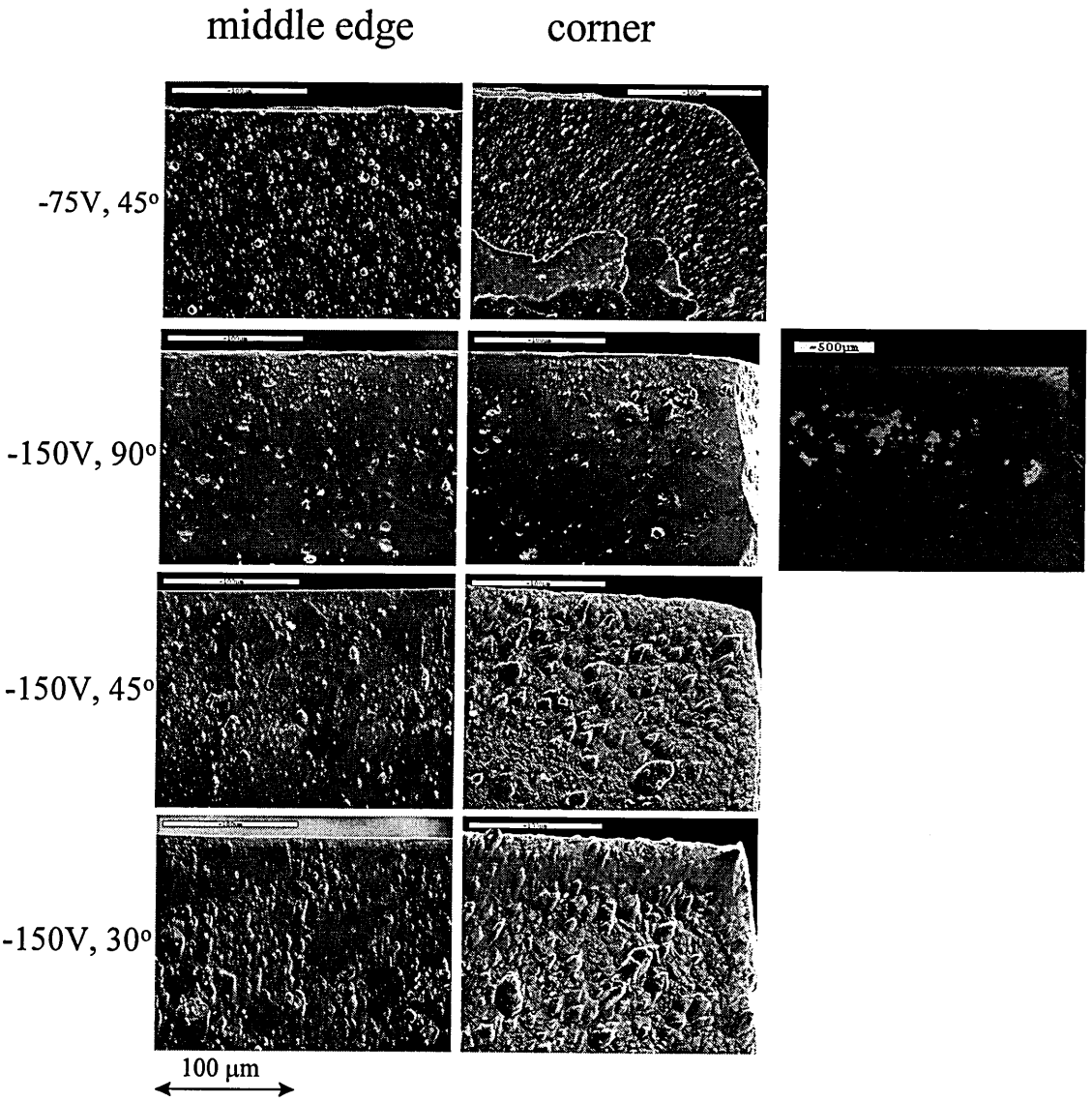

Fig.4-13: Comparison between the morphology of the coating in the middle and at the corner of the same wedge, for several different wedges. In the case of 90° wedge coated at -150V, Fe compositional map taken by EDX at a lower magnification is also attached.

For the 45° wedge coated at -75V, the coating in the corner is breaking along the edge - as in the middle of the wedge - but is also partially delaminating on the side. Similar situation was observed for all the wedges coated at -75V. For the 45° wedge coated at -105V, a significant decrease in the coating thickness was observed close to the corner (not shown here). The coatings deposited in the corner region at the highest bias -150V were affected by the ions in the most spectacular way. For the 90° wedge, the coating close to the corner was completely resputtered - which can be seen from the compositional map (taken by EDX). A closer look reveals that the ions have also slightly altered the substrate topography in this region. The effects are much more pronounced in the corner region of the 30° and 45° wedges, where the ions have not only completely resputtered the coating but have also created complex topographical features - such as ripples and cones.

Low magnification side-views of the two samples are presented in Fig.4-14. We can see clearly the gradual increase in the spatial extent of the completely resputtered region towards the corner. The increase in the spatial extent of the edge-affected region for all the wedges coated at -150V is presented in Fig.4-15. For the sharpest 30° sample, the region is more than 3 mm wide, which is ~2.6-times more than in the middle of the wedges.

The compositional changes are also enhanced at the corners. In part I the Al/Ti Kα X-ray signal ratio in the middle of the wedges was found to decrease towards the edge. Fig.4-16 compares the decrease of the Al/Ti ratio close to the edge relative to that far away - for the middle of the wedges and the corners. The magnitude of the Al-depletion, a function of the wedge angle and the substrate bias, is substantially enhanced at the corners. For the 30° wedge coated at -150V the Al/Ti ratio is decreased by up to ~60% close to the edge, in the corner - by up to ~70% (Fig.4-17).

The enhancement of the magnitude and spatial extent of the changes at the corners is related to the 'three-dimensional' geometry of the corner. The area from which ions can be attracted towards the corner is much larger than in the middle of the wedge, which means that the coating growing in the corner region is affected by even greater increase in the ion bombardment. This will also affect the shape of the plasma sheath near the corner and thus the spatial extent of the changes. Detailed analysis of this phenomenon will be done in Chapter 5. For the same reasons as before, the changes

are more and more significant with increasing the substrate bias and/or increasing the sharpness of the corner but, compared to the middle of the wedges, the zone diagram in Fig.4-9 would be shifted towards the origin of the graph. Due to the increased ion bombardment, the same type of morphology as in the middle of the wedges occurs at lower energy or for less sharp angle in the corners.

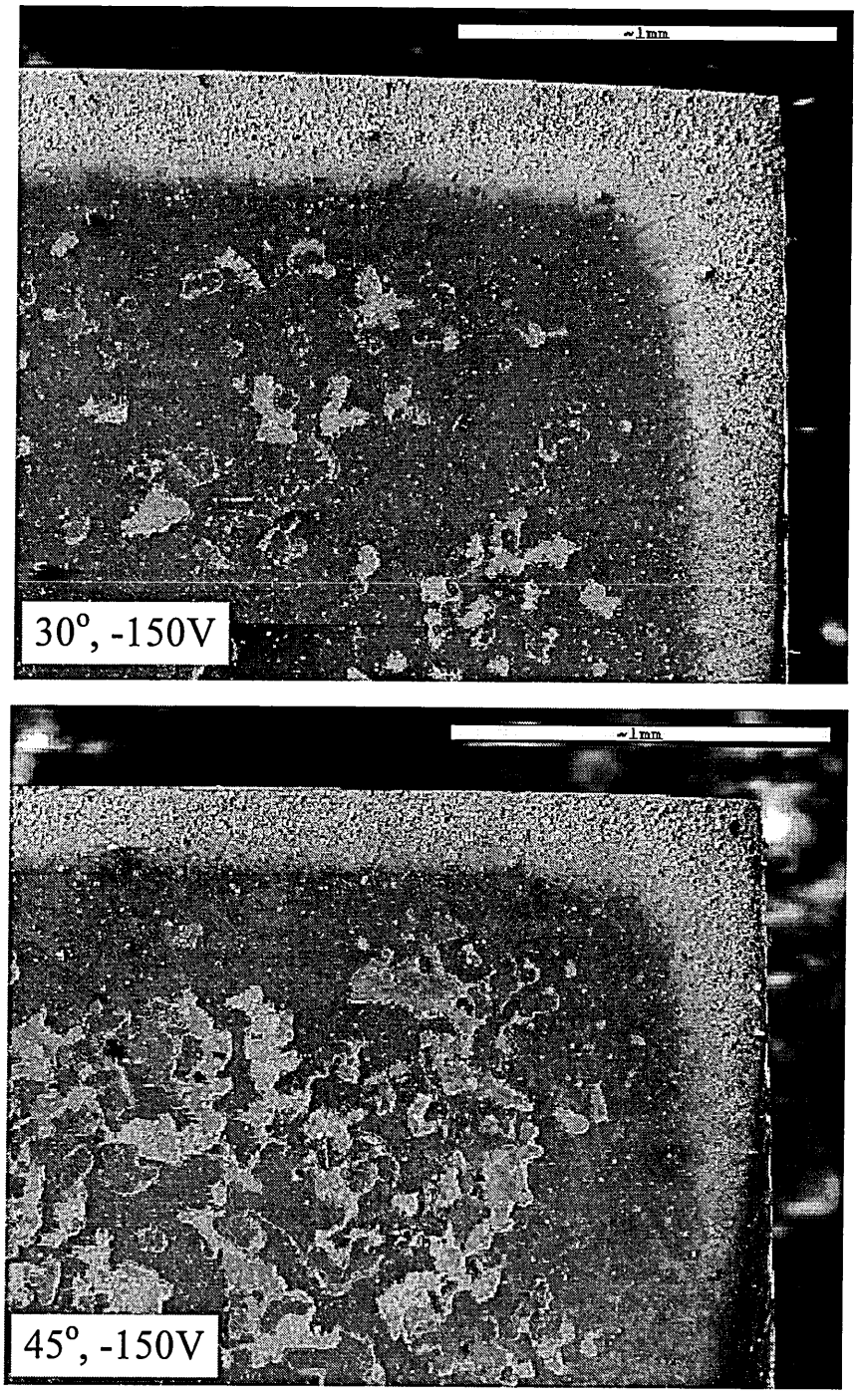

Fig.4-14: Low magnification side-view of the corner region of 30° wedge and 45° wedge, both coated at -150V.

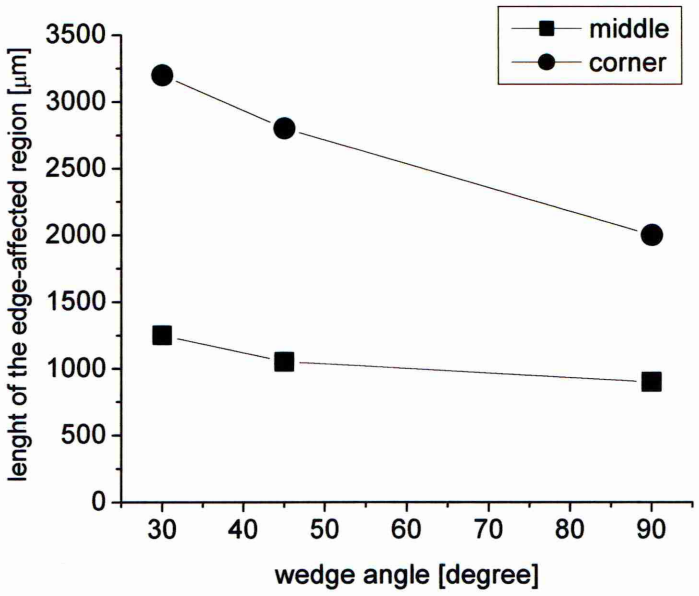

Fig.4-15: Spatial extent of the edge-affected region as a function of the wedge angle - in the middle of the wedges and in the corner.

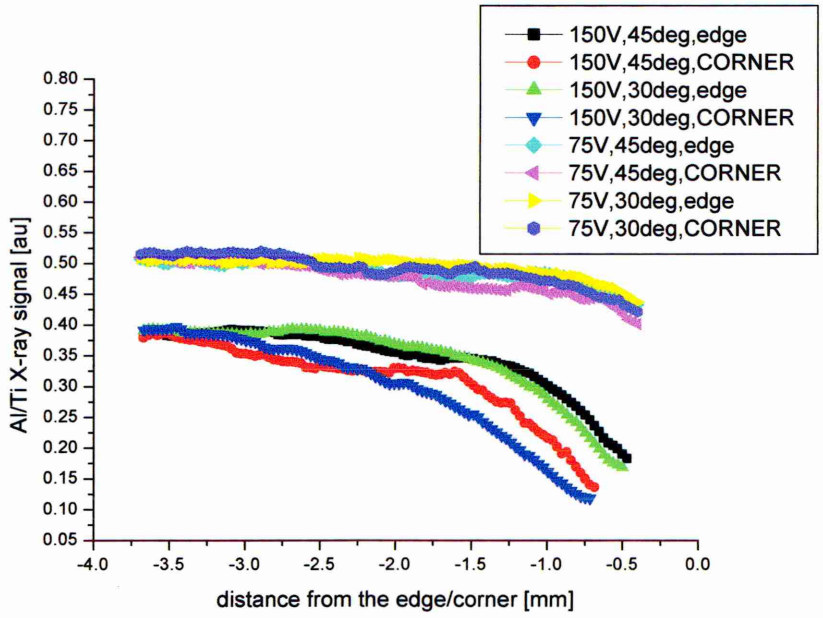

Fig.4-16: Comparison of the Al/Ti EDX linescans taken in the edge region - in the middle of the wedges and at the corners.

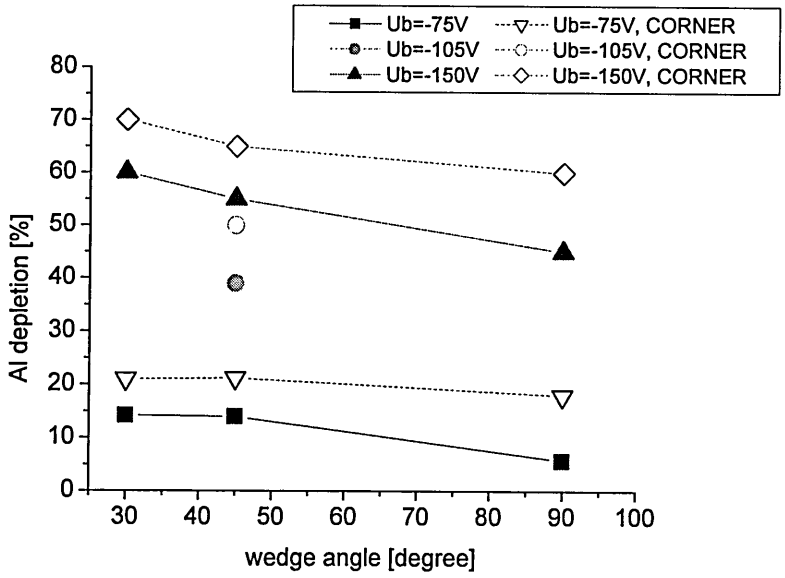

Fig.4-17: The amount of the Al-depletion as a function of the wedge angle and the substrate bias, measured in the middle of the wedges and at the corners.

4.4. Droplets

The small spherical particles visible on all the wedges where the coating is not completely resputtered (see for example Fig.4-2) are coating defects caused by 'droplets' - macro particles of target material incorporated into the coating. During the etching phase prior to the coating deposition these particles, emitted from the target as the arc locally and rapidly melts the material, are displaced to the substrate and are then covered with the coating during the magnetron sputtering. On flat surfaces the droplets and the coating on top of them have always a spherical shape, with the diameter depending on the melting point of the target material (Petrov, 1997 and Creasey, 1997). A closer examination of the wedges reveals that the droplets in the edge region are non-symmetrical. Fig.4-18 shows the typical shape of the droplets - they are much narrower on one side, pointing towards in the edge in the middle of the wedges and towards the corner in the corner area. This corresponds well with our model of the plasma sheath around the wedges which implies change in the angle of incidence of the ions - from perpendicular to the substrate far from the edge to along the edge/corner axes of symmetry. Due to the oblique angles of incidence, any protrusion - such as an initially

spherical droplet and the coating on top of it - will be bombarded more from one side than from any other and will thus become much narrower in the direction of the ions arrival. The more oblique the angle, the more non-symmetrical it will be - as can be seen from the comparison between the 90° and 30° wedges coated at -75V.

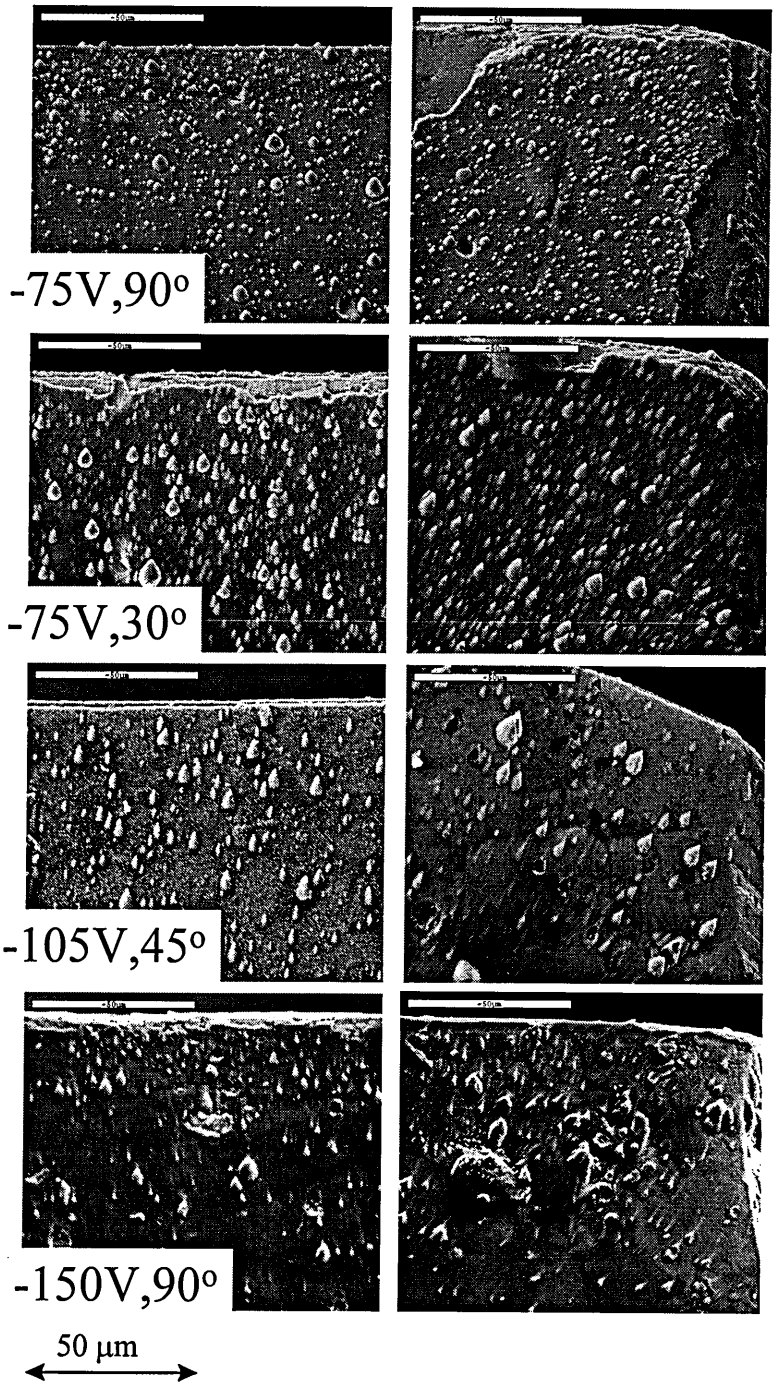

Fig.4-18: SEM micrographs showing the shape and the distribution of droplets on different wedges, in the middle of the wedge and at corners.

The change in the shape as a function of the distance from the edge can be seen in the next figure on the example of 30° wedge coated at -75V. The defects have conical shape close to the edge (Fig.4 -19a), while at a distance ~500 μm from the edge (Fig.4-19b) - where the edge-affected region is only just beginning (see Fig.4-8) - they are almost perfectly round.

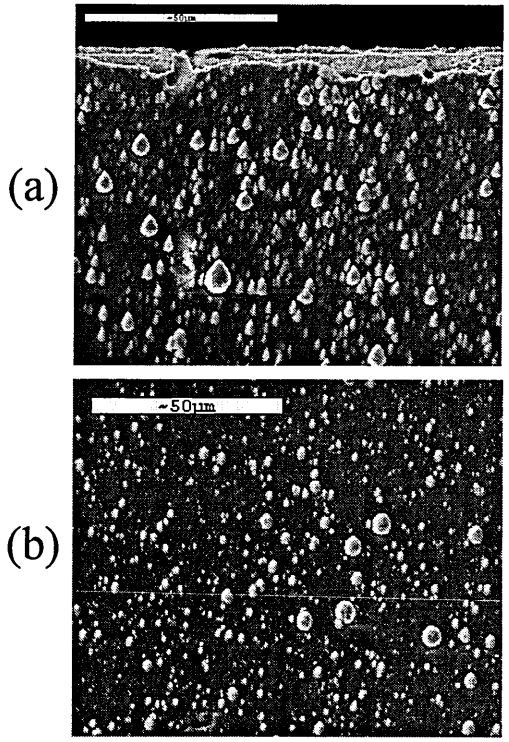

Fig.4-19: SEM micrographs showing the shape and the distribution of droplets on 30° wedge coated at -75V: (a) near the edge, (b) at 500 μm from the edge.

4.5. Effect of the substrate polishing

The initial roughness of the substrate also plays an important role during the deposition on flat samples. The reason for this is in fact connected to edge-related problems - any significant alteration from the perfectly flat surface can change to some extent the shape of the plasma sheath and thus the local properties of the coating. The effects can be even more important when coating sharp wedges, as the increased ion bombardment in the edge region could enhance the changes. An example is presented in Fig.4-20 which shows top-view of two corners of the same 90° wedge coated at -75V. The corner shown in Fig.4-20a was mirror polished and the coating on top of it is

almost uniform, with only few small localised delaminations. This is in contrast with the corner in Fig.4-20b where one side was not polished and was thus left with regular scratches from the machining. On this corner, almost all the coating is delaminated, often along the scratches. In order to eliminate this effect, the initial surface of all our wedges was carefully mirror-polished, trying to get the same ideal surface for all the samples.

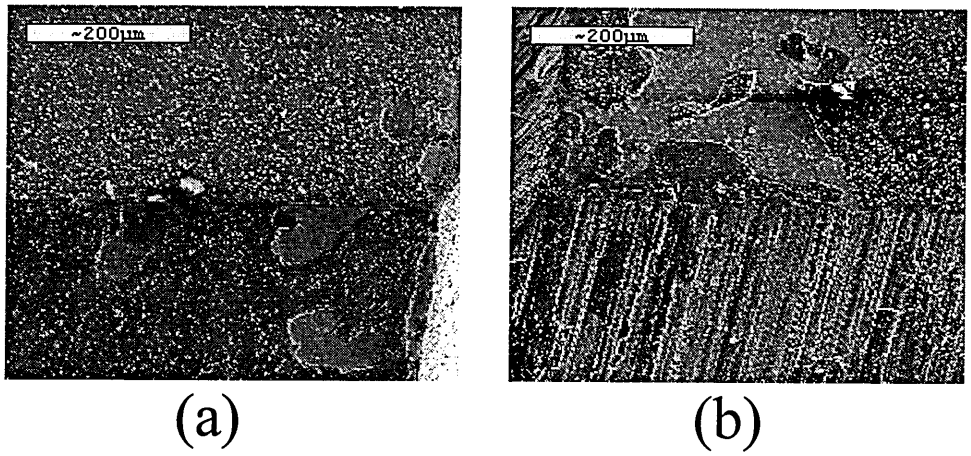

Fig.4-20: Top-view of the two corners belonging to 90° wedge coated at -75V. Prior to the coating deposition, the substrate in the corner area was: (a) mirror-polished, (b) unpolished.

Chapter 5: Plasma-surface interaction at sharp edges and corners

In order to be able to better understand and to quantify the observed changes in the properties of coatings near sharp edges and corners, we need to analyse the interaction between the wedges and the plasma during the deposition. The electric field inside the plasma sheath around wedge-shaped samples, and the resultant ion trajectories are modelled. The results from the simulations are directly compared with the experimental observations described in the previous chapter.

5.1. Shape characteristics of the plasma sheath

5.1.1. Modelling of the electric field inside the plasma sheath

The electric field inside the plasma sheath around sharp wedge-shaped samples (0° and 90°) was simulated by Watterson (1989) (see section 2.1.2.). He calculated numerically the solution of the Poisson's equation coupled with the changing space charge (self-consistent model). We have set up a similar simulation model, where approximations were used in order to simplify the calculation. It allowed us to simulate the characteristics of the plasma sheath for wedges with different geometries (different angles and radii of curvature). Furthermore, the simplified form of the model enabled us to extend the two-dimensional edge geometry, relevant for the edge region in the middle of the wedges, into three-dimensions and thus describe the situation at the corners of the wedges.

Our first approximation was to neglect the effect of the space charge, which allowed us to calculate the electric field using QUICKFIELD simulation program (http://www.quickfield.com). The program calculates numerically the solution of the electrostatic Poisson equation with specified boundary conditions. The schema of our model is shown in Fig.5-1. We have selected the sample surface to be at the potential equal to the applied bias ($\phi_o = U_b$), while the plasma boundary was set to zero. The important part was the selection of the potential profile across the plasma sheath ($\phi = f(x)$). The function should ideally be potential profile of the sheath above the flat

substrate (as it is set for a region far from the edge), which is given by Child-Langmuir equation (see section 2.1.1.) as:

$$\Phi = -V_o\left(\frac{x}{s}\right)^{4/3}, \qquad \text{(Eq.5-1)}$$

with the plasma sheath width - s - equal to:

$$s = \frac{\sqrt{2}}{3}\frac{\varepsilon_0^{1/2}\varphi_0^{3/4}}{n_s^{1/2}T_e^{1/4}}, \qquad \text{(Eq.5-2)}$$

where n_s is the ion density in the plasma and T_e the average electron temperature. We have used the same dimensionless parameters as in the simulations by Watterson to enable direct comparison of the results. The following transformations were used for the potential (φ), ion flux density (n) and the spatial coordinates (r):

$$\varphi' = \varphi / \varphi_0, \qquad \text{(Eq.5-3)}$$

$$n' = n / (n_s\delta), \qquad \text{(Eq.5-4)}$$

$$r' = r / (\varepsilon_0\varphi_0/en_s\delta)^{1/2}, \qquad \text{(Eq.5-5)}$$

where the parameter δ is equal to the square root of the ratio between the initial and final energy of the ions travelling through the sheath:

$$\delta = (m_i v_s^2 / 2e\varphi_0)^{1/2}, \qquad \text{(Eq.5-6)}$$

m_i being the ion mass and v_s their speed at the sheath boundary. In this system of coordinates the y-component of the equation Eq.5-1 becomes:

$$\varphi \approx -(1-3y/2)^{4/3}, \qquad \text{(Eq.5-7)}$$

and the potential is varying from -1 (at y = 0 - the sample) to 0 (at $y = y_p = 2/3$ - the sheath boundary). Our second approximation was to simplify the potential profile in Eq.5-7 into a linear function:

$$\varphi \approx -(1-2y). \qquad \text{(Eq.5-8)}$$

This linear variation of potential corresponds to the case of flat sample in vacuum, where the electric field is constant (Eq.2-8 in Chapter 2). The comparison of the two potentials shown in Fig.5-2. The two function are almost equal close to the sample surface, where the disturbing effect of the plasma is the smallest. The maximum error across the sheath, occurring close to the sheath-plasma boundary, is ~1/3.

Our model assumes that the relative change in the shape of the plasma sheath is mostly determined by the edge geometry, while the dependence on the bias voltage is

relatively weak. Watterson in his simulations has shown that this assumption is valid for small values of the parameter delta defined in Eq.5-6 (the shape coefficients of the sheath varied only by ~10% for delta between 0.1 and 0.25). Using Bohm's formula for ion acceleration in the pre-sheath region (Bohm, 1949) in order to determine $v_{s,,}$ we have estimated delta to be ~0.1 in our conditions (substrate bias -150V and electron temperature 3eV).

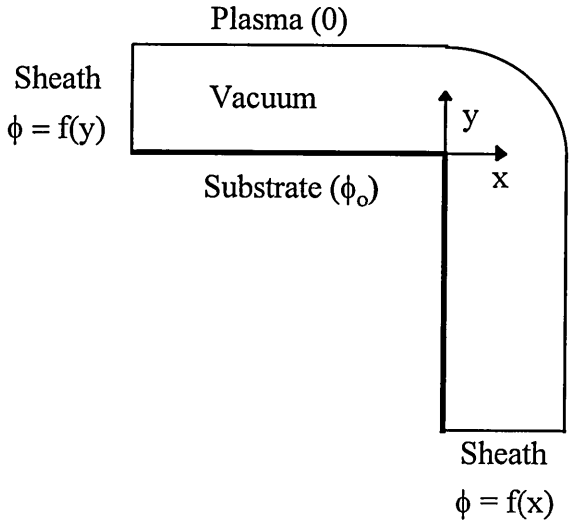

Fig.5-1: Schematic drawing showing the set-up of the simulations of the electrostatic field inside the plasma sheath around edges.

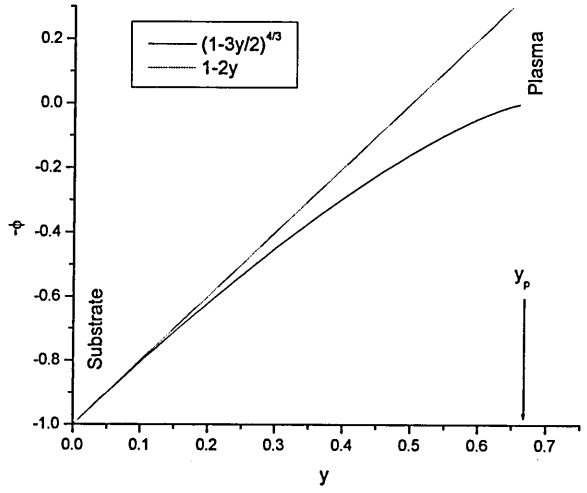

Fig.5-2: Potential profile in the vicinity of a flat biased surface - in vacuum and in the plasma sheath. The variables are in the dimensionless form defined in the text.

The advantage of our simplified model is that we could relatively easily calculate the characteristics of the plasma sheath even in 3D which allowed us to simulate both sharp edges and sharp corners. The geometry and the boundary conditions were extended from 2D to 3D using axial symmetry.

5.1.2. Quantification of the magnitude and spatial extent of the edge-related changes

a.) 2D simulations vs. the middle of the wedge

The simulated electric fields for three different 2D wedges with angles 0° (knife edge), 30° and 90° are shown in Fig.5-3. The field is represented by potential lines, each corresponding to a change in the potential by 20V. The lines are visibly contracted towards the edges where the electrostatic field intensity, and thus the gradient of the potential, is the strongest.

An equipotential line situated in the middle of the plasma sheath was selected in order to quantify the important shape characteristics of the sheath in the edge region:

- The spatial extent of the edge-affected region (x_s) was determined by measuring the relative distance from the edge where the equipotential line was disturbed by less than 5%, that is, where the sheath width was equal to 95% of the planar width y_p.
- In order to asses the sheath contraction at the edge (r_t), the distance of the equipotential line from the substrate at the edge was compared to that far away (equal to y_p).
- We could also get a quantitative estimate of the increase in the ion flux, by comparing the relative length of the equipotential line above a unit length of the sample surface - close to the edge and far away. Here we have used the fact that the number of ions entering the sheath is proportional to the amount of current and hence the equipotential line length.

The results are summarised in Table III. The comparison with the results simulated by Watterson shows that our electrostatic field model yields results within 25% of those calculated by the more exact self-consistent model.

	Spatial extent x_s/y_p		Sheath contraction r_t/y_p		Max. ion flux density n_{edge}/n_{flat}	
	Our model	Watterson (1989)	Our model	Watterson (1989)	Our model	Watterson (1989)
2D 0°	0.72	0.91	0.48	0.52	4.1	3.5
2D 30°	0.70	-	0.63	-	3.6	-
2D 90°	0.59	0.81	0.72	0.67	2.7	2.1

Table III: The shape characteristics of the simulated plasma sheath around 2D wedges, and the estimate of the maximum ion flux density in the edge region.

The values of the spatial extent and the sheath contraction in the table are relative to the value of the plasma sheath width above a flat surface (or far from the edge) - y_p. Its value in our conditions, as determined by plasma probe measurements, was:

$y_p \sim 0.90$ mm at $U_b = -75$V,

$y_p \sim 1.15$ mm at $U_b = -105$V, and

$y_p \sim 1.50$ mm at $U_b = -150$V.

The results from the 2D simulations can be directly related to the effects observed experimentally in section 4.1. With increasing the sharpness of the edge, the electric field in the edge region gets stronger and the plasma sheath is thus more contracted. The sheath width at the edge is ~0.7 of the width above flat surface for the 90° wedges and ~0.6 for the 30° wedges. The sheath width above a 30° edge at -75V, for example, is $\sim 0.63 \times 0.9 = 0.57$ mm, while at -150V we have $\sim 0.63 \times 1.50 = 0.94$ mm. As the contraction of the plasma sheath increases, so does the spatial extent of the disturbance. Table IV compares the experimentally observed spatial extent of the changes in the middle of the wedges and the simulated values, for two substrate biases: -75V and -150V. The maximum difference is ~ 15 %.

The implications of the increase in the ion flux in the edge region by ~2-times for the 90° wedges and by ~3.5-times in the case of 30° wedges will be discussed in section 5.3.

	Experimental value	Simulated value
-75V, 30° wedge	x_s ~0.55 mm	$x_s = 0.70 \times 0.90 = 0.63$ mm
-75V, 90° wedge	x_s ~0.45 mm	$x_s = 0.59 \times 0.90 = 0.53$ mm
-150V, 30° wedge	x_s ~1.25 mm	$x_s = 0.70 \times 1.50 = 1.15$ mm
-150V, 90° wedge	x_s ~1.00 mm	$x_s = 0.59 \times 1.50 = 0.89$ mm

Table IV: Comparison between the experimentally measured spatial extent of the edge-affected region and the simulated values.

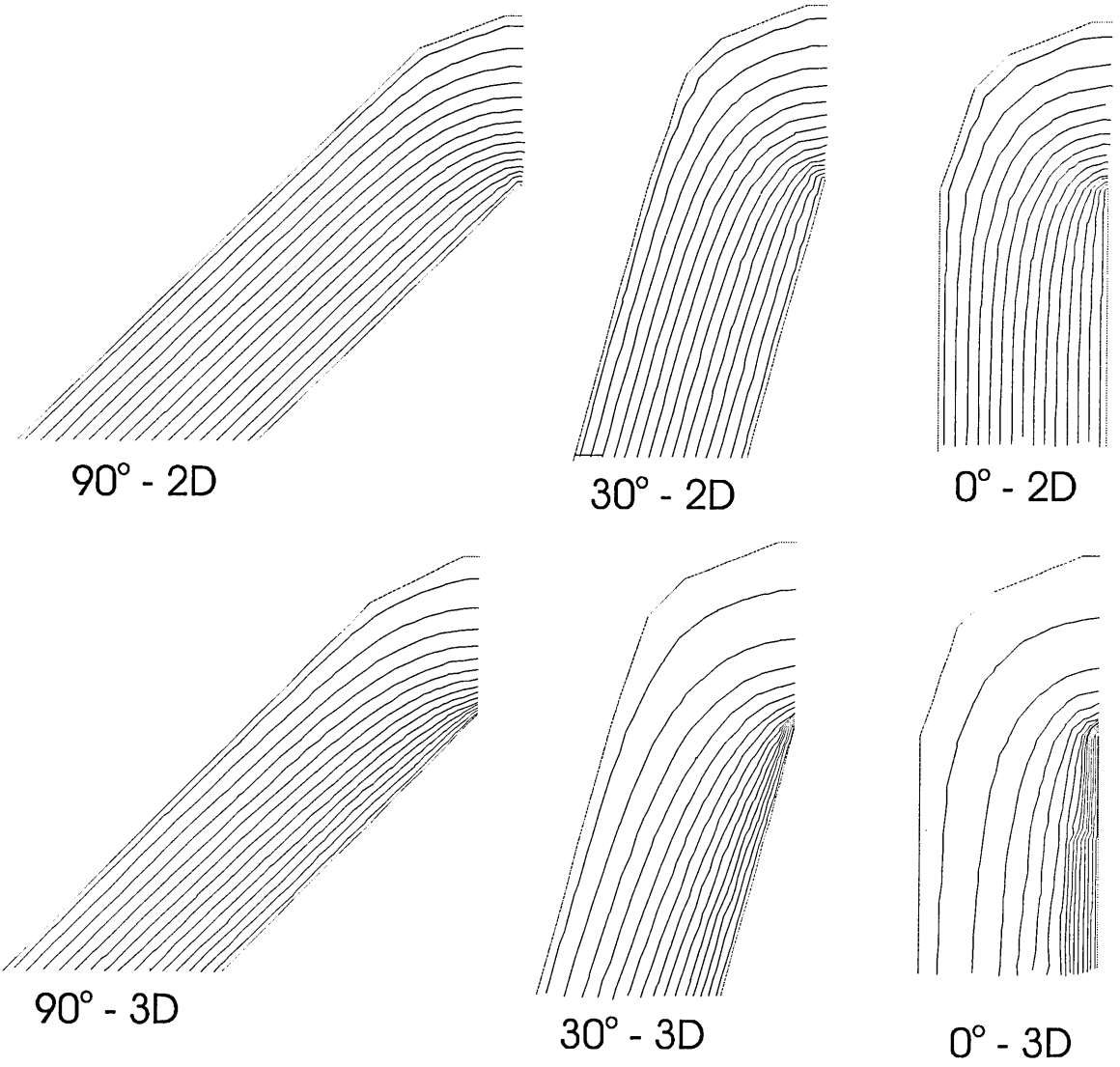

Fig.5-3: Simulated electrostatic field lines in the vicinity of sharp edges with angles 90°, 30° and 0°. Results from QUICKFIELD simulations done for two-dimensional and three-dimensional edge geometry are compared in each case.

b.) 3D simulation vs. the corners

Using our simplified model we could calculate the characteristics of the plasma sheath even in 3D which allowed us to understand the situation at sharp corners. Figure 5-3 compares the potential distribution around a 2D edge and the cross-sections of the potential distribution around a 3D cone for two geometries - 30° and 90°. The field lines are visibly even more distorted in the vicinity of the 3D edges. The difference is shown in Fig.5-4 which shows the potential profile across the plasma sheath right on top of the edges (the gradient of the potential corresponds to the strength of the electric field). The characteristic parameters of the plasma sheaths, measured in the same way as before, are summarised in Table V.

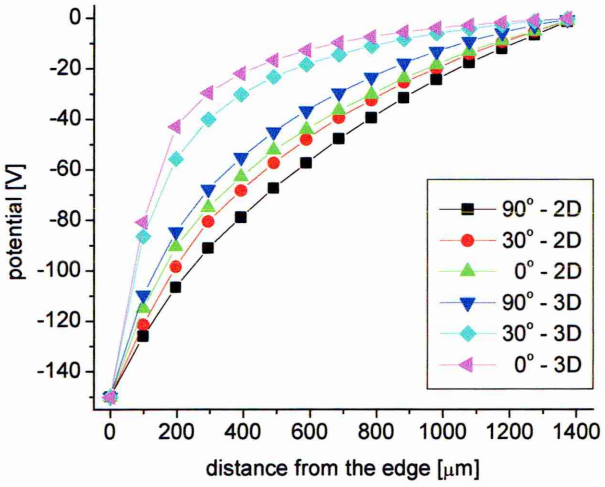

Fig.5-4: Potential profiles corresponding to the simulated electrostatic field distributions shown in Fig.5-3.

	Spatial extent x_s/y_p	**Sheath contraction** r_t/y_p	**Max. ion flux density** n_{edge}/n_{flat}
3D 30°	5.5	0.25	11.2
3D 90°	2.3	0.50	6.6

Table V: The shape characteristics of the simulated plasma sheath around 3D wedges, and the estimate of the maximum ion flux density in the edge region.

The plasma sheath is ~2-3 times more contracted towards the edge in 3D than in 2D. The sheath width at the edge for 30° cone is only ~0.25 × 0.90 = 0.22 mm at -75V and ~0.25 × 1.50 = 0.37 mm at -150V. The spatial extent of the disturbed region is ~4-8 times higher compared to the 2D case. For 30° cone, the simulated spatial extent of the effect is ~5.5 × 0.90 = 5.0 mm at -75V and ~5.5 × 1.5 = 8.2 mm at -150V, while for 90° cone, the changes should be felt up to ~2.3 × 0.90 = 2.1 mm away from the edge at -75V and up to ~2.3 × 1.50 = 3.5 mm at -150V.

The corner of a 30° wedge is in between the 30° and 90° cone geometries - it looks like a 30° cone if we look in the direction along the edge and like a 90° cone from the perpendicular direction. The simulation thus predict that the length of the edge-affected region in the corner of a 30° wedge coated at -150V should be in between 3.5 and 8.2. The experimentally measured value is ~3.2 mm (Fig.4-15).

The simulations also show that in 3D the ion flux density in the edge region is increased by ~3-4 times compared to the 2D case. This explains the enhancement of the edge-related effects experimentally observed at the corners. It also explains why the same type of morphology as in the middle of the wedges was observed at lower ion energies in the corners (section 4.3).

5.2. Ion trajectories across the plasma sheath

5.2.1. Modelling of the ion flux and the angle of incidence distributions (in 2D)

The spatial distribution of the electric field in the plasma sheath around wedge-shaped samples simulated in section 5.1. can be used to calculate the ion trajectories across the sheath. We have developed a Monte Carlo simulation program which calculates the motion of ions under a given electric field inside a 2D region (the plasma sheath). The schema of the simulations is shown in Fig.5-5. The ions start at a random place along the plasma boundary* with an initial energy of 0.5 eV and a random initial direction. Their trajectories inside the sheath are then calculated from the following set of equations:

* Due to our simplifications, we have selected the equipotential line situtaed at $2/3\varphi_0$ as starting boundary.

$$a_x = \frac{q}{m} \times E_x \qquad a_y = \frac{q}{m} \times E_y$$
$$v_{x(i+1)} = v_{xi} + a_x \times dt \qquad v_{y(i+1)} = v_{yi} + a_y \times dt$$
$$x_{(i+1)} = x_i + v_{x(i+1)} \times dt \qquad y_{(i+1)} = y_i + v_{y(i+1)} \times dt \quad , \qquad \text{(Eq.5-9)}$$

where the acceleration a (components a_x, a_y) is calculated from the intensity of the electric field E (E_x, E_y), this is then used to calculate the velocity v (v_x, v_y) and finally the spatial coordinates (x and y). The time step dt can be selected at the beginning of the simulations - the smaller it is, the more accurate the trajectories will be, but on the other hand it prolongs the simulation (as more calculations are needed). The electric field components (E_x, E_y) were taken from the Quickfield simulations (section 5.1.). The ion density distribution can be determined from the number of ions hitting a selected unit length (dl) on the sample surface. The angle of incidence distribution along the surface can be calculated from the velocity components at the impact.

The results from simulations done for a sharp wedge with angle 0° (knife edge) are presented in Fig.5-6, together with the results by Watterson. The comparison shows again good agreement with the more accurate self-consistent model. Identical results were also obtained using electron and ion optics simulation program SIMION (http://www.sisweb.com/simion/installs.htm), which calculates both the electric field and ion trajectories using fourth order Runge-Kutta numerical integration method.

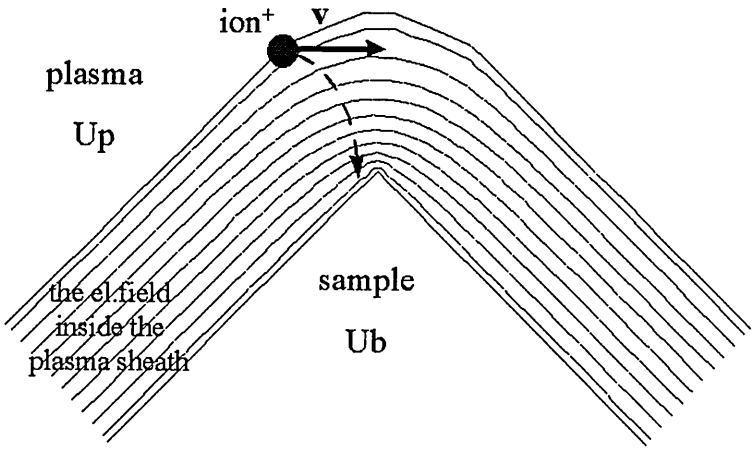

Fig.5-5: Schematic drawing showing the set-up of the simulations of the ion trajectories across the plasma sheath. Positively biased ions (with an initial velocity v) attracted from the plasma towards the negatively biased sample are moving across the electric field inside the plasma sheath. The x- and y-directions are defined in Fig.5-1.

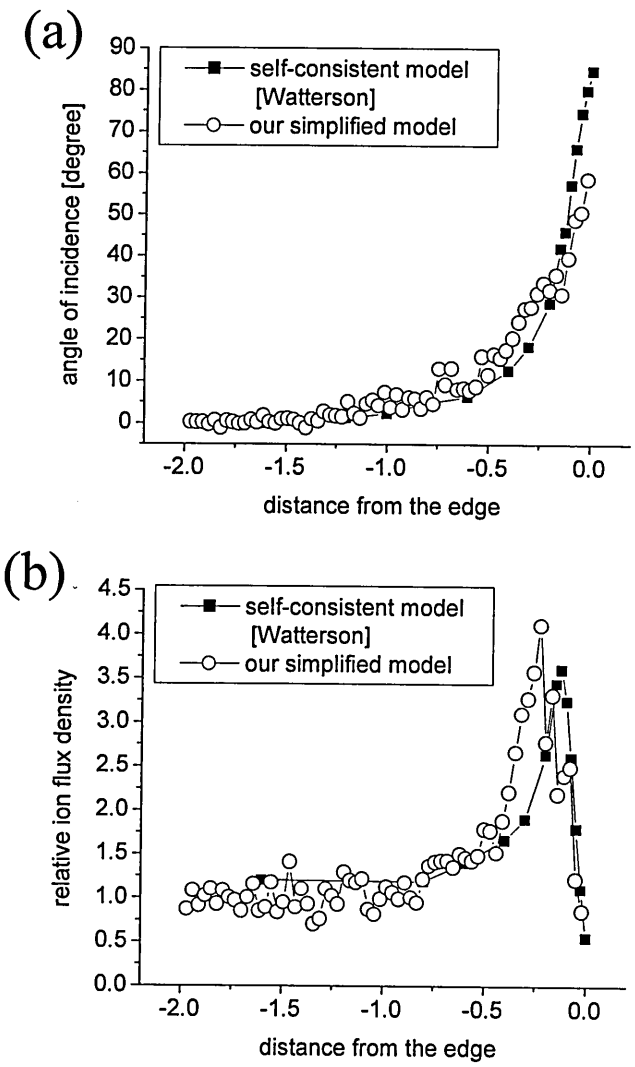

Fig.5-6: Angle of incidence and ion flux density distributions as a function of the distance from the edge, simulated for a sharp edge with angle 0° (knife edge). Our results are compared with those calculated by Watterson (1989). The variables are in the dimensionless form defined in the text.

5.2.2. Quantification of the increase in the sputtering rate

The simulated ion flux and angle of incidence distributions can be used to calculate a crucial parameter - the magnitude of the sputtering rate of the ions along the wedges. The sputtering rate, defined as the number of atoms removed from unit area on the sample, per unit time, can be written as:

$$S = n \times Y, \qquad \text{(Eq.5-10)}$$

where n is the ion flux density at the sample - number of ions hitting unit area of the surface per unit time, and Y is the sputtering yield of the ions - defined as the number of removed atoms per number of incident ions. The sputtering rate is a very important parameter from the practical point of view as it influences directly the thickness of the coating (the resputtering of the atoms from the growing coating reduces its thickness) and it gives us a measure of the ion-coating interaction.

a.) TRIM simulations

The sputtering yield of the ions at any point along the wedge is a function of the angle of incidence of the ions (Andersen, 1981). The sputtering rate increases with increasing the angle of incidence because the density of energy deposition near the surface of the sample increases - allowing more atoms to escape. When the angle gets close to 90°, however, the ions are almost reflected from the surface and their efficiency decreases. We have used TRIM simulation program (available at http://www.srim.org) in order to determine the change in the sputtering yield with the angle of incidence of the ions in our conditions. The results from simulations done for TiAlN and VN layers bombarded by Ar^+ ions with energy 150eV are shown in Fig.5-7. The sputtering yield of all the elements reaches a maximum at angle of incidence ~70° (the angle being slightly different for each element). The sputtering yield at the maximum is ~2.2-3.5 times higher compared to the perpendicular angle of incidence ($\beta = 0$). In the case of our wedge-shaped samples, the angle of incidence is changing from perpendicular to the surface far from the edge to along the wedge plane of symmetry. The maximum angle of incidence of the ions, occurring close to the edge, will thus be equal to $90°-\alpha/2$ (see Fig.5-7b), which is ~45° for the 90° wedge, ~67° for 45° wedge and ~75° for the sharpest 30° wedge. In relation with this the increase in the sputtering rate near the edge will be different for each geometry (as indicated in Fig.5-7a by the arrows).

If we now multiply the sputtering yield and the ion flux at any point along the wedge - combining the simulated results shown in Fig.5-6b and Fig.5-7a, we can finally calculate the spatial distribution of the sputtering rate of the ions (Eq.5-10). We have done the calculation for two cases: 30° and 90° wedge, both coated at -150V. To get a more accurate result we have used the angle of incidence and ion flux density

distributions simulated by Watterson. Our simulations would however give a similar results - as shown in Fig.5-6. The results simulated for the knife edge (α = 0°) were used as an approximation of the 30° wedge case.

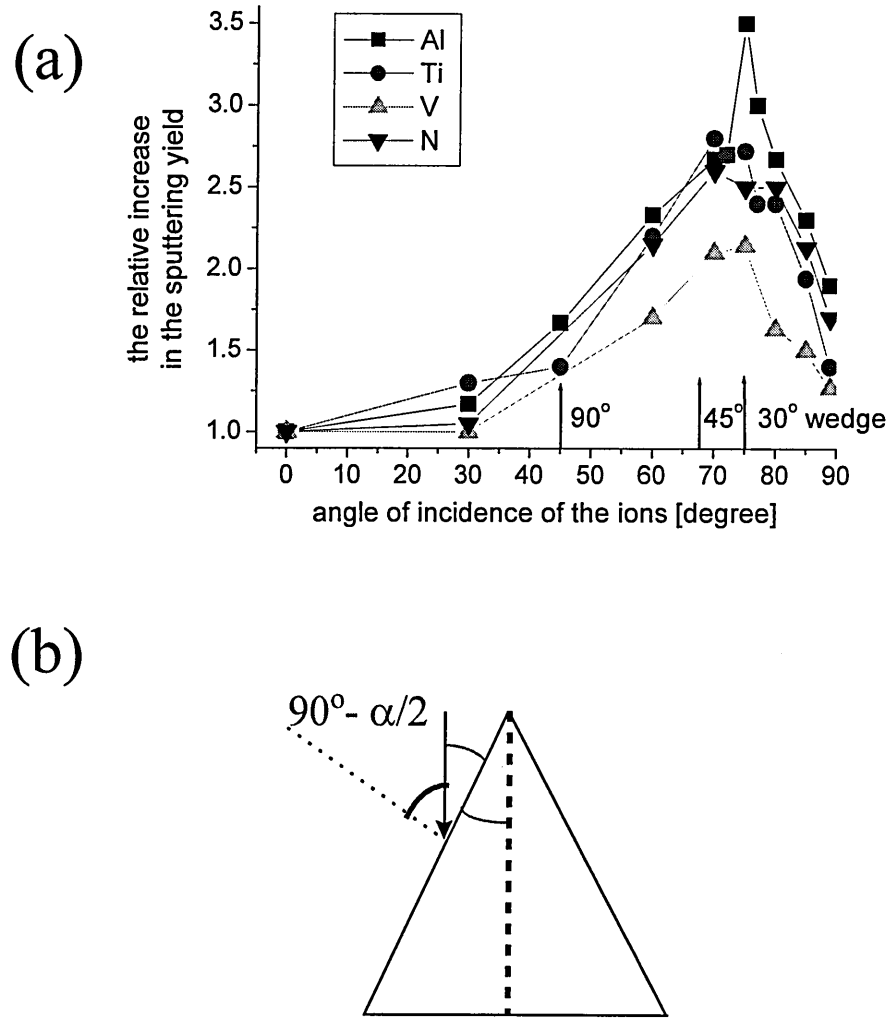

Fig.5-7: (a) The component sputtering yield of different elements as a function of the angle of incidence of the ions, simulated using the TRIM code. The bombardment of $Ti_{0.5}Al_{0.5}N$ and $V_{0.5}N_{0.5}$ by Ar^+ ions with energy 150eV was simulated. The arrows on the x-axes show the value of the angle of incidence near the edge for wedges with different geometries. (b) Schematic drawing showing the relationship between the angle of incidence of the ions near the edge (where they arrive parallel to the wedge plane of symmetry) and the wedge angle α.

b.) Sputtering rate increase in the edge region for the 30° wedge coated at -150V

The upper part of Fig.5-8 shows the simulated angle of incidence and ion flux density distribution in the case of 30° wedge coated at -150V. The x-axis, originally dimensionless, was scaled using the value of the planar sheath width at -150V: $y_p = 1.5$ mm. The micrograph underneath shows the side-view of the wedge, at the same scale as the x-axis of the graph. The edge-affected region starts at around ~1.2 mm from the edge, where the ion flux density and the angle of incidence of the ions start to increase. The effect induces changes in the coating properties - such as thickness, composition and thus stress - which manifest itself by the appearance of partial delaminations (further away from the edge, the coating is homogeneous). The increase of the two parameters is however non-uniform. There is a distinctive region close to the edge, starting at ~300 μm, in which the change is almost exponential and where complete resputtering of the coating occurs. The sputtering rate of the ions, calculated by combining the ion flux density with the sputtering yield of the ions (calculated from the angle of incidence) is plotted below. The function shown corresponds to the sputtering rate at which the ions resputter Al. The figure reveals two significant results:

- The sputtering rate of Al is up to ~10-times higher than on flat samples - which is difference of one order of magnitude.
- The maximum of the sputtering rate occurs at some distance away from the edge - ~120 μm in this particular case.

The shape of the function would be similar for Ti or V, but with lower increase. The significant increase in the sputtering rate of the ions explains the complete resputtering of the coating during the deposition and their impact on the topography of the surface. Side views of the resputtered region, together with the corresponding compositional maps, are presented in Fig.5-9a. The figure shows erosion of the substrate material, which can be clearly visible between 100 and 200 μm from the edge. The maximum of the ion sputtering is at ~150 μm from the edge, which is in good agreement with the simulated value. After reaching the maximum, the sputtering rate goes down and the surface less than 100 μm away from the edge is much less disturbed. A closer look reveals that the eroded structures are small cone-like features (which will be discussed in more details in section 5.3.). The compositional maps show that there are some

remains of the coating material near these features because they were shadowed by the protrusions.

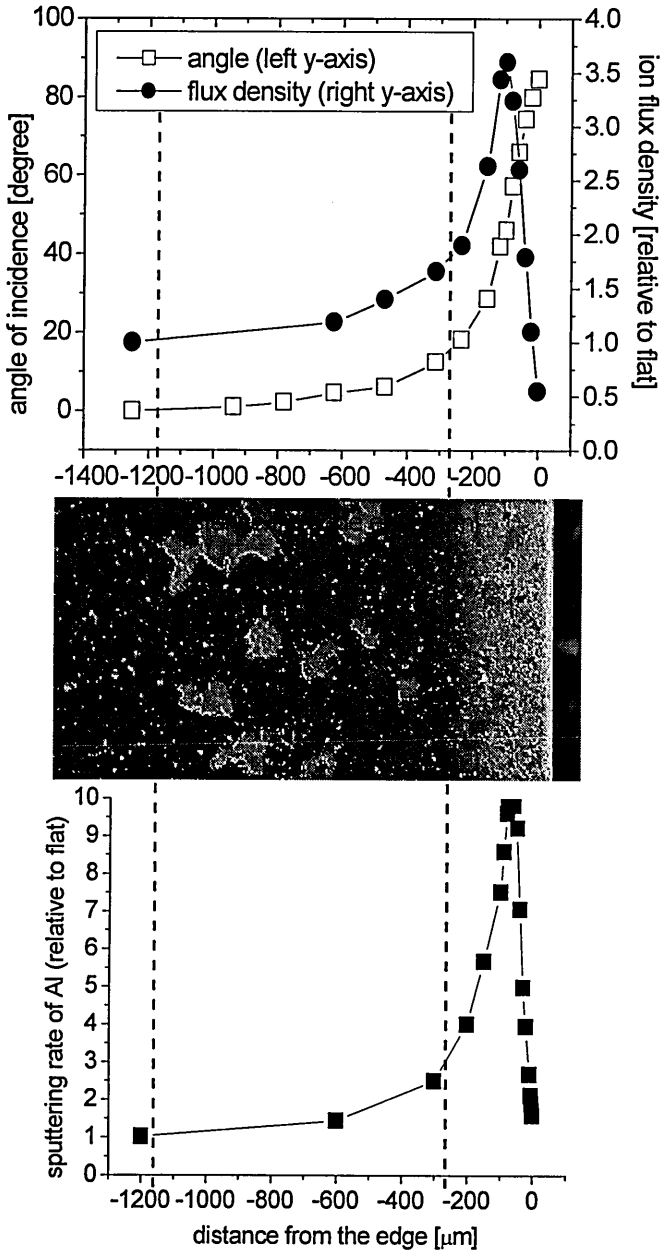

Fig.5-8: The upper part: The angle of incidence and ion flux density distributions shown in Fig.5-6 - applied to the case of the 30° wedge coated at -150V. The middle part: Side-view of the wedge at the same scale as the x-axis on the graph above. The edge line is vertical. The lower part: The calculated resputtering rate distribution on the same wedge. The dashed vertical lines show the borders of the distinctive regions and connect the three parts of the figure.

Fig.5-9b shows side view of the 45° wedge coated at -150V. For this wedge, slightly less sharper than the 30° case, the increase in the sputtering rate would be slightly lower and would occur closer to the edge - which is in agreement with the surface topography. There seems to be also a difference between the topography at different places which correspond to different crystal grains in the substrate material. This effect will be described in section 'e' below. The effect is not clearly visible on the 30° wedge because there the substrate is much more disturbed by the ions.

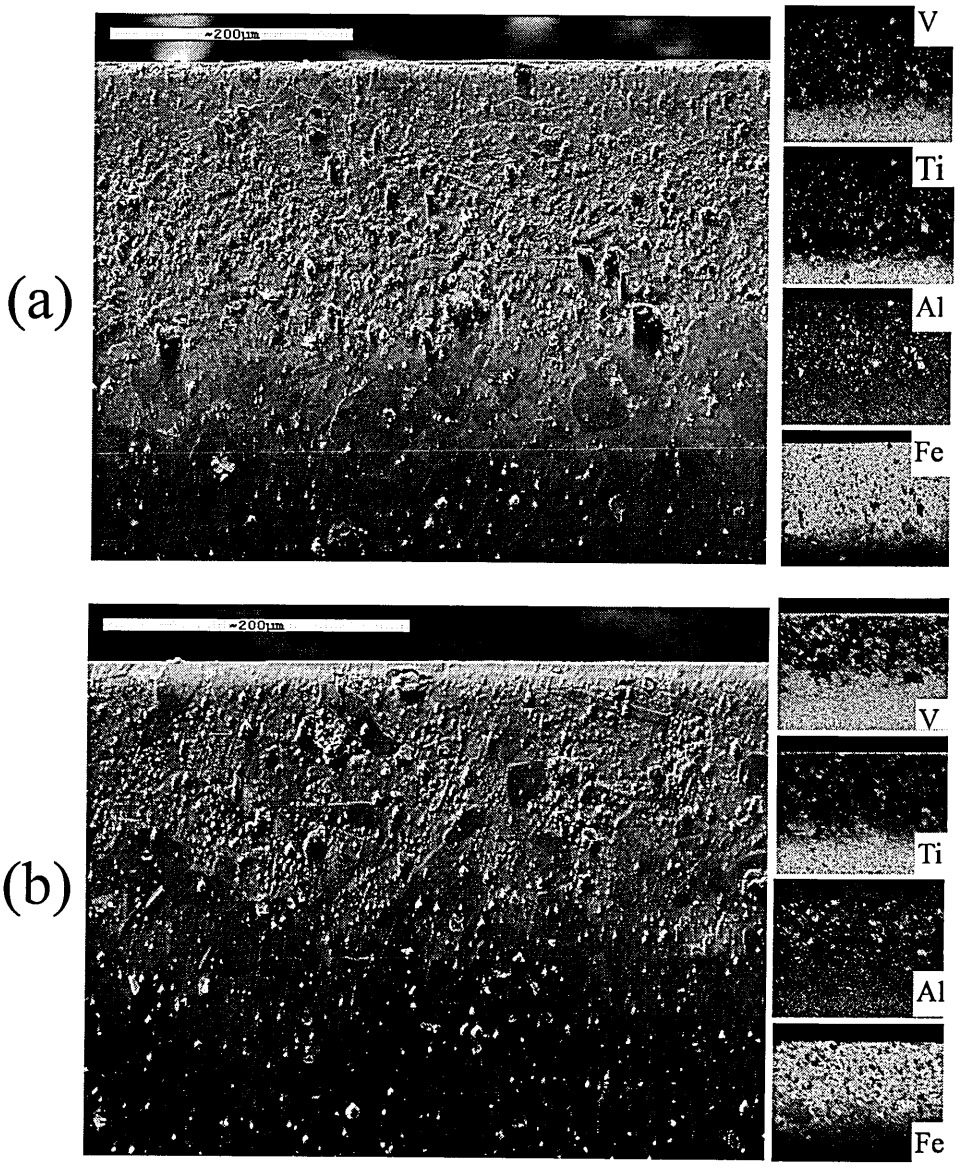

Fig.5-9: Side-view of the completely resputtered region on (a) 30° wedge coated at -150V, (b) 45° wedge coated at -150V. On the left side the corresponding compositional maps are shown.

c.) Sputtering rate increase in the edge region for the 90° wedge coated at -150V

In the edge region of 90° wedge, the maximum ion flux density is ~2-times higher (Table III) and the maximum sputtering yield is ~1.5-times higher (TRIM value for the angle of incidence 45° - Fig.5-7a). The sputtering rate is thus increased by up to ~3-times the value far from the edge. The distribution would have similar shape as the one in Fig.5-8, but with much lower maximum, situated closer to the edge. The sputtering rate increase in this case is not sufficient to create complete resputtering as in the case of the 30° and 45° wedges, however the increased sputtering manifest itself by reducing significantly the thickness of the coating, which can be seen in Fig.4-6 in Chapter 4.

d.) The increase in the sputtering rate at corners (3D case)

The increased ion flux at the corners discussed in section 5.1.2.b leads to increased sputtering rate of the ions. In the case of 90° wedge coated at -150V, the ion flux density at the corner is increased by up to ~6.6 times (Table IV). The sputtering yield will be ~1.5-times higher (the value from TRIM for 90°), which means that the increase in the sputtering rate will be ~10 times compared to flat samples. The value is similar to the magnitude of the sputtering rate increase in the middle of 30° wedge coated at the same bias (section 'a' above). This is in agreement with the experimental observations which show the similarity in the topography between the middle of the 30° wedge and corner of the 90° - see Fig.4-13 (Chapter 4).

The highest increase in the sputtering rate will occur in the corner region of 30° wedge coated at -150V. The simulated increase in the sputtering rate is ~11.2 times (Table V), while the increase in the sputtering yield is ~3.5 (Fig.5-7a). This means that the sputtering rate in this region can be up to ~40 times higher than on flat parts. This dramatic increase not only completely resputters the coating but it also causes significant erosion of the substrate material, much more severe than in the middle of the wedge, and creates complex ion-induced topography which will be discussed in details in section 5.3.

e.) The effect of the edge radius

The simulations presented so far were done for infinitely sharp edges ($r \rightarrow 0$). In reality however the edges have a certain radius of curvature, the magnitude of which will necessarily affect the electric field in the vicinity of the edge, and thus the edge-effects we are studying. The electric field distributions simulated using the Quickfield program (using the same set-up as described above) for a range of radii of curvatures can be seen in Fig.5-10. Two different wedge angles were chosen - 30° and 90°, while the radius was varied from r = 0 (infinitely sharp edge) to r = 500 μm.

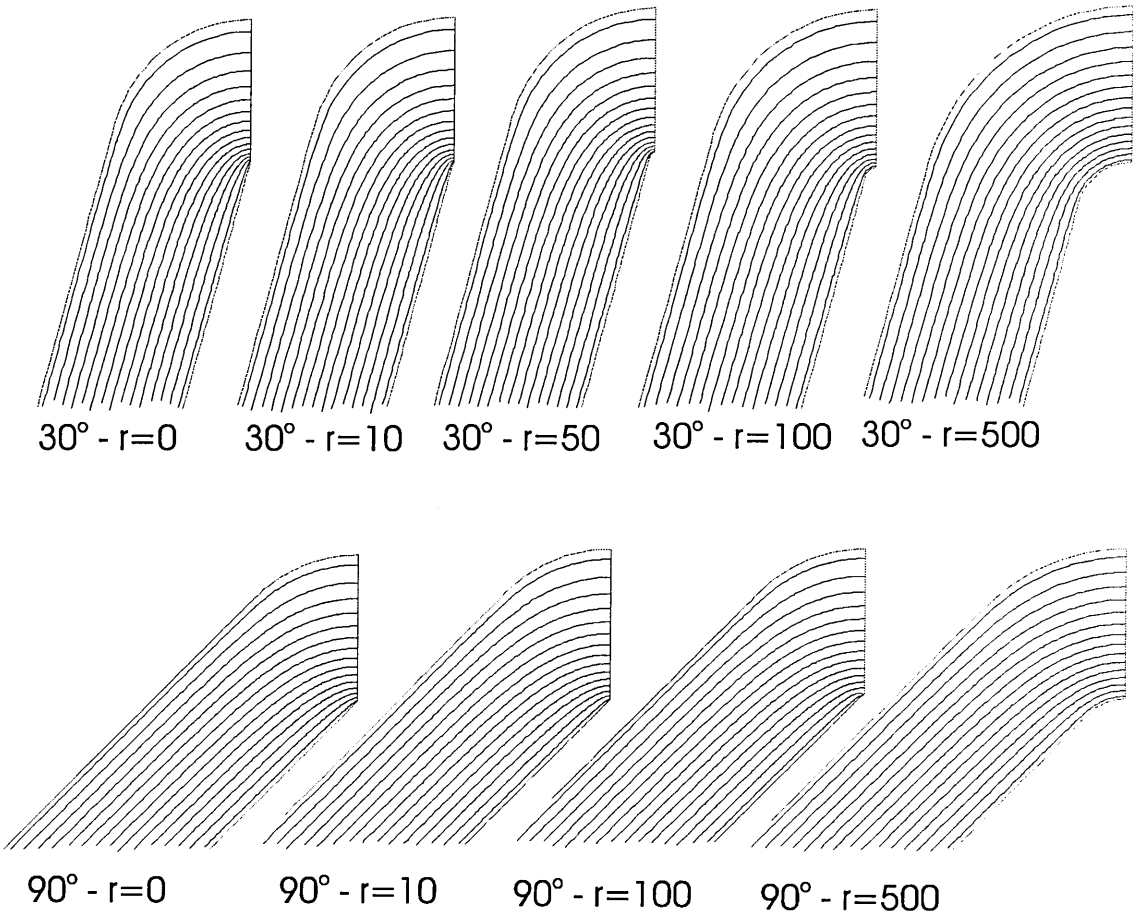

Fig.5-10: Simulated electrostatic field lines across the plasma sheath around two-dimensional edges with angles 30° and 90° (QUICKFIELD). For each angle, the radius of curvature of the edge was progressively increased from 0 (infinitely sharp) to 500 μm. (Only half of the cross-sections is shown, the other half would be mirror-image of the first one.)

With increasing the radius of curvature, the potential lines close to the edge become more and more uniform - the electric field is decreasing towards the value above a flat surface. The variation of the potential across the sheath right on top of the edge, for all the different geometries, is presented in Fig.5-11. Because of our simplification of a constant plasma sheath boundary, the profiles have the same length - in reality with increasing the electric field near the edge, the plasma is drawn nearer to the edge (sheath contraction) and the corresponding variations are happening across a smaller distance. The figures nevertheless reveal that the potential profiles for wedges with radii of curvature much smaller than the dimensions of the sheath width - 10 and 50 μm (as well as 100 μm) - are very similar to the case where the radius was assumed to be infinitely sharp. This explains the agreement between the edge effect characteristics measured on the real wedges, with radius ~2 μm, and the values simulated for an infinitely sharp edge.

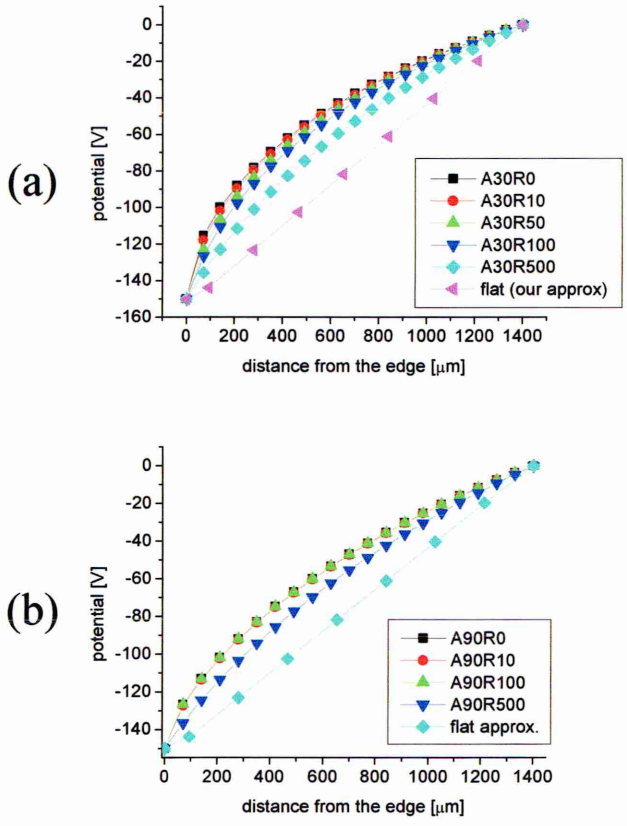

Fig.5-11: Potential profiles corresponding to the simulated electrostatic field distributions shown in Fig.5-10. Potential profile above a flat surface in vacuum (similar to the profile in the plasma sheath) is also shown.

Additionally, the trajectories of ions in the electric field above a 0° wedge (knife edge) with radii 2, 5 and 10 μm were simulated using the SIMION program (in the same way as described in section 5.2.1). The ion flux distributions are shown in Fig.5-12. The profiles are similar, but the magnitude of the maximum increase in the ion flux, happening at ~150 μm from the edge, is slightly decreasing with increasing the radius. The value of the ion flux hitting the region right on top of the edge are however similar for all three radii.

The properties of coatings grown on wedges with the different radii of curvatures, small compared to the sheath dimensions, would however be different because of another effect - the change in the relative angle between the arriving ions and the growing surface. With increasing the radius of the growing surface, there is an increasingly large region right on top of the edge in which the surface will be perpendicular to the ions, arriving along the wedge axes of symmetry. This is clearly visible in Fig.5-13 which shows simulated ion trajectories near 0° edge with radius 10 μm. In this region the sputtering yield will thus be relatively lower compared to neighbouring regions where the entry is oblique. Taking into account that the EDX probe, at any position, is detecting the average composition from a region with dimensions ~1 by 1 μm, this explains the compositional profiles measured across the coating, shown in Fig.4-11 (Chapter 4).

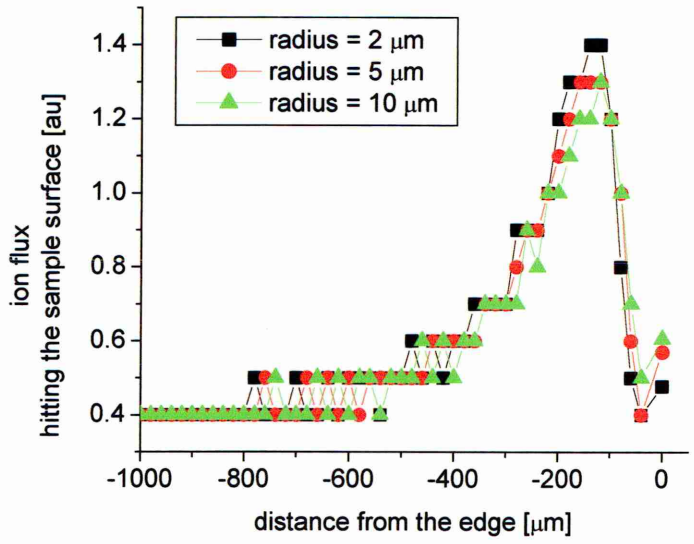

Fig.5-12: Ion flux density distribution as a function of the distance from the edge, simulated for an edge with angle 0° and three different radii of curvature (SIMION).

The value of the ion flux on top of the edge simulated for zero radius is lower than the value far from the edge (Fig.5-8). Simulation for edges with radii (Fig.5-12) - which are closer to reality, show however that the value is actually similar (or slightly higher) than the value corresponding to flat surface. This corresponds well with the measured values which for increasing radii change towards the 'flat value'. Because the ion flux in these regions is similar to that above a flat surface and the angle of incidence is the same - perpendicular (unless the wedge angle is very small - such as the 30° case), the sputtering rate of the ions is similar and thus also the ratio of the elements inside the coating.

In the case of radii large enough to be comparable with the sheath dimensions, which is the case of the 500 μm radius, the electric field near the edge is less disturbed and the potential profiles are closer to the situation above a flat surface (Fig.5-10). The ion flux being similar throughout the coating, as well as the perpendicular incidence - the edge is 'rounded' already at the substrate-coating interface, the compositional values across the coating are almost constant, and are close to the values corresponding to the flat case - which is in agreement with Fig.4-12 (60° wedge with radius ~250 μm).

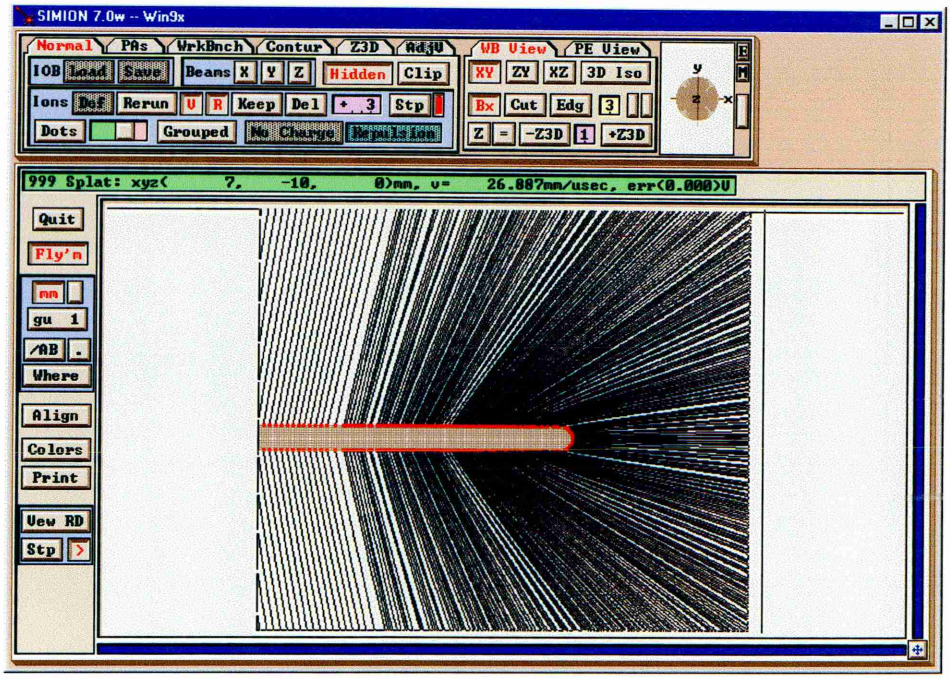

Fig.5-13: Simulated ion trajectories near 0° edge with radius of curvature 10 μm - showing clearly the continuos change in the angle of incidence of the ions (SIMION).

f.) The effect of the crystallinity of the substrate

We have assumed so far that the substrate and the coating are single crystal materials. In reality, the stainless steel substrate we have used is a polycrystalline material composed from grains having different crystallographic orientations and the situation will be similar for the coating growing on top of them. The relative orientation of the atomic planes and the direction of ions affects the sputtering yield (Roosendaal, 1981), and we can thus expect that the sputtering rate will show some variations from grain to grain and that this effect will be enhanced in the edge region.

The effect can be clearly seen from Fig.5-14a which shows the region next to the edge on 30° wedge coated at -150V at high magnification. There is no coating left in this region and what we see is the topography of the steel substrate caused by the ion bombardment (during the etching phase, as well as during the UBM sputtering). There are distinctive smooth grains which are clearly separated from the rough surrounding because their crystallographic orientation decreases the sputtering yield of the ions.

The effect is also visible when there is a thin coating on top of the substrate. Fig.5-14b shows the edge region on 90° wedge coated at -150V, together with the compositional maps. Here the different sputtering yields manifest itself by the differences in the thickness of the coating on different areas. Most of the region is bright on the Fe map - the coating on top is thinner than 1 μm and the X-ray excitation volume can reach the substrate. But we can also see distinctive grains with orientation lowering the sputtering yield of the ions and therefore covered with coating thicker than 1 μm. They are dark on the substrate map, while they are bright on the Ti map even though Ti, being more easily resputtered than V, is almost completely resputtered from all other areas. Al, with the lowest sputtering yield, is missing completely from the edge region. The same can be seen in Fig.5-9b. The grains are clearly visible on the 45° wedge coated at -150V. There is a very thin coating on the smooth dark coloured grains containing V and some Ti, the Al is completely resputtered. On the surrounding areas there is no coating left and the substrate is subjected to the ion bombardment which creates the rough surface.

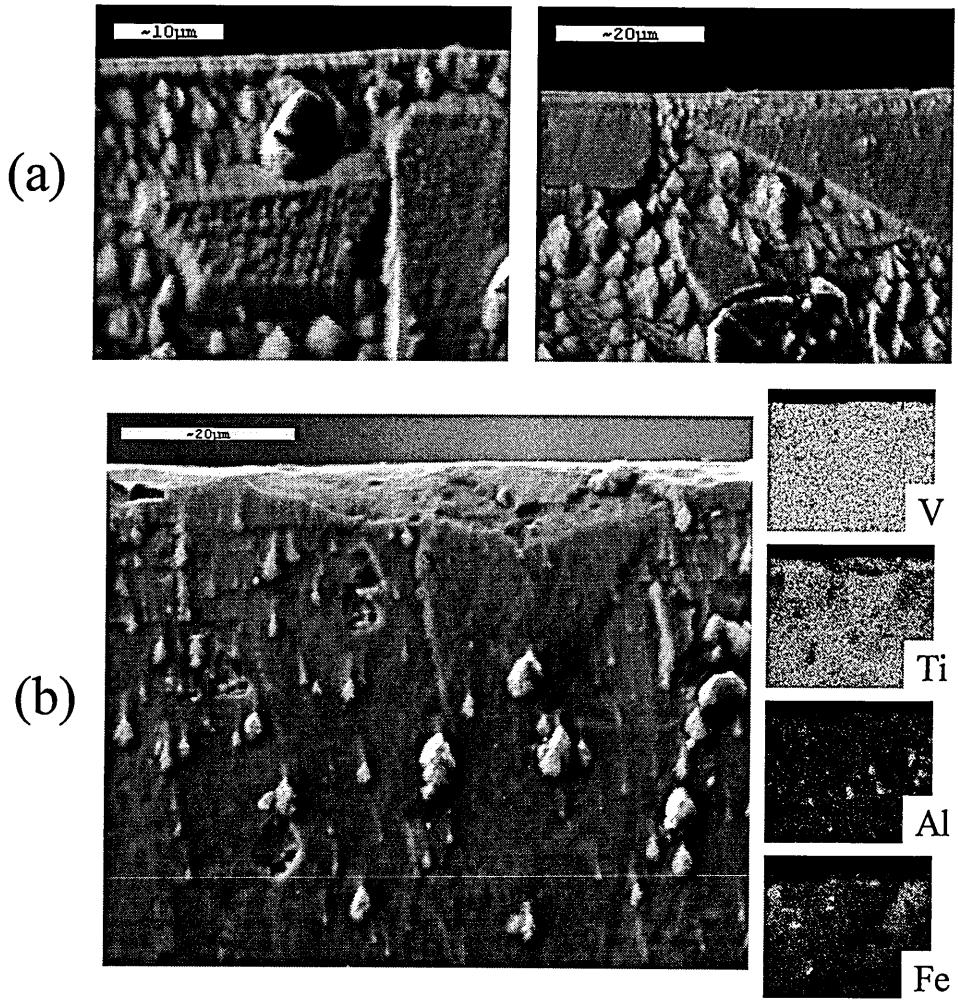

Fig.5-14: Topography of the edge region (in the middle of the wedges) in the case of: (a) 30° wedge coated at -150V, (b) 90° wedge coated at -150V, accompanied by compositional maps.

5.3. Ion-induced topography

At the highest substrate bias -150V the sputtering yield and thus the sputtering rate of the ions at edges and corners is high enough to compete with the growth of the coating. For all the wedges examined - 30°, 45° and 90° - close view of the edge and corner regions reveals partially or completely resputtered coating (Fig.4-13, Fig.4-14 in Chapter 4). In the places where the coating is resputtered - which are the places where the ion bombardment is the most intense - the ions are interacting with the stainless steel substrate material. In this section we will discuss the topography which is thus created and show the relationship between the characteristics of the topographical

features and the simulated characteristics of the ion bombardment (such as magnitude, spatial distribution, angle of incidence of the ions).

The most spectacular effects of the ion bombardment can be seen in the corner region of 30° wedge (coated at -150V) where the sputtering rate is increased by up to 40-times when compared to the usual value on flat samples (section 5.2.2.d). The boundary at which the complete resputtering in the corner starts is shown in Fig.5-15. As we approach the corner, the thickness of the coating (dark coloured smooth regions) is rapidly decreasing. Because the coating is so thin, we can see the contours of the different substrate grains. A small distance closer to the edge the coating and the grain contours suddenly disappear. The sudden increase in the sputtering rate of the ions starts to shape the substrate, creating complex topographical features such as ripples and - closer to the corner - cones. The change in the morphology of the substrate as a function of the distance from the corner for the 30° wedge can be seen in Fig.5-16. At the boundary of the resputtered region - roughly 500 μm from the corner - small ripples appear (Fig.5-16a). Their amplitude progressively increases and the substrate becomes more and more rough (Fig.5-16b). At a distance ~300 μm from the corner, the ripples change into cones (Fig.5-16c).

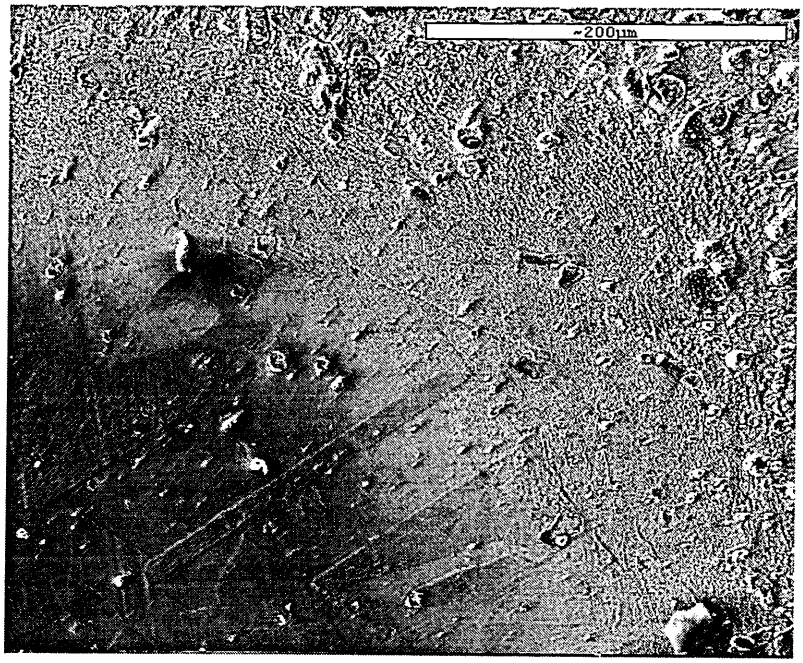

Fig.5-15: Surface topography on 30° wedge coated at -150V in a region ~500 μm from the corner.

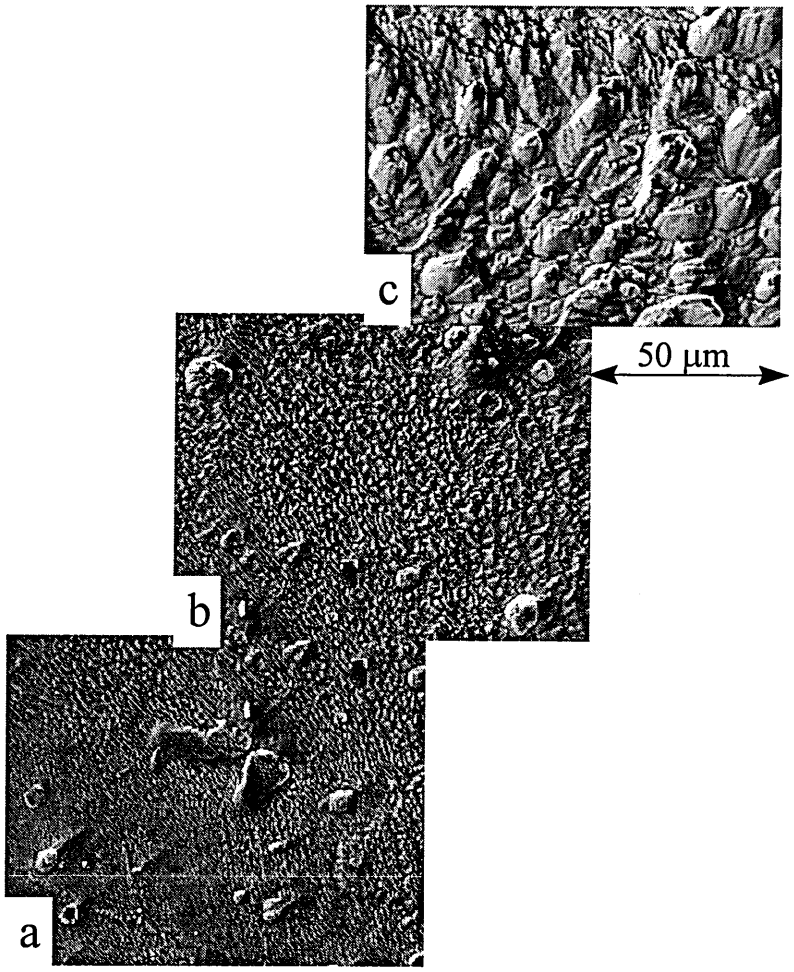

Fig.5-16: Surface topography on 30° wedge coated at -150V at a distance: a.) 400, b.) 300, c.) 200 µm from the corner.

Although ion-induced surface variations such as ripples and cones are often observed on bombarded surfaces, their formation is not yet fully understood. It has been suggested that ripples are the results of stress waves formed in the materials by uniform ion bombardment (Carter, 1977) and that they are related to bombardment at an oblique angle of incidence (Bradley, 1988). With increasing the ion bombardment, individual ridges can evolve from the ripples due to localised non-uniformities - such as surface roughness, impurities or ion-induced defects (Kester, 1993). The initial morphological features are then intensified upon subsequent bombardment due to the dependence of the sputtering yield on the angle of incidence of the ions. On a flat surface the sides of any protrusion will be bombarded at an oblique angle and will thus be sputter away faster than the surrounding area.

In the case of our wedge-shaped sample, the gradual increase in the ion bombardment as a function of the distance from the corner means that surface topographical features at different stages of development, such as ripples and cones, can be observed in close proximity to each other. The sudden change from the ripples to the cones we have observed in Fig.5-15 can be associated with the steep increase in the ion flux which happens at a specific distance from the corner (shown in Fig.5-8 for the 2D case).

The effect of the magnitude of the ion bombardment on the surface topography can be seen in Fig.5-17, where the corner area of the 30° wedge is compared with the edge region in the middle of the wedge. The comparison clearly shows the significant increase in the ion-induced substrate erosion at the corners - corresponding to 4-times increase in the sputtering rate (the rate in the middle edge region is ~10-times the value on flat samples (section 5.2.2.b), while the value at the corner is ~40-times (section 5.2.2.d)). In the middle of the wedge (Fig.5-17b) small cone-like features can be observed on some of the grains. In the corner region (Fig.5-17a) the roughness of the surface is highly increased and the cones are much more pronounced. Due to the intensive erosion, individual grains cannot be distinguished here, although some differences in the cones concentration between different places can be seen.

The change in the magnitude of the ion bombardment as a function of the distance from the edge/corner induces further effects. In section 5.2.2.b we have seen that there is a region, at a specific distance from the edge, where the sputtering rate steeply increases and that after reaching the maximum the rate goes down closer to the edge. The corresponding topography in the middle of the wedges was shown in Fig.5-9. The effect is much more spectacular at the corners - as shown in Fig.5-18 for the 30° as well as 45° wedge. As we are approaching the corner, we can see increase in the substrate erosion leading to a maximum and then decreasing - which creates the smooth region lining the corners. The width of this region is ~20 μm for the 45° wedge and ~50 μm for the 30° wedge where it is much more pronounced. When comparing the 30° and 45° wedge, the combined effect of higher ion flux and a bigger change in the angle of incidence (from 0° to ~75°, compared with 67.5°) explains the more dramatic topographical variations on the 30° wedge. This is also why the corner of 90° wedge, shown in Fig.4-17 in Chapter 4, is much less disturbed.

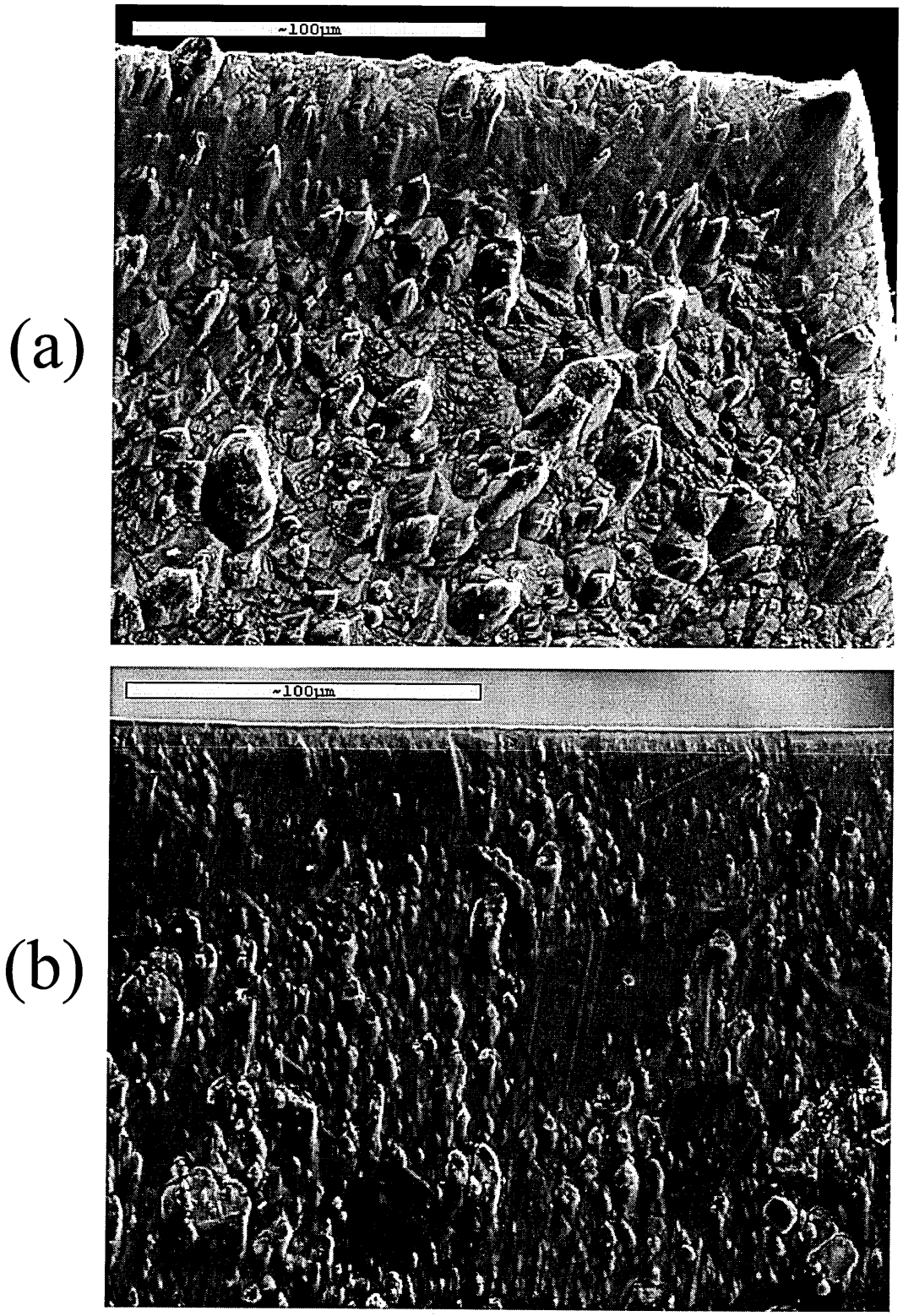

Fig.5-17: Surface topography near the edge of 30° wedge coated at -150V: (a) at the corner, (b) in the middle of the wedge.

(a)

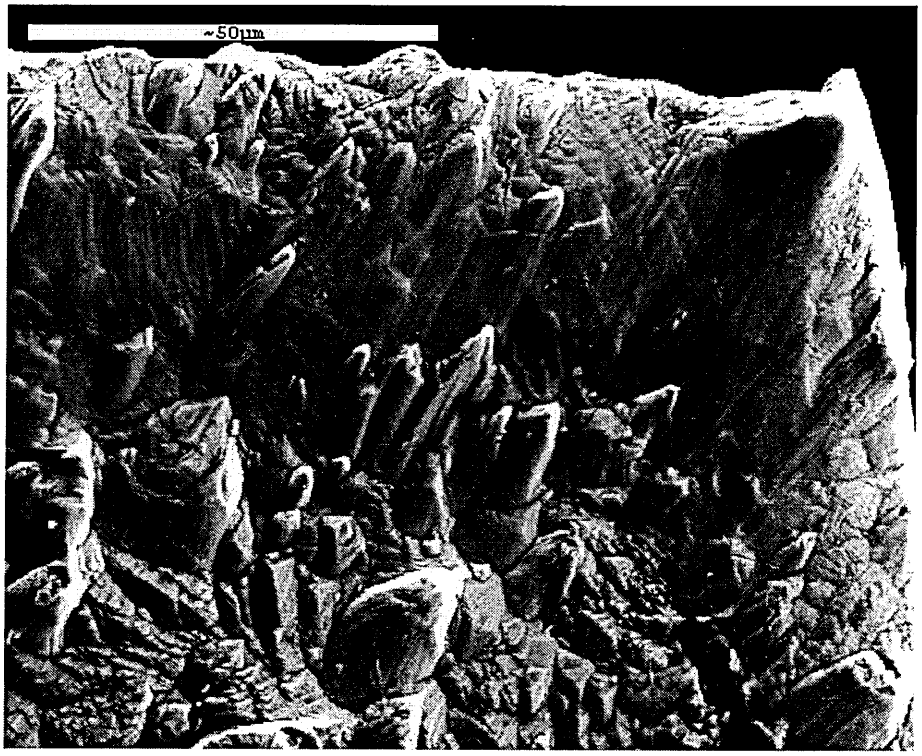

(b)

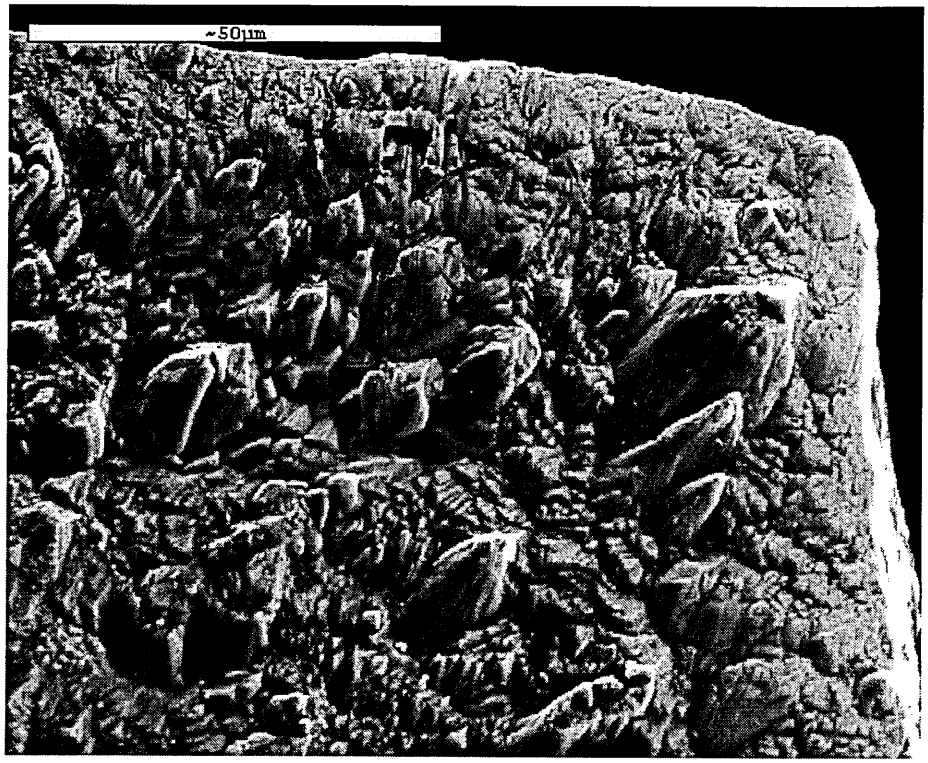

Fig.5-18: High magnification view of the corner region on (a) 30° wedge coated at -150V, (b) 45° wedge coated at -150V.

The way in which the cones are oriented relative to the edges is directly related to the spatial distribution of the ions - the ions and thus the cones are directed towards the edge in Fig.5-17b and towards the corner in Fig.5-17a. The orientation of the cones relative to the surface normal is, on the other hand, given by the angle of incidence of the ions. According to the theory of cone formation in (Hauffe, 1991) the axes of the cone structures are parallel with the direction of the bombarding ions. The cones therefore follow the gradual change in the angle of incidence of the ions - from perpendicular to the surface far from the edge to almost parallel to the surface close to the edge/corner.

Some localised remains of the coating material can be found in places which were shadowed from the ion flux or where the ion bombardment was less severe. In Fig.5-18 the small black patches which can be seen on both wedges correspond to coating material which remained in places shadowed by the surrounding features and/or was redeposited there from other regions during the bombardment. The coating material was also observed on top of some of the cones, as these places were sputtered much less than the sides of the cones. The effect could however be observed only in regions close to the boundary at which the increased resputtering started. Closer to the edge, the cones were much sharper and all the material was resputtered, due to the much higher overall sputtering rate.

Chapter 6: Internal structure of coatings growing on sharp edges at low substrate biases

The simulations of ion trajectories around wedges done in section 5.2.2.e have shown that there is a distinctive region right on top of the edge in which the angle of incidence of the ions suddenly changes from very steep to perpendicular to the surface - Fig.6-1 (taken from Fig.5-13). Furthermore the coating is strongly curved in this region. The influence of these effects on the internal structure of the coatings is examined in this chapter.

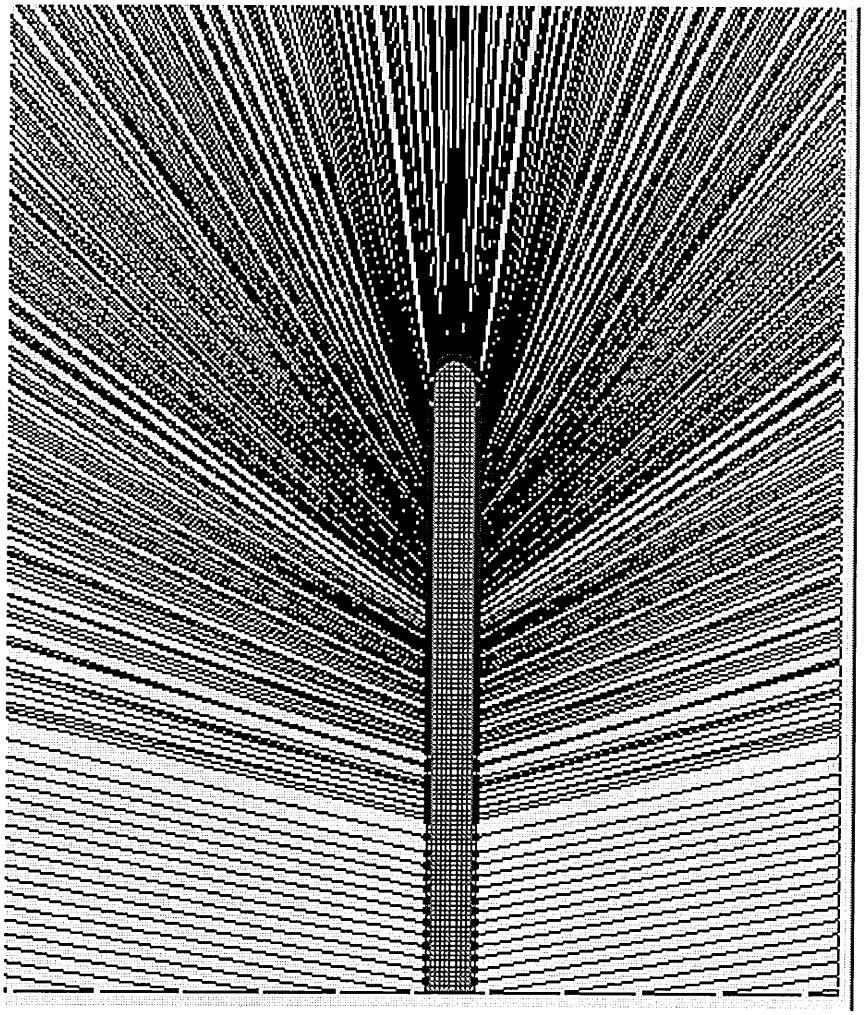

Fig.6-1: Simulated ion trajectories in the vicinity of an edge with angle 0° and radius of curvature 10 μm.

TEM cross-sections, prepared by two different methods, are presented: 30° wedge coated with TiAlN/VN - prepared by FIB, and 60° wedge coated with TiAlCrYN - prepared by PIPS. The two preparation techniques are described in Chapter 3. The coatings examined were deposited at -75V. In the case of the 30° wedge, a region in which the coating on the edge was homogenous was selected for the sample preparation. The TiAlN/VN sample was examined using electrons with energy 400 keV, while in the case of TiAlCrYN sample the energy was 200 keV.

6.1. The coating on the edge of a 30° wedge coated with TiAlN/VN at -75V

6.1.2. The microstructure of the coating

TEM micrographs of the coating on the edge at two different magnifications are shown in Fig.6-2 and Fig.6-3. The grain structure of the coating is clearly visible - the contrast between the grains being related to their different crystallographic orientations relative to the electron beam. The coating in the edge region is composed of coarse grains with different shapes, with the exception of a narrow region right on top of the edge which has a fine grained structure (see Fig.6-4a). The structure of the grains was examined using the electron diffraction. Fig.6-6 compares the diffraction patterns from the two types of grains. The area selected by the diffraction aperture is marked on the bright-field image. In the fine grained region right on top of the edge (Fig.6-6a), the diffraction image is typical for polycrystalline material (Lindsay, 1999). This is in contrast with the single crystal diffraction pattern shown in Fig.6-6b, which proves that there is one large grain inside the aperture (and not several smaller grains superposed one next to each other).

Fig.6-2: Low magnification bright-field TEM image of the near-edge region of sharp 30° wedge coated with TiAlN/VN at -75V (cross-section prepared by FIB).

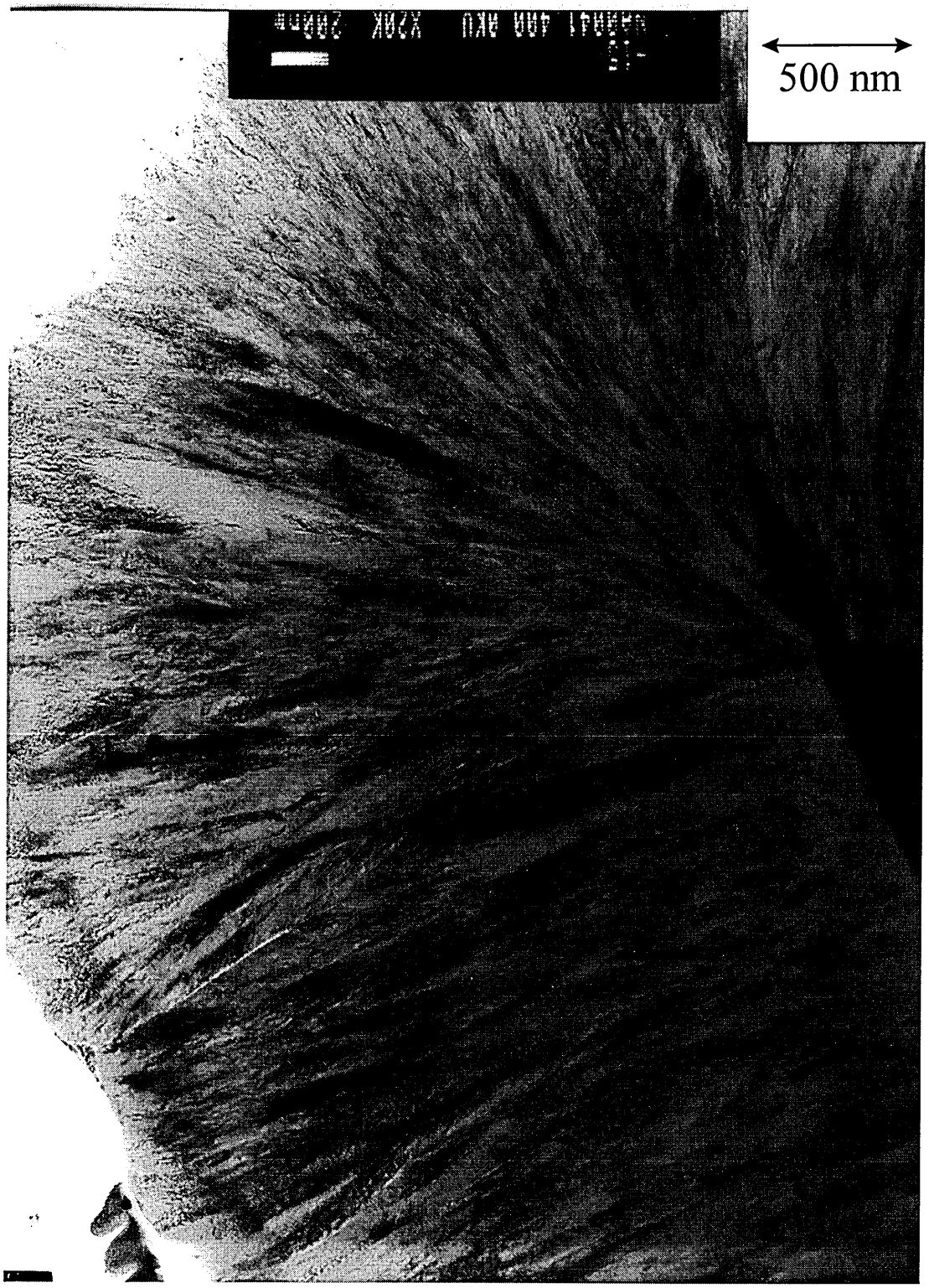

Fig.6-3: Bright-field TEM image of the near-edge region of sharp 30° wedge coated with TiAlN/VN at -75V.

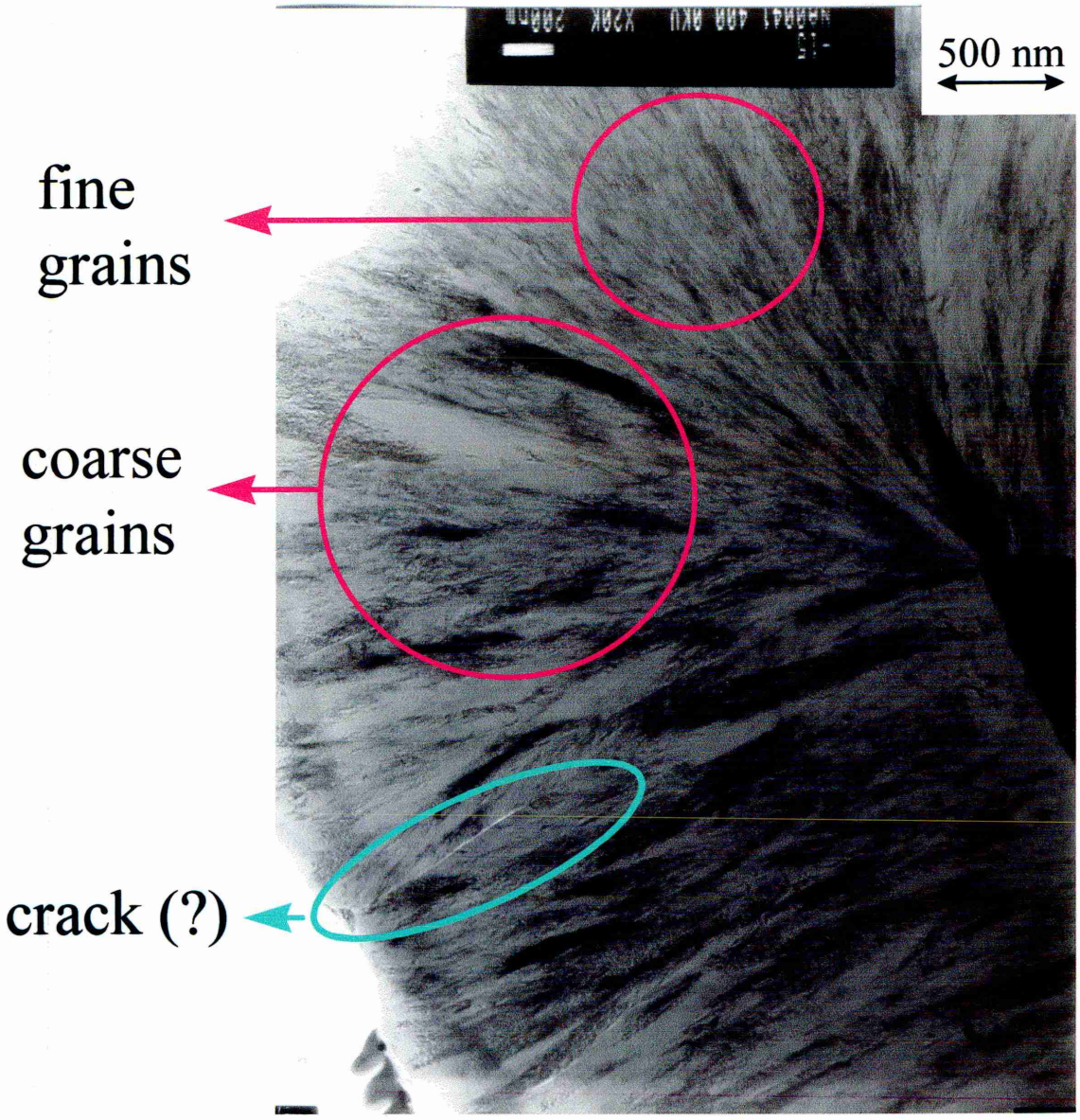

Fig.6-4: Bright-field TEM image of the near-edge region of sharp 30° wedge coated with TiAlN/VN at -75V, showing the structural features described in the text.

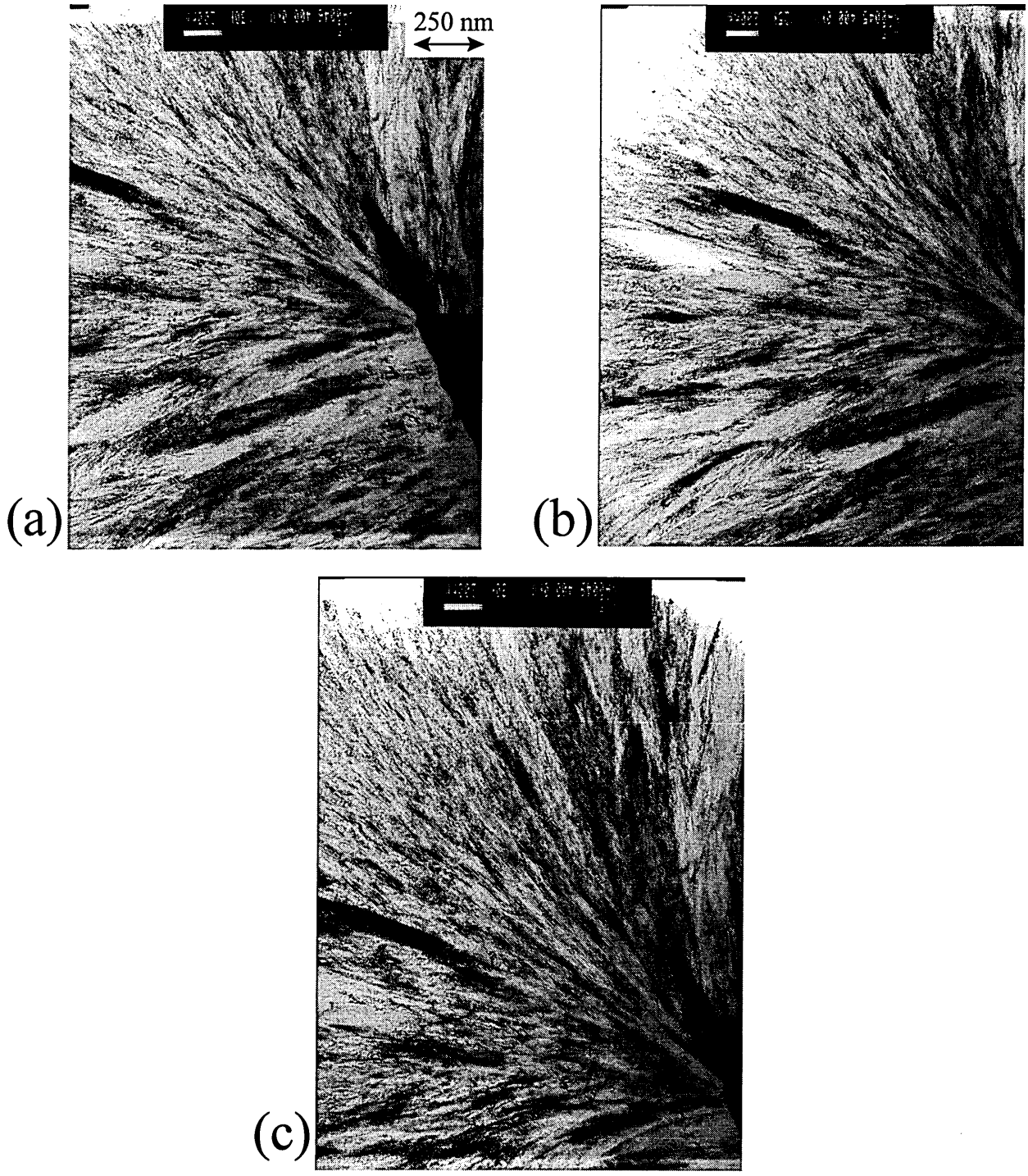

Fig.6-5 : Bright-field TEM images examining in more detail the grain structure on the 30° wedge.

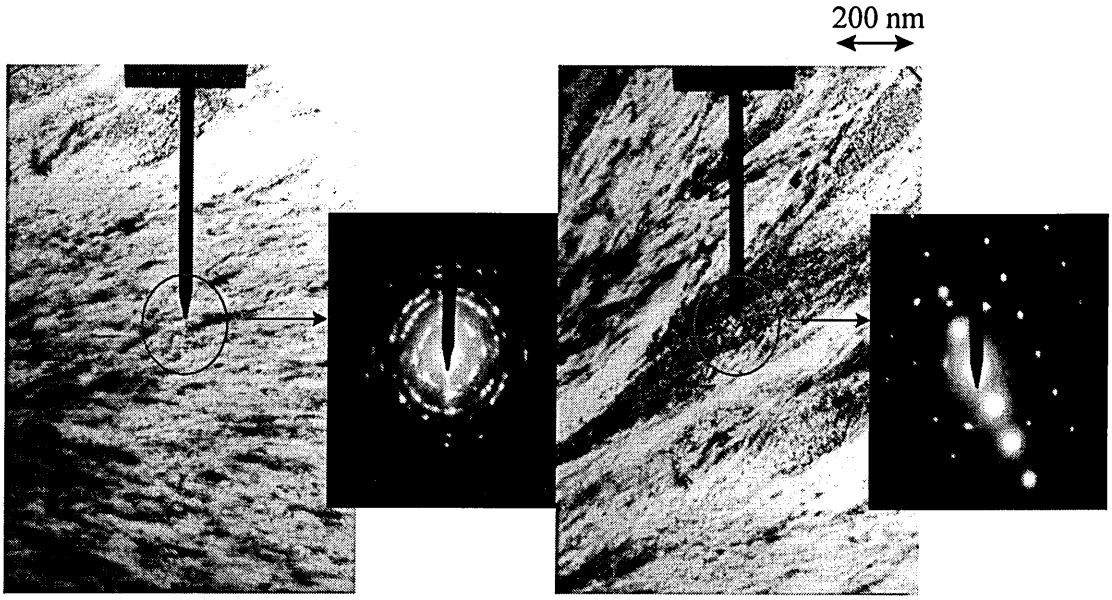

Fig.6-6: Diffraction patterns taken in: (a) the fine-grained region on top of the edge (region A), (b) the coarse-grained region next to the edge (region B). The position and the size of the region contributing to the diffraction pattern is shown on the bright-field images.

The grain structure of the coatings is strongly influenced by the characteristics of the ion bombardment. The size of the individual crystals is related to the amount of energy present in the growth layer during the condensation of the deposited atoms - influenced by the substrate temperature, the ion flux and the ion energy (Sundgren, 1995). We have seen in Chapter 2 (section 2.2.1.) that an increase in the ion flux can have similar effect on the coatings as an increase in the growing temperature, which promotes the growth of larger grains (structural zone models - Fig.2-5.). The work of Hultman (1991) on flat TiN coatings deposited under conditions similar to ours (magnetron sputtering, deposition bias -100 V), has shown that the grain size of coatings deposited at $J_i/J_{me} \sim 6$ was 2 - 5-times larger than at $J_i/J_{me} \sim 2$. An increase in the ion energy can also lead to an increase in the size of the grains - if the energy (and the flux) are not too high, as shown in (Sundgren, 1983). If the ion energy is however increased above that required for obtaining dense coatings, ion-induced defects as well as the ions become incorporated into the coating - which can lead to a continuous renucleation during the growth and thus disrupt the columnar microstructure.

In the case of wedge-shaped samples, the ion flux in the region shown on the cross-section in Fig.6-3 is similar to that above a flat surface (Fig.5-12 in section 5.2.2.e). The important effect affecting the properties of the coating in this region is however the angle of incidence of the ions. Its distribution shown in Fig.6-1 can be directly related to the grain size distribution on the cross-sectional image. The distinctive region on top of the edge in which the grain structure is different from the rest and which becomes wider with increasing the radius of the growth surface (Fig.6-7), is coinciding with the simulated region of perpendicular incidence of the ions (Fig.6-1). In this region, both the flux and the incidence of the ions are similar to those above a flat surface and so should thus be the internal structure. In the rest of the edge region, the ions enter at very steep angles of incidence (up to 75° for the 30° wedge - Fig.5-7), which has a significant impact on the growing coating as it increases the total amount of energy transferred from the ions to the atoms in the growing layer (providing the angle is not too close to 90°). The effect is shown schematically in Fig.6-8. If we suppose that the ions entering the coating travel in average through roughly the same length inside the material before being stopped or rescattered, then the energy which the ions give to the growing coating via collisions is, in the case of non-normal angle of incidence, concentrated towards the growth surface where the condensation of the crystals is taking place. The energy of the ions being low, this change in the incidence of the ions is similar to an increase in the ion flux (at a low energy) or an increase in the substrate temperature - which both increase the average energy per atom without causing significant defects. We have used TRIM simulations in order to quantify the change. Fig.6-9 shows the simulated distribution of the ions inside the coating for angles of incidence 0° and 75°, as well as the penetration depth simulated for a range of incidence angles. In the near-edge region of the 30° wedge, there is roughly the same number of ions bombarding the surface as in the flat case, but their energy is concentrated to 3-times smaller region. This means that there is roughly 3-times more energy transferred to the growing layer, which enables the growth of the large crystals we can see in Fig.6-4.

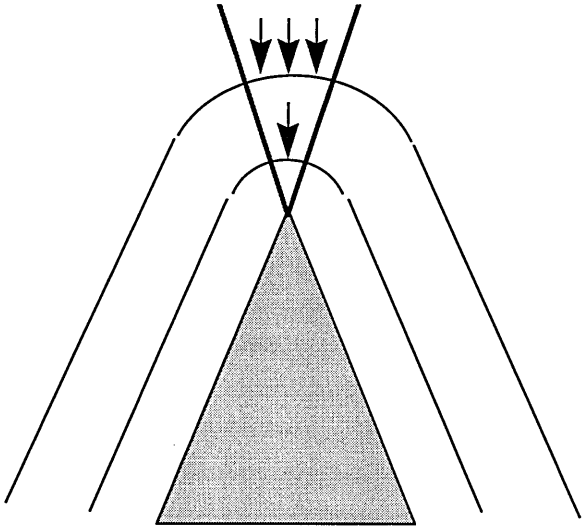

Fig.6-7: Schematic drawing of the region on top of an edge in which the growth surface is perpendicular to the direction of the ion bombardment. As the coating grows and its thickness is increasing, the extent of this specific region increases.

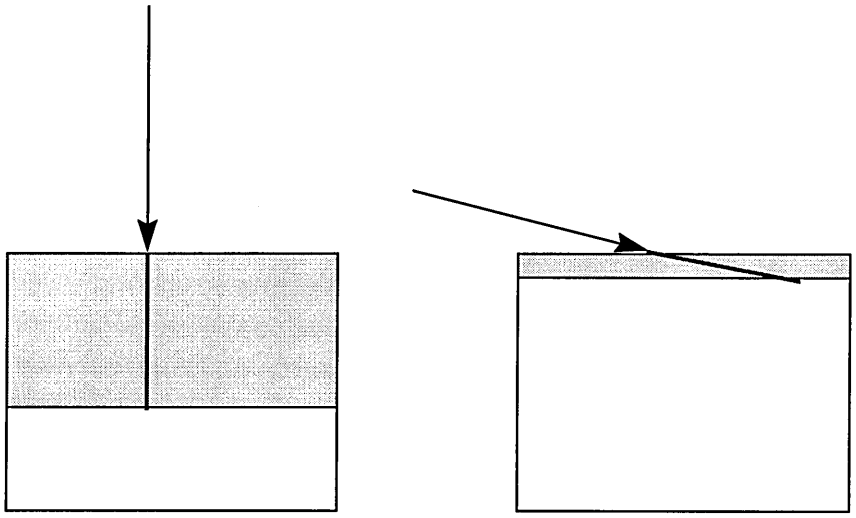

Fig.6-8: Schematic drawing of the dimensions of the region affected by the ions - arriving at two different angles of incidence. The path of the ions inside the material has the same length in both images.

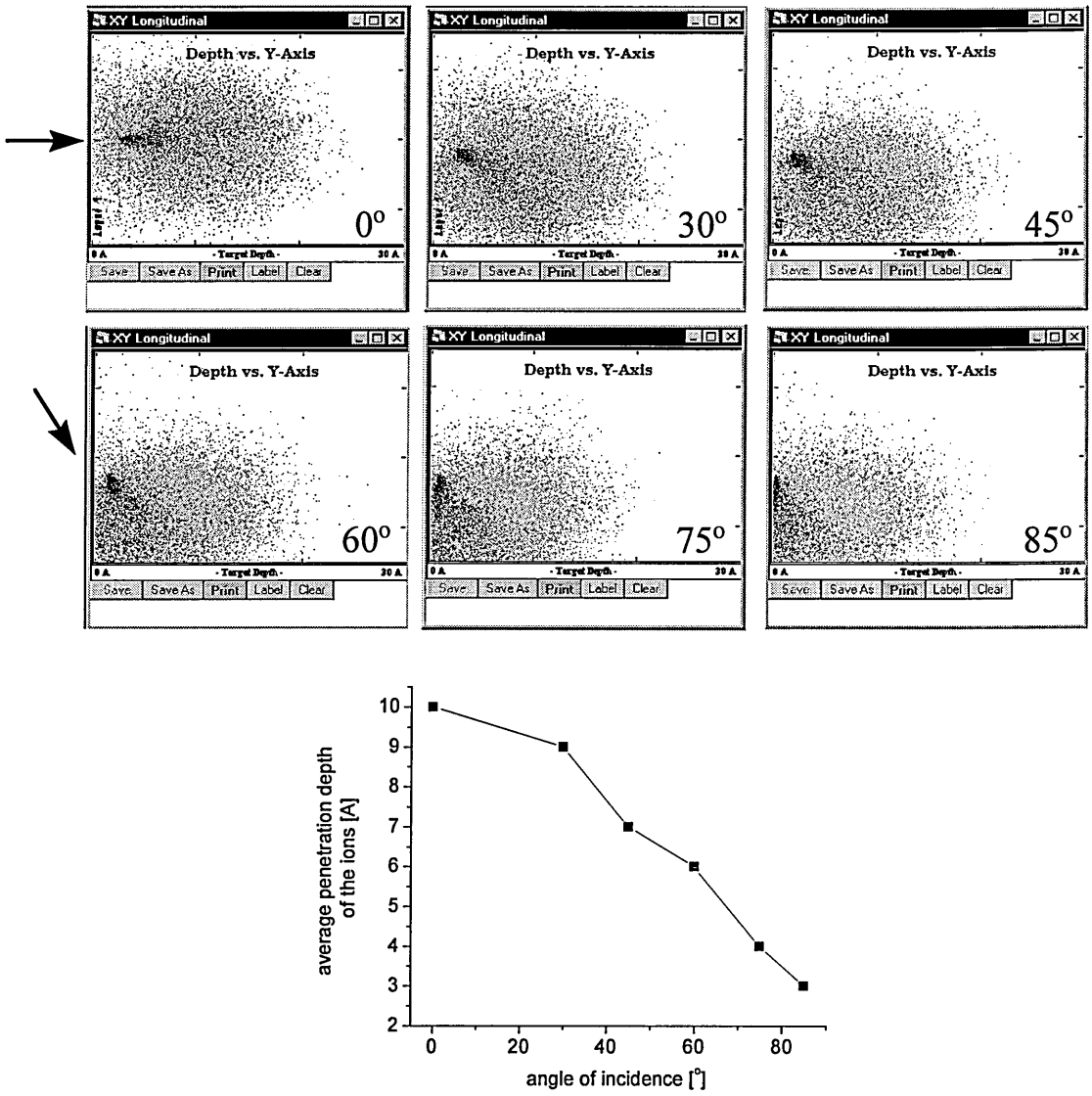

Fig.6-9: Simulated interaction between a solid material ($Ti_{0.5}Al_{0.5}N$) and ions (Ar^+, 75 eV) - arriving at a range of angles of incidence (from perpendicular to the surface to very steep angles) - showing the change in the penetration depth of the ions (TRIM). The direction of the ion flux, for angles 0° and 60°, is marked by the arrows.

A comparison between the structure of the near-edge region (the region on top of the edge is denoted as region A, the rest as region B) and the same coating deposited on a flat substrate is presented in Fig.6-10. The typical grain size in region B, which grows under steep angles of incidence of the ions, is much larger than in the flat coating. On the other hand the average grain size in region A, where the ions arrive perpendicularly, is closer to the flat case. The fact that the grain size here is actually lower than in the flat coating can be related to slightly different ion flux and growth

conditions between the two regions. Furthermore, the distribution of the grain sizes is related to the distribution of the ion bombardment around the edge. During deposition on a flat substrate, the ion flux bombarding the growing coating is uniform all over the sample and so is thus the coating structure (Fig.6-10c). On the edge however, the sudden change in the angle of incidence of the ions (from ~75° to 0°) corresponds to the sudden change from fine grains to coarse grains which can be observed in the higher magnification image in Fig.6-5b.

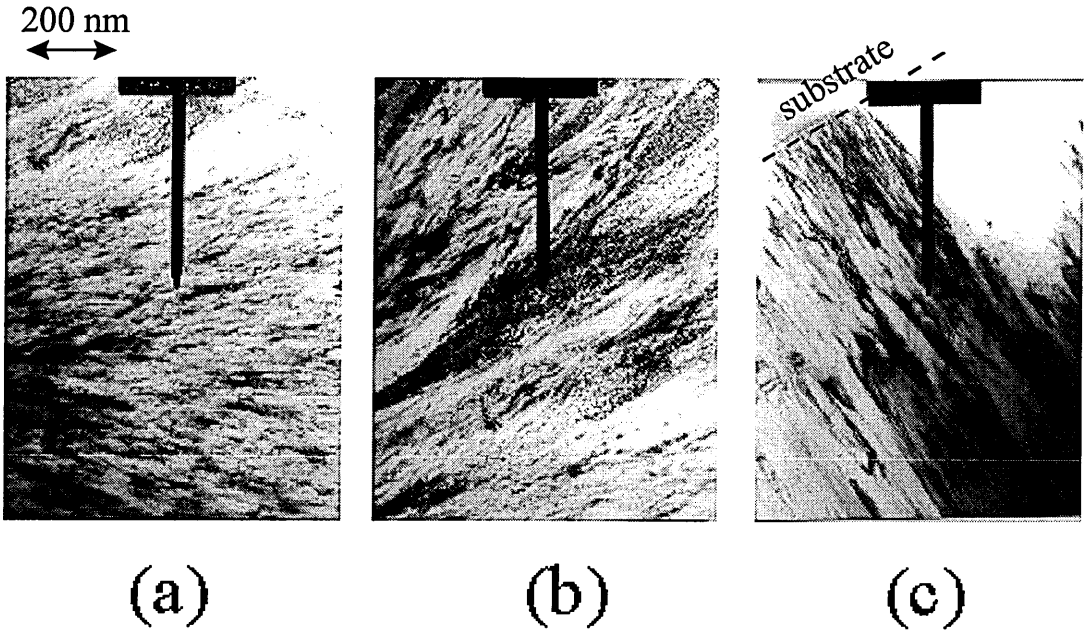

Fig.6-10: Bright-field images comparing the coating deposited on the 30° wedge - (a) region A, (b) region B - with the same coating deposited on a flat surface (c). The images were taken at the same magnification.

Apart from the changing ion characteristics, another difference between the coating in the near-edge region and a flat coating is the 'curvature' of the coating on the edge. Fig.6-5c shows the complicated arrangement of the grains in the 'curved' region close to the edge, in contrast with the regular and uniform grains on the flat substrate (Fig.6-10c). The region in which the coating is curved is furthermore a region in which the thickness of the coating locally increases (if the resputtering is not too high) because of the large solid angle from which atoms can arrive towards the top of the wedge. The two regions - region C in which the coating is 'curved' and thicker, and region D where the coating is 'flat' - are marked in Fig.6-11a. We can expect that the boundary between

these two types of coatings will be a 'critical' region where, if the stress or the external forces are high enough, the coating is likely to break and detach from the edge. TEM observations (Fig.6-4) have revealed a thin white line running along the boundary marked in Fig. 6-11a. Although the identification of this feature is not completely unambiguous, it seems to be a crack across the coating. This could to be supported by an observation made during the sample preparation where, while performing the mechanical grinding of the thin cross-sections, the top part of the coating very often detached from the rest of the sample in a way shown schematically in Fig.6-11b. This effect is due to mechanical stresses present in the coating on the edge, not stresses due to changes in the properties of the coating due to changing ion bombardment, which happen in a much larger edge region and which are the most significant some distance away from the edge. The delaminations of the coating on top of wedges observed by SEM ('zone 2' in Fig.4-9) are most probably caused by the combination of the two factors.

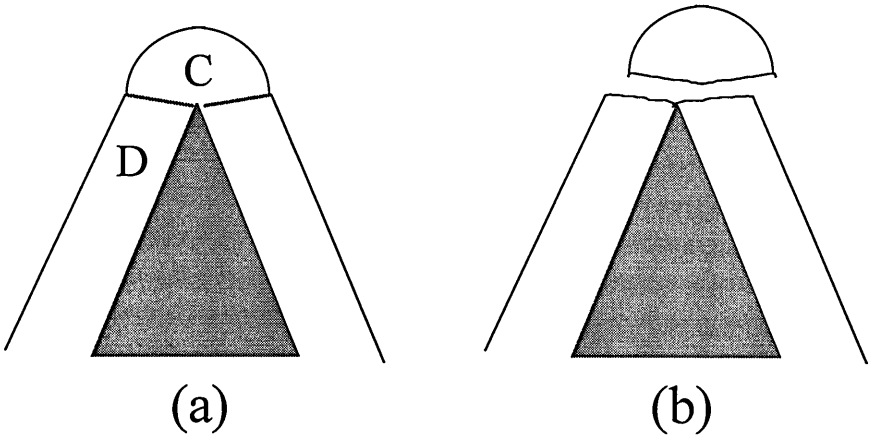

Fig.6-11: (a) Schematic drawing showing the region near the edge where the coating is curved (region C). (b) Schematic representation of a problem encountered during TEM sample preparation from the coated wedges - the coating was often observed to detach from the rest of the sample in a way shown in the image.

6.1.2. The texture of the coating

The evolution of the crystallographic orientation of individual grains inside a polycrystalline material prepared by PVD is driven by kinetic and/or thermodynamical

forces - related to the deposition conditions. Most of the grains will be growing with a certain specific orientation in the growth direction - which will be the most favourable orientation in the given conditions. This orientation is called 'preferred orientation' or also 'texture' (Ensiger, 1994).

The principle of the texture determination for cubic materials is to take a bright-field image at the same time as the diffraction image in order to be able to mark the growth direction on the diffraction pattern by superposing the two images. A magnification has to be chosen at which the two images are aligned, and not rotated one relative to each other. The diffraction spot corresponding to the plane oriented along the growth surface will be situated on the growth direction line, as explained in Fig.6-12.

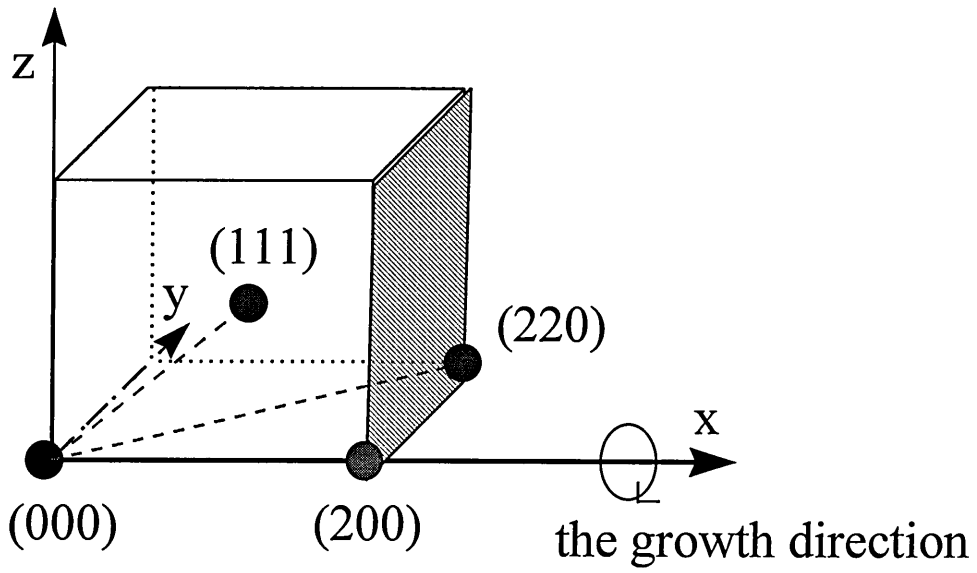

Fig.6-12: The principle of texture measurements for a cubic material, shown on the example of (200) texture. Let's consider the electron beam directed along the z-axes and the diffraction pattern projected into the (xy) plane. The x-axes is selected as the growth direction. If the cube is oriented with (200) plane in the growth direction (which means that (200) is the surface plane of the crystallite), the diffraction in the (200) direction will be aligned with the growth direction (the x-axes). The (200) direction being fixed, the cube can rotate freely in the (yz)-plane. For certain angles of rotation around the x-axes, the other spots - (111) and (220) - can intercept the (xy) plane, and thus become bright on the diffraction image. The amount of rotation required and thus the relative position of the spots in the diffraction pattern plane can be calculated from the geometry of the cube.

Examples of diffraction patterns revealing a (200) and a (111) preferred orientation are shown in Fig.6-13. More details about texture measurements in PVD grown coatings can be found in (Lindsay, 1999).

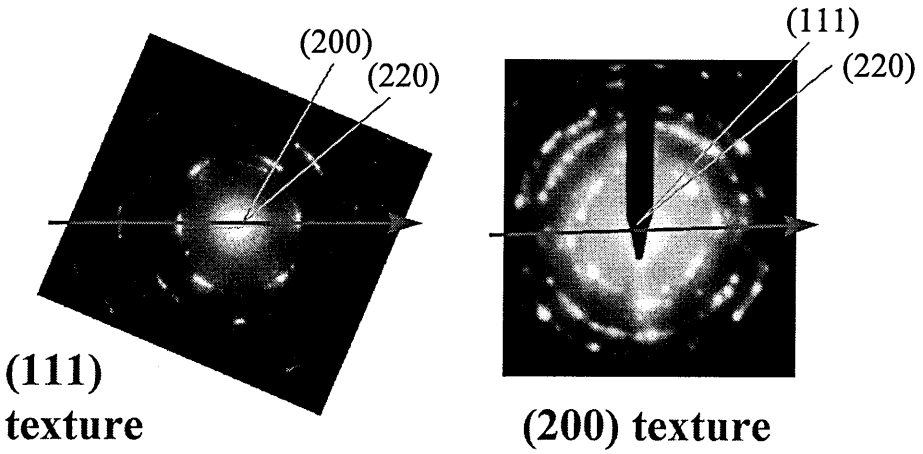

Fig.6-13: Diffraction patterns showing a (200) and a (111) texture inside the TiAlN/VN coating (with fcc structure). The growth direction, marked by arrows, was taken from bright-field images. The orientation corresponding to each spot can be determined measuring the relative distance between the spot and the origin of the pattern. On both patterns only one orientation is present in the growth direction - showing that most of the grains situated within the aperture are oriented in the same direction.

The texture measurements on the cross-section from the 30° wedge are summarised in Fig.6-14. The vicinity of the edge was mapped and the preferred orientation of the grains was colour coded. The diameter of the area selected for each measurement was ~500 nm. The figure reveals that most of the grains near the edge grow with (200) and (220) orientations. This is in contrast with measurements on the same coating deposited on flat substrates, where (111) texture was observed (Münz, 2000). The difference can be related to the different driving force behind the formation of these textures. TiAlN, as well as TiN, are fcc materials. For this crystallographic arrangement, (111) plane exhibits the densest array of atoms, while (100) plane (equivalent to the (200) plane) is the plane with lowest surface energy. The (111) orientation in the growth direction is thus favoured when the adatoms have low energy and the crystals evolve by kinetic competition - the densest orientation has the highest probability of surviving under the ion bombardment. The (100) orientation becomes

preferable when the adatoms, colliding with the ions, receive enough energy to sample several surface binding sites before being incorporated into the coating and thus 'choose' the energetically most favourable position. The emergence of the higher-energy (111) surface as the preferred orientation is thus due to kinetic limitations while the appearance of the (200) texture is due to thermodynamic driving forces (Hultman, 1995). In agreement with this, TiAlN (and TiN) coatings were observed to change from (111) preferred orientation to (complete or partial) (200) orientation - with increasing the ion flux, the ion energy or the surface temperature, as each of these factors increases the energy of the adatoms (Adibi, 1993). The (200) orientation is thus more likely to develop in the near-edge region where, due to the steep angles of incidence of the ions (except in the narrow region right on top of the edge), the adatoms in the growing layer receive increased amount of energy (Fig.6-9). It is similar for the (220) orientation, the surface energy of which is also lower than that of the (111) orientation. This seems to correspond with the experimental results presented in Fig.6-14. However, in order to have a complete picture, more measurements done on several samples would be needed.

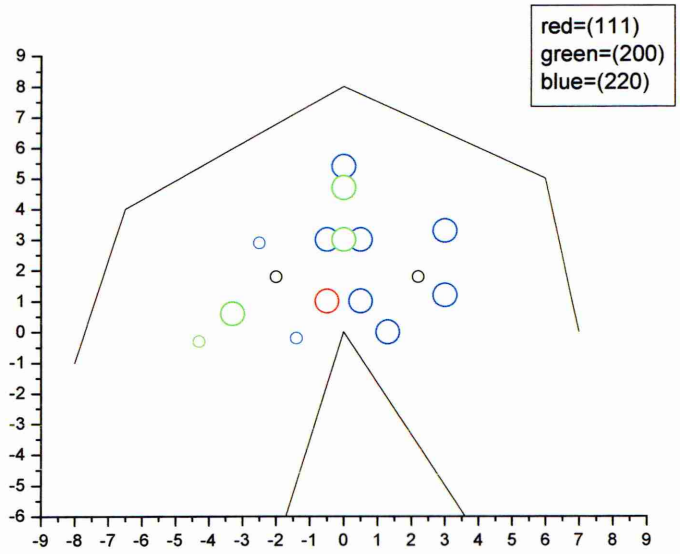

Fig.6-14: Summary of the texture measurements on the cross-section shown in Fig.6-3. The position of each circle shows the position of the diffraction aperture on the sample. The colour marks the preferred orientation of the grains within the aperture.

6.2. The coating on the edge of a 60° wedge coated with TiAlCrYN at -75V

Fig.6-15 presents TEM cross-section from the edge area of the 60° wedge at two different magnifications. The worse resolution of the images when compared to the previous cross-section is due to higher thickness of the sample prepared by PIPS. A further difference is related to the thickness uniformity - the FIB method results in a cross-section with a uniform thickness (Fig.6-2), while this is much more difficult to achieve with the PIPS instrument. Nevertheless Fig.6-15 shows that, with very careful preparation, electron transparent samples from sharp edges can be in principle prepared even with the PIPS method, the advantage being that FIB is a very expensive and not widely available preparation technique.

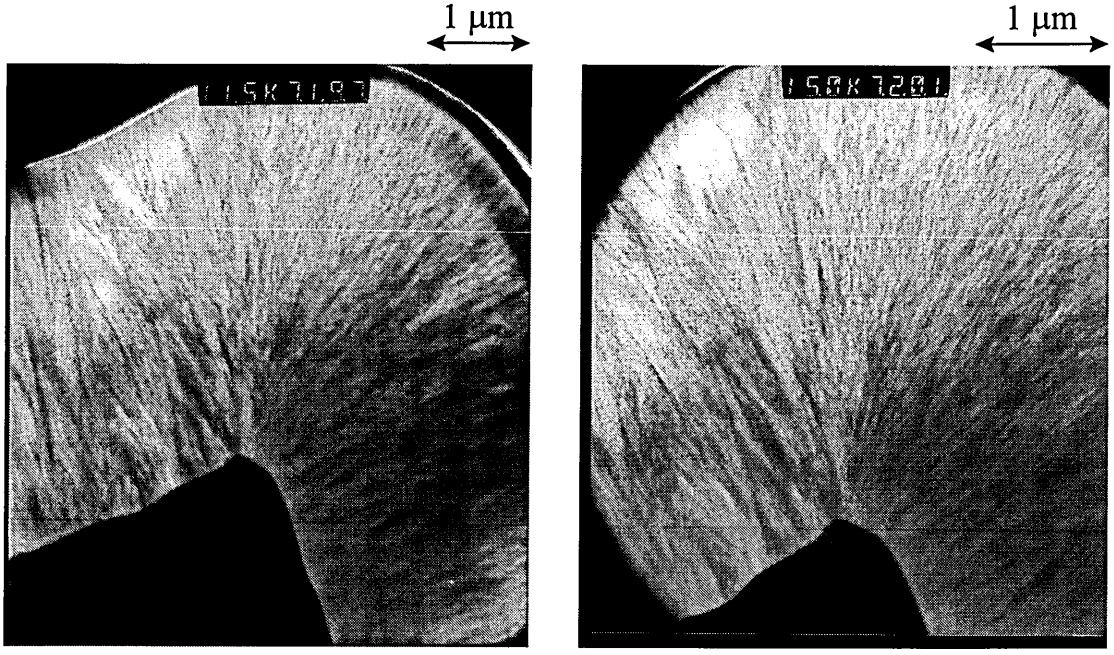

Fig.6-15: Bright-field TEM images of the near-edge region of sharp 60° wedge coated with TiAlCrYN at -75V (cross-section prepared by PIPS).

The microstructure of the coating on the 60° wedge seems to have similar characteristics as the cross-section from the 30° wedge. The grain structure can be best observed on the left side of the image where the sample is thinner. We can see a fine-grained region right on top of the edge and coarser grains next to it. In the middle of the coating, a thin black line, marked in Fig.6-16, is visible. This line, caused by an

interruption in the deposition process due to a power failure, corresponds to a thin oxide layer formed on the top of the sample during the interruption. It allows us to see the growth surface midway through the deposition process and to check that, in agreement with our model, the width of the fine-grained region on top of the edge seems to correspond with the width of the region where the angle of incidence of the ions is perpendicular to the growing surface - as shown in figure.

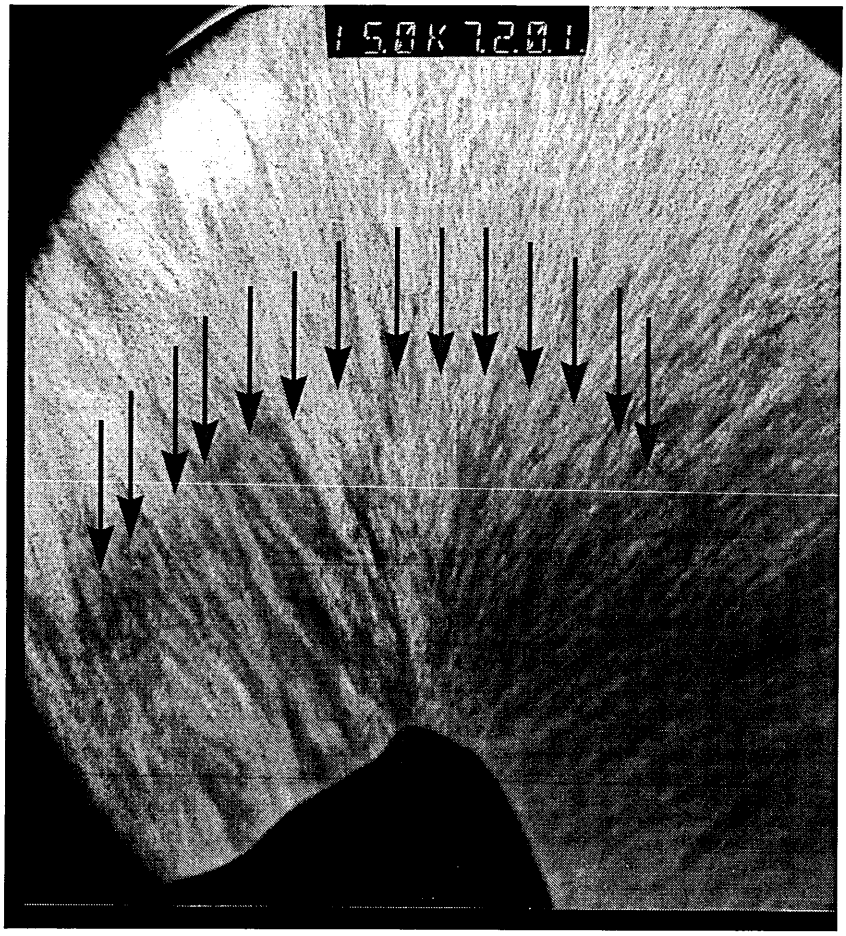

Fig.6-16: Bright-field TEM image of the near-edge region of the 60° wedge. The arrows show the direction of the ion bombardment relative to the growth surface, which can be seen on the cross-section as a thin black line.

Chapter 7: Cutting tools coated by ion-assisted PVD

Changes in the properties of coatings in the vicinity of sharp edges studied in this thesis are of a particular importance for ion-assisted coating of cutting tools. Any change in the crucial cutting edge region, which in practical applications means in a region up to ~0.3 mm from the edge, can affect the performance and the lifetime of the tool (Sandvik, 1990). This chapter applies the model established in Chapter 6 to the case of industrially-used cutting tools and shows how it can be used to better understand and possibly avoid or decrease the unwanted effects.

7.1. Edge-related effects observed on cutting tools

Fig.7-1 shows a cross-section (imaged by SEM) from a cemented-carbide drill coated with TiAlCrYN, used industrially in dry high speed machining.

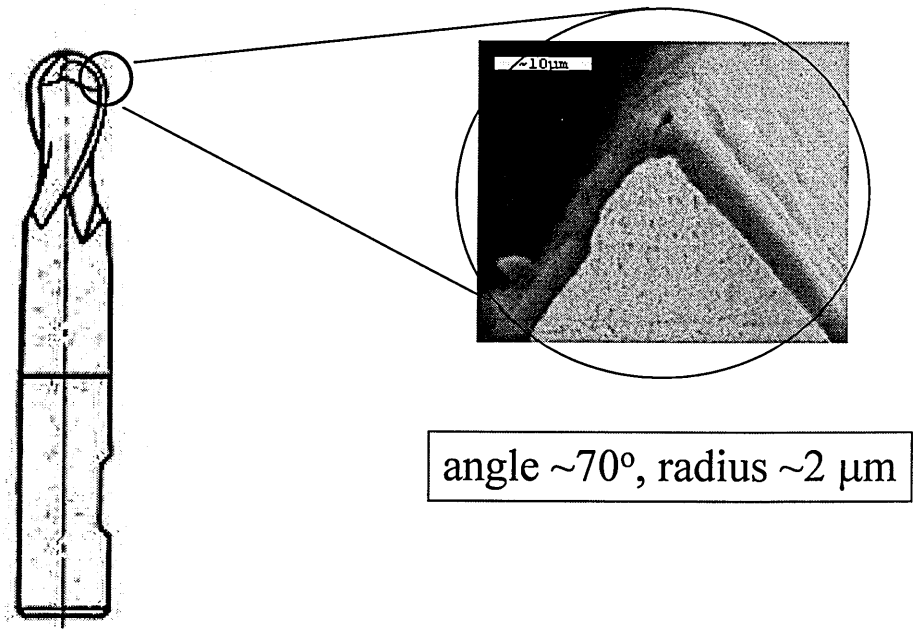

Fig.7-1: Schematic view of ball-nosed end mill and SEM micrographs of the cross-section from the cutting edge, coated at -75V.

The tool was coated using the same deposition process as in the case of the wedges, at substrate bias -75V. The cross-section shows the coating on the cutting edge situated at the top of the tool (Fig.7-1). The angle of the cutting edge is ~70°, while the radius of curvature is ~2 μm. The coating on the edge deposited at this low substrate bias value is homogenous. The increased bombardment in the edge region affects however the composition of the coating - Al-depletion (~10%) was observed near the edge (Fig.7-2). The value is similar to that observed on the 90° wedge coated at -75V (Fig.4-2 and Fig.4-6 in Chapter 4), which has similar edge geometry.

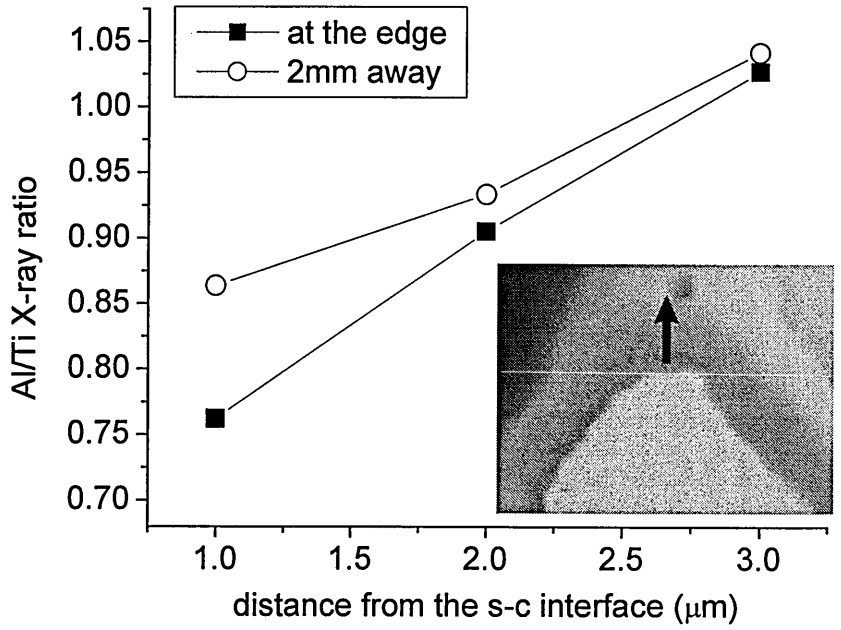

Fig.7-2: Al/Ti X-ray ratio measured across the coating - on top of the cutting edge, and 2 mm away from the edge.

In order to examine the influence of the substrate bias, the same type of drilling tools was coated at a range of bias values from -75V to -150V. The drills were coated with TiAlN/VN (using the same process as described in Chapter 3). Compositional maps of the cutting edge region on the different drills are presented in Fig.7-3. The tungsten map detects the substrate, while the coating is visible on the vanadium map - the combination of the two maps allows direct assessment the homogeneity of the coating in the edge area. The observed changes can be directly related to the zone diagram established in Fig.4-9 (Chapter 4). The coating deposited at -75V is

homogenous (no tungsten is visible) and the situation is similar at -85V (which is not shown in the figure). When the substrate bias reaches -95V, the coating starts to partially delaminate from the edge which reveals the substrate in this region (the thin line bright in the tungsten map). The delaminations are more pronounced at -125V. At the highest substrate bias -150V, there is a region around the edge in which the coating is missing almost completely and it is therefore dark in the vanadium map. The substrate bias values which correspond to the three situations (= the three 'zones') are similar to the values expected from Fig.4-9 for an edge with angle ~70°.

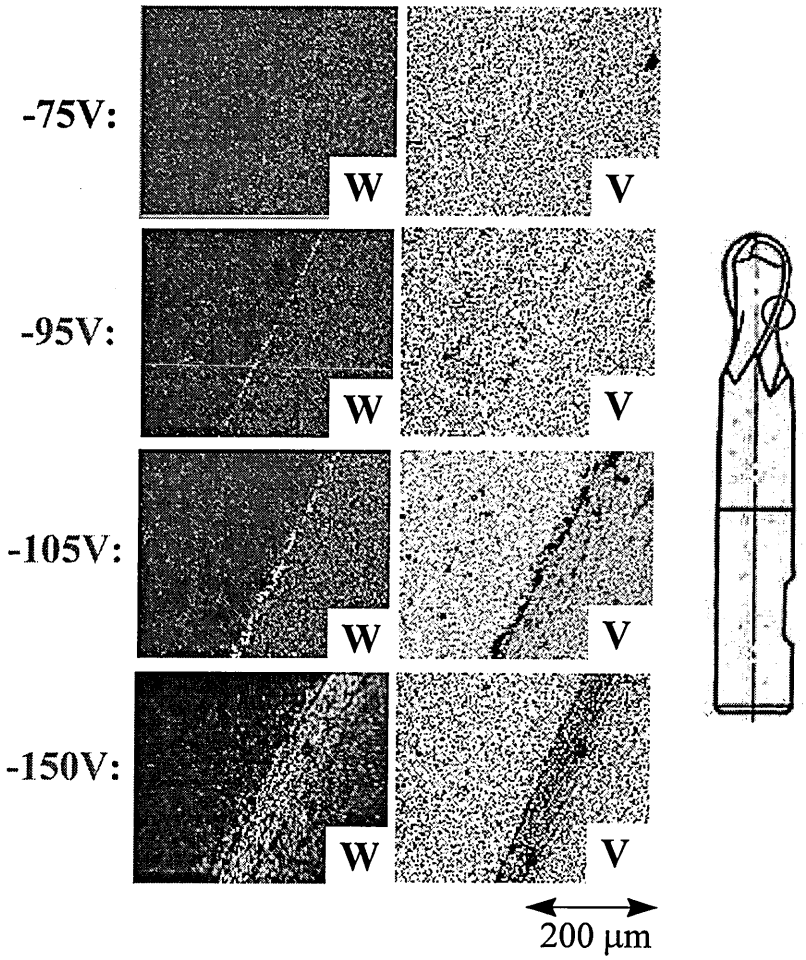

Fig.7-3: Tungsten and Vanadium EDX compositional maps of the cutting edge region (marked on the adjacent drawing) corresponding to tools coated at a range of substrate biases.

The changes in the properties of coatings in the cutting area mean changes in the performance of the coatings in practical applications. The disruption of the

homogeneity of the coatings in the cutting edge area at higher biases has necessarily a negative impact on the cutting tool performance and lifetime. The effect of the Al-depletion is also very important as a decrease in the Al concentration means decreased oxidation resistance of the coating in the crucial edge region (Lii, 1998). Extensive research examining the properties of TiAlN as a function of the Al/Ti ratio has shown that even a small change in the relative ratio of the two elements can furthermore lead to changes in the colour (Huang, 1995), hardness and wear (Lii, 1998), as well as stress and adhesion of the coatings (Tonshoff, 1997 and 1998), and their internal structure and texture (Wahlstrom, 1993). Best performance of the coating in practical applications was observed for Al/Ti stoichiometric ratio ~1.

The performance of the coatings deposited on the drills was determined by cutting tests. A typical result from one of the tests is shown in Fig.7-4. The increase in the substrate bias value during the coating deposition was observed to have a negative impact on the performance and thus the lifetime of the coated tools. For the test shown, the lifetime of the tool at -95V was ~20% shorter and at -150V ~60% shorter than the lifetime at -75V. This contrasts with the case of coatings deposited on flat substrates which usually show improved mechanical properties with moderate increase in the deposition bias (Hakansson, 1987), and thus shows the importance of the understanding of effects happening in the edge region.

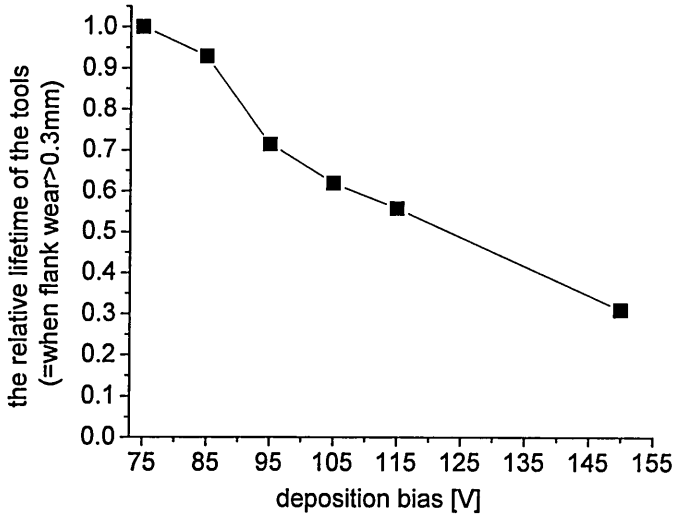

Fig.7-4: Example of results from cutting tests, done to asses the lifetime of the tools coated at different substrate biases.

7.2. Optimisation of the deposition process

Table VI (from Münz, 1991) compares the most important deposition parameters of various commonly used ion-assisted PVD techniques: low-voltage and high-voltage electron-beam vacuum coating (LV-EB and Tri-EB), the random-arc and steered-arc processes (R-Arc and S-Arc), the double-cathode sputtering (Sp) and the unbalanced magnetron sputtering (UBM).

	LV-EB	**Tri-EB**	**R-Arc**	**S-Arc**	**Sp**	**UBM**
Gas	$Ar+N_2$	$Ar+N_2$	N_2	N_2	$Ar+N_2$	$Ar+N_2$
Total pressure ($\times 10^{-3}$ mbar)	2	6	5	7	8	1-50
Deposition temperature (°C)	450	500	425	425	350	500
Deposition rate (A/s)	9	25	24	8	52	7-8
Substrate bias voltage (V)	50	110	100	100	85-100	60-80
Ion current density (mA/cm^2)	3-5	2	1.9	1.6	0.6	2.5-6
Ion-to-metal arrival rate ratio (at the substrate)	4.9	0.95	0.94	2.4	0.14	4-6.4

Table VI: Comparison of the conditions used for the deposition of TiN-type coatings by different PVD techniques.

The advantage of the UBM sputtering over the other techniques is its ability to produce high ion-to-metal arrival rate ratio, while allowing exact controllability of the operation (unlike the EB process). The high-flux low-energy ion irradiation used in UBM allows production of superior quality coatings (dense coatings with small number of defects - Chapter 2). The use of high ion fluxes, which are furthermore mostly composed of Ar ions, however enhances the problem of the possible non-uniformity of the ion bombardment in the case of non-flat samples. This is especially critical in the case of sharp edges where the effect of the bombardment can become significantly increased, as shown in Chapter 4. The problem requires careful analysis (not only in UBM, but in any

ion-assisted deposition) and, if necessary and possible, optimisation of the deposition parameters with regard to the effects happening in the edge region.

Our analysis of the edge-related effects has shown that the important parameters which affect the magnitude and spatial extent of the changes (besides the ion-to-metal ratio) are:

- the edge geometry - which affects the shape of the plasma sheath and thus the ion flux and angle of incidence distribution)
- the substrate bias of the edge - which affect the ion-coating interaction as well as the plasma sheath width
- the type of ions used - which affects the ion-coating interaction
- the plasma characteristics: plasma density and plasma temperature - which affect the ion flux entering the plasma sheath, as well as the sheath width.

Decreasing the sharpness of the edge could decrease the edge-effects. Often, however, a certain specific geometry, usually quite sharp, is required by the cutting operation. The situation is similar with the plasma characteristics (density and temperature), which are determined by the design of plasma source and the type of the deposition process itself, and are thus usually fixed and have limited possibilities of further improvements. The most easily varied parameter is the substrate bias during the deposition. During UBM coating of industrially used cutting tools, its value is kept low (~75V) in order to decrease any unwanted changes in the cutting edge area as much as possible (Münz, 2003). Further decrease in the bias would compromise the coating densification. However, even at this low value, changes in the coating composition, and even in the homogeneity (if at corners) can occur (Chapter 4). The situation can be influenced by another parameter - the type of the bombarding ions. Replacement (partial or total) of the Ar-ions by lighter N-ions, for example, would decrease the sputtering yield of the ions and thus reduce the resputtering effects. This possibility was tested in the case of the TiAlN/VN coating applied on the drilling tools. Fig.7-5 compares the cutting tools coated under the same deposition conditions, but two different values of N_2-gas pressure: the standard value ~1×10^{-3} mbar and an increased value of ~4×10^{-3} mbar, while keeping the Ar-gas pressure constant at ~2×10^{-3} mbar. The increase in the N_2-pressure, which means a larger fraction of N-ions (mainly N_2^+) relative to Ar-ions, has

resulted in a decrease of the edge-related problems. At the higher pressure, the substrate bias could thus be increased to -95V without losing the homogeneity of the coating on the edge. Decrease in the Al-depletion (Fig.7-6) and improved cutting performance was also observed. Any possible 'optimisation' of the UBM process for coating of sharp edges needs however to be carefully analysed, as any change in the deposition parameters has an impact on the coating process and the coating properties itself.

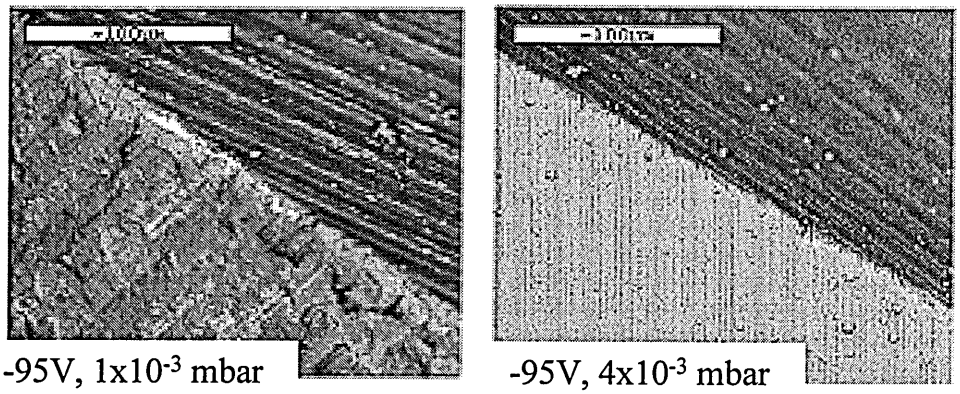

Fig.7-5: SEM micrographs of the cutting edge on tools coated at two different N_2-pressure values. The substrate bias in both cases was -95V. The brighter areas along the edge on the first image correspond to coating delaminations which reveal the substrate underneath. (The images were taken using the backscattered electrons contrast.)

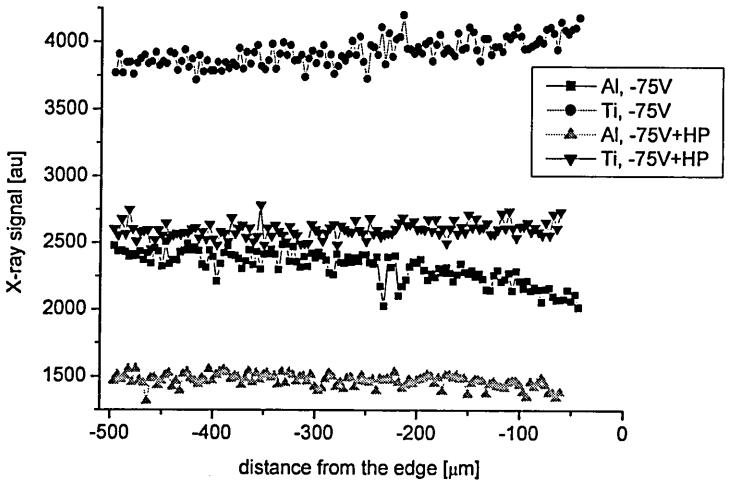

Fig.7-6: The Al and Ti EDX linescans as a function of the distance from the edge - measured on tools coated at substrate bias -75V, but at two different values of N_2-pressure (HP = higher pressure).

Chapter 8: Conclusions

Our work demonstrates the difference between ion-assisted PVD on flat substrates and on real 3D samples containing sharp edges and corners. It complements the vast amount of previous work on ion-assisted PVD - which studied coatings deposited on ideal flat substrates. For the first time, detailed electron microscopy analysis of the edge-related effects and their influence on the coating properties was done. The most important achievement of this work is the establishment of a physical model, based on simulations of the plasma-surface interaction during the deposition, which allows us to better understand and to quantify the changes in the edge region.

The alteration of the electric field, and thus the shape of the plasma sheath, in the vicinity of biased non-flat surfaces immersed into plasma can significantly affect the characteristics of the ions bombarding the surface during a coating deposition. In the case of sharp free-standing edges and corners, the coating in the edge region grows under higher ion flux. Furthermore, the angle of incidence of the ions in this region will be altered: the incidence will change from perpendicular to the substrate - far from the edge, to along the wedge plane of symmetry - near the edge. This means that there will be more ions in the vicinity of sharp edges and they will arrive at the surface at oblique angles of incidence. Both these factor will have an impact on the growth of the coating. The oblique incidence of the ions will increase their sputtering yield (the probability with which they can remove atoms from the growing coating) which, combined with the increased number of the ions, leads to increased resputtering rate of the coating growing in the edge region. The change in the angle of incidence and the flux of the ions will also affect the transfer of energy from the ions into the growing coating. These changes in the interaction between the ions and the coating atoms can have significant effect on the properties of the coating in the edge region, and thus its performance in practical applications.

Our work has studied wedge-shaped samples coated by an ion-assisted PVD process used for industrial depositions on cutting tools - closed field UBM sputtering which uses high-flux, low-energy ion irradiation ($J_i/J_{me} \sim 4$, $E_i = 75$ - 150 eV). The changes in the ion bombardment in the edge region were observed to cause:

- changes in the thickness of the coatings
- changes in the coating composition (depletion of the higher sputtering yield component, in our case Al)
- changes in the homogeneity of the coatings (cracking and delamination of the coating)
- changes in the internal structure of the coatings (alterations in the grain size, texture, and defects).

The typical spatial extent of the affected region was on the same scale as the plasma sheath width (in our case ~1 mm), with a maximum occurring at a distance from the edge of ~10% of the plasma sheath width.

The influence of the following parameters was examined in this work:

- the edge geometry:
  - the angle of the edge (30° - 90°)
  - the radius of curvature of the edge (2 μm - 500 μm)
  - two-dimensional edge vs. three-dimensional corner
- the deposition conditions:
  - the substrate bias (75 - 150 V)
  - the ion flux composition (Ar vs. N-ions).

The range of the parameters which was selected resembles the typical conditions found during coating of cutting tools with industrial scale ion-assisted PVD process, and thus have relevance to many practical applications.

Decreasing the angle of the edge resulted in increased edge-related effects. This can be explained by a greater alteration in the electric field across the plasma sheath near the edge - as was shown by simulations.

The radius of the edge, when much smaller than the plasma sheath width, produces strong local effects in the region on top of the edge. On the other hand, if it is comparable with the sheath dimensions, it will cause overall decrease, and ultimately complete cancellation, of the focusing effect of the edge on the ion trajectories.

The edge-related changes in the coating properties were found to be even more enhanced in the vicinity of three-dimensional corners, because of a much stronger electric field near the edge, compared to the two-dimensional case. This was clearly manifested by the surface topography close to the corners coated at the highest substrate

bias -150V, where not only the coating was completely resputtered, but also a range of ion-induced topographical features (such as ripples and cones) was created in the substrate. These dramatic changes were explained by up to 40-times increased resputtering rate of the ions near the corner, calculated from our model.

Another crucial parameter is the substrate bias value, which is closely related to the energy of the ions. The most significant changes were observed at the highest negative subtrate bias (-150 V) - complete resputtering of the coating and substrate erosion. However, even at biases as low as -75V, which are commonly used in practical applications, the coating on the edge was found to have altered composition, as well as altered internal structure.

The unwanted effects could however be to some extent decreased by using ions with a lower sputtering yield - in our case, replacement of Ar-ions by lighter N-ions resulted in improvement of the coating properties. Another alternative for future improvement, which we have not explored in this thesis, could be increasing the plasma density. This would reduce the plasma sheath width, and thus the magnitude and the spatial extent of the changes. It would however require a radical change in the way how the plasma is produced and the coatings are deposited.

The physical model presented in this thesis allows to quantify the edge-related effects and thus to systematically predict the influence of the above described parameters on the coating properties in the edge region. The edge-related effects can be quantified by calculating the electric field distribution around the edges, and the resulting shape of the plasma sheath. The spatial extent of the changes in the coating properties is directly related to the spatial extent of the region in which the electric field is altered by the edge. The magnitude of the changes is given by the characteristics of the ion bombardment in the edge region (the flux density and the angle of incidence) and can be described in terms of the resputtering rate of the ions. Its value can be estimated from the geometry of the sample and of the surrounding plasma sheath. The calculation of the ion trajectories across the electric field inside the sheath, and of the resulting flux and incidence of the ions at any point along the sample, furthermore allows to assess the distribution of the changes as a function of the distance from the edge. Our simplified model can be used as a good approximation of the more exact, but also more complicated, self-consistent model. It allows to estimate the edge-related

effects relatively easily in 2D as well as in 3D case, and is thus directly relevant for practical applications.

Bibliography

F. Adibi, I. Petrov, J. E. Greene, L. Hultman, J.-E. Sundgren, J. Appl. Phys. 73(12) (1993) 8580.

H.H. Andersen, H. L. Bay, 'Sputtering Yield Measurements', in: Topics in Applied Physics series - Volume 47 (Sputtering by particle bombardment I), edited by R. Behrisch (Springer-Verlag, 1981), Chapter 4.

A. R. P. de Ataide, C. Alves Jr., V. Hajek, J. P. Leite, Surf. and Coat. Technol. 167 (2003) 52.

G. Betz, G. K. Wehner, 'Sputtering of Multicomponent Materials', in: Topics in Applied Physics series - Volume 52 (Sputtering by particle bombardment II), edited by R. Behrisch (Springer-Verlag, 1983), Chapter 2.

D. Bohm, 'The Characteristics of Electrical Discharges in Magnetic Fields' (McGraw-Hill, New York, 1949), Chapter 4.

R.M.Bradley and J.M.E.Harper, J. Vac. Sci. Technol. A 6 (1988) 2390.

G. Carter, M. J. Nobes, F. Paton, J. S. Williams and J. L. Whitton, Radiat. Eff. 33 (1977) 65.

G. Carter, B. Navinsek, J. L. Whitton, 'Heavy Ion Sputtering Induced Surface Topography Development', in: Topics in Applied Physics series - Volume 52 (Sputtering by particle bombardment II), edited by R. Behrisch (Springer-Verlag, 1983), Chapter 6.

F.F. Chen, 'Plasma diagnostic techniques' (Academic Press New York, 1965), Chapter 4.

C. D. Child, Phys. Rev. 32 (1911) 492.

S. Creasey, D. B. Lewis, I. J. Smith, W.-D. Münz, Surf. and Coat. Technol. 97 (1997) 163.

L. A. Donohue, D. B. Lewis, W.-D. Münz, M. M. Stack, S. B. Lyon, H.-W. Wang, D. Rafaja, Vacuum 55 (1999) 109.

D. Drouin, P. Hovington, R. Gauvin, Scanning 19 (1997) 20.

B. Enders, R. Emmerich, W. Ensinger, Surf. and Coat. Technol. 66 (1994) 478.

W. Ensinger, Surf. and Coat. Technol. 65 (1994) 90.

W. Ensinger, T. Hochbauer, B. Rauschenbach, Surf. and Coat. Technol. 94-95 (1997) 352.

W. Ensinger, T. Hochbauer, B. Rauschenbach, Surf. and Coat. Technol. 103-104 (1998) 218.

J. E. Greene, S. A. Barnett, J.-E. Sundgren, A. Rockett, 'Ion-beam assisted film growth' (edited by T. Itoh, Elseviere New York, 1988), Chapter 5.

C. R. M. Grovenor, H. T. G. Hentzell and D. A. Smith, Acta Metall. 32 (1984) 773.

G. Hakansson, J.-E. Sundgren, D. McIntyre, J. E. Greene, W.-D. Munz, Thin Solid Films 153(55) (1987) 79.

S. Hamaguchi, S. M. Rossnagel, J. Vac. Sci. Technol. B 14(4) (1996) 2603.

J. M. E. Harper, J. J. Cuomo, R. J. Gambino, H. R. Kaufman, 'Ion Bombardment Modification of Surfaces' (edited by O. Auciello and R. Kelly, Elsevier New York 1984), Chapter 4.

W. Hauffe, 'Production of Microstructures by Ion Beam Sputtering', in: Topics in Applied Physics Series - Volume 64 (Sputtering by particle bombardment III), edited by R. Behrish and K. Wittmaack (Springer-Verlag, 1991), Chapter 6.

U. Helmersson, J.-E. Sundgren, J. of Electron Microscopy Technique 4 (1986) 361.

U. Helmersson, S. Todorova, S. A. Barnett, J.-E. Sundgren, L. C. Markert, J. E. Greene, J. Appl. Phys. 62(2) (1987) 481.

P. Hovington, D. Drouin, R. Gauvin, Scanning 19 (1997) 1.

P. Hovington, D. Drouin, R. Gauvin, D. C. Joy, N. Evans, Scanning 19 (1997) 29.

T. C. Huang, G. Lim, F. Parmigiani, E. Kay, J. Vac. Sci. Technol. A 3 (1985) 2161.

Ch.-T. Huang, J.-G. Duh, Surf. and Coat. Technol. 71 (1995) 2259.

L. Hultman, S. A. Barnett, J.-E. Sundgren, J. E. Greene, J. of Crystal Growth 92 (1988) 639.

L. Hultman, W.-D. Münz, J. Musil, S. Kadlec, I. Petrov, J. E. Greene, J. Vac. Sci. Technol. A 9(3) (1991) 434.

L. Hultman, J.-E. Sundgren, J. E. Greene, D. B. Bergstrom, I. Petrov, J. Appl. Phys. 78(9) (1995) 5395.

J. D. Jackson, 'Classical electrodynamics' (3rd edition, New York, 1999), p.75.

H. A. Jehn, B. Rother, H. Kappl and G. Ebersbach, Surf. and Coat. Technol. 94-95 (1997) 232.

B. O. Johansson, J.-E. Sundgren, H. T. Hentzell and S.-E. Karlsson, Thin Solid Films 111 (1984) 313.

L. B. Jonsson, C. Hedlund, I. V. Katardjiev, S. Berg, Thin Solid Films 348 (1999) 227.

G. Keller, S. Mandl, U. Rude, B. Rauschenbach, Surf. and Coat. Technol. 136 (2001) 117.

D. J. Kester and R. Messier, J. Mater. Res. 8 (1993) 1938.

S. S. Kim, J. G. Hang and S. Y. Lee, Thin Solid Films 334 (1998) 133.

C. Klatt, B. Enders, G. K. Wolf, Surf. and Coat. Technol. 74-75 (1995) 966.

I. Kvasnicka, Z. Mala, R. Novak, D. Novakova, Surf. and Coat. Technol. 116-119 (1999) 634.

D. T. Kwok, P. K. Chu, B.P. Wood, C. Chang, J. Appl. Phys. 86(4) (1999) 1817.

I. Langmuir, Phys. Rev. 2 (1913) 450.

I. Langmuir, Phys. Rev. 28 (1926) 727.

M. A. Lieberman, A. J. Lichtenberg, 'Principles of Plasma Discharges and Materials Processing' (John Wiley and Sons, New York, 1994).

D.-F. Lii, J. of Materials Science 33 (1998) 2137.

R. Lindsay, J. N. Chapman, A. J. Craven, D. McBain, Ultramicroscopy 80 (1999) 41.

A. R. Messier, A P. Giri, R. A. Roy, J. Vac. Sci. Technol. A 2 (1984) 500.

A. R. Messier, J. Vac. Sci. Technol. A 4(3) (1986) 49.

B. A. Movchan, A V. Demchishin, Phys. Met. Metallogr. USSR 28 (1969) 83.

K.-H. Muller, J. Appl. Phys. 58 (1985) 2573.

K.-H. Muller, J. Appl. Phys. 59 (1986) 2803.

K.-H. Muller, J. Appl. Phys. 62 (1987) 1796.

W.-D. Münz, Surf. and Coat. Technol. 48 (1991) 81.

W.-D. Münz, D. Schulze, F. J. M. Hauzer, Surf. and Coat. Technol. 50 (1992), 192.

W.-D. Münz, L. A. Donohue, P. Eh. Hovsepian, Surf. and Coat. Technol. 125 (2000) 269.

W.-D. Münz - private communication (2003).

G. Nayal, D. B. Lewis, M. Lembke, W.-D. Münz, J. E. Cockrem, Surf. and Coat. Technol. 111 (1999) 148.

R. Novak, I. Kvasnicka, D. Novakova and Z. Mala, Surf. and Coat. Technol. 114 (1999) 65.

M. Paulus, L. Stals, U Rude, B. Rauschenbach, J. Appl. Phys. 85(2) (1999) 761.

I. Petrov, L. Hultman, J.-E. Sundgren, J. E. Greene, J. Vac. Sci. Technol. A 10(2) (1992) 265.

I. Petrov, F. Adibi, J. E. Greene, L. Hultman, J.-E. Sundgren, Appl. Phys. Lett. 63(1) (1993) 36.

I. Petrov, A. Myers, J. E. Greene, J. R. Abelson, J. Vac. Sci. Technol. A 12(5) (1994) 2846.

I. Petrov, P. Losbichler, D. Bergstrom, J. E. Greene, W.-D. Münz, T. Hurkmans, T. Trinh, Thin Solid Films 302 (1997) 179.

S. J. B. Reed, 'Electron Microprobe analysis' (Cambridge University Press, 1993), Chapters 12-17.

H. E. Roosendaal, 'Sputtering Yield of Single Crystalline Targets', in: Topics in Applied Physics series - Volume 47 (Sputtering by particle bombardment I), edited by R. Behrisch (Springer-Verlag, 1981), Chapter 5.

S. M. Rossnagel, J. Cuomo, Thin Solid Films 171 (1989) 143.

B. Rother, H. Kappl, I. Pfeifer-Schaller, G. Ebersbach, H. A. Jehn, Surf. and Coat. Technol. 97 (1997) 200.

Sandvik Coromant (publisher), 'Modern Metal Cutting - Practical Handbook' (Fairlawn New York, 1990).

Yu. P. Sharkeev, A. N. Didenko, E. V. Kozlov, Surf. and Coat. Technol. 65 (1994) 112.

C. Schonjahn, M. Bamford, L. A. Donohue, D. B. Lewis, S. Forder, W.-D. Münz, Surf. and Coat. Technol. 125 (2000) 66.

J.-E. Sundgren, B.-O. Johansson, S.-E. Karlsson, Thin Solid Films 105 (1983) 385.

J.-E. Sundgren, 'Diamond and Diamond-Like Films and Coatings' (edited by R. E. Clausing, Plenum Press, 1991), p.47.

J.-E. Sundgren, L. Hultman, 'Materials and Processes for Surface and Interface Engineering' (edited by Y. Pauleau, Kluwer Academic Publishers, 1995), p.453.

J. A. Thorton, J. Vac. Sci. Technol. 11 (1974) 666.

J. A. Thorton, J. Vac. Sci. Technol. A 4(6) (1986) 3059.

H. K.Tonshoff, A.Mohlfeld, T.Leyendecker, H.G.Fuss, G.Erkens, R.Wenke, T.Cselle, M.Schwenck, Surf. and Coat. Technol. 94-95 (1997), p. 603.

H. K. Tonshoff, B. Karpuschewski, A. Mohlfeld, H. Seegers, Thin Solid Films 332 (1998) 146.

V. Valvoda, A. J. Perry, L. Hultman, J. Musil, S. Kadlec, Surf. and Coat. Technol. 49 (1991) 181.

U. Wahlstrom, L. Hultman, J.-E. Sundgren, F. Adibi, I. Petrov, J. E. Greene, Thin Solid Films 235 (1993) 62.

P. A. Watterson, J. Phys. D 22 (1989) 1300.

D. B. Williams, C. B. Carter, 'Transmission Electron Microscopy' (Plenum Press, New York, 1996).

Z. M. Zeng, T. K. Kwok, X. B. Tian, B. Y. Tang, P. K. Chu, J. Appl. Phys. 86(1) (1999) 120.

Appendix: ZAF corrections analysis

This section presents ZAF analysis for Al and Ti $K\alpha_1$ radiations inside TiAl material. The corrections accounting for the absorption, stopping power, backscattering and fluorescence of the two radiations are calculated according to Reed (1993). The final correction factor is then used to find the relationship between the emitted X-ray intensities and the actual composition of the elements inside the material. The absorption correction for the radiation within the substrate material is also calculated.

a.) Absorption correction (A)

Since X-rays are generated below the surface of the sample, the emergent radiation suffers absorption prior to the detection. The absorption correction is a function of the angle between the sample and the detector (as this influences the length of path traversed by the radiation), the wavelength of the emergent X-ray, the elements present and the depth distribution of X-rays generation. There are several models describing this distribution. In our calculation we have used the simplest Philibert method. (There are other more sophisticated models, which give somewhat better results in cases of severe absorption and are thus preferable for light element analysis - for example rectilinear, gaussian or parabolic models - but in most cases, the results of calculations using different models do not differ greatly.) The absorption factor for samples examined by microprobe analysis, F_a, can be calculated using the Philibert equation, which accounts for the effects of the sample-detector angle, accelerating voltage, composition, etc.:

$$Fa = (1+\frac{\chi}{\sigma}) / [1+\frac{h}{(1+h)}(\frac{\chi}{\sigma})],$$

where χ is a function of mass attenuation coefficient μ and the angle of the detector φ:

$$\chi = \mu / \sin\varphi,$$

h is a function of the atomic weight A and the atomic number Z of the material:

$$h = 1.2(A / Z^2),$$

and σ is a function of the accelerating voltage of the electrons E_0 and the critical ionisation potential E_C:

$$\sigma = 4.5 \times 10^5 / (E_0^{1.65} - E_C^{1.65}) .$$

The mass attenuation coefficient μ is a measure of the material's power to absorb the X-rays. It is usually expressed in units of cm^2/g and is independent of the physical and chemical state of the absorber. Owing to the strong dependence of μ on atomic number of the material, the absorption suffered by characteristic radiation emerging from a sample in the electron microprobe is highly dependent on the composition. For quantitative analysis an absorption correction is therefore very important.

The mass attenuation coefficients for the Al and Ti radiation are (from table 15.2.in Reed, 1993):

μ_{Al} (in Al) = 398 μ_{Al} (in Ti) = 2200

μ_{Ti} (in Al) = 264 μ_{Ti} (in Ti) = 108

The coefficients for the two radiations in TiAl-alloy can be calculated using the mass concentrations of the elements (assuming 50% Al and 50% Ti alloy):

μ_{Al} (in TiAl) = (0.5 × 398) + (0.5 × 2200) ≈ 1300

μ_{Ti} (in TiAl) = (0.5 × 264) + (0.5 × 108) ≈ 180.

From these values, χ is obtained by multiplying by $1/\sin\psi$ (the take-off angle $\varphi = 40°$ in the standard position of the detector):

χ (for Al) = 2022

χ (for Ti) = 280.

The parameter h is calculated using the corresponding A and Z, the mean value for the alloy is calculated using the mass concentrations (50% Al and 50% Ti):

h (for Al) = 0.192

h (for Ti) = 0.119

h (for TiAl) = 0.115.

The parameter σ is a function of E_o and E_c (E_o = 20 keV in our case and E_c = 1.560 keV for Al and 4.964 keV for Ti):

σ (for Al) = 3258

σ (for Ti) = 3568

Which gives finally:

F_a (for Al radiation in TiAl) = (1 + 0.62)/(1 + 0.1335 × 0.62) = 1.496

F_a (for Ti radiation in TiAl) = (1 + 0.078)/(1 + 0.1335 × 0.078) = 1.067.

The comparison of the two absorption corrections:

F_a(for Al in TiAl)/F_a (for Ti in TiAl) = 1.4,

shows that the absorption of Al radiation inside TiAl is significantly higher when compared to Ti-radiation (by ~40%).

We have also calculated the absorption correction for $Ti_{0.5}Al_{0.5}$lN, in order to see how much it differs from the $Ti_{0.5}Al_{0.5}$ material. The same formulas were used, but now taking into account the mass absorption coefficients for Al and Ti radiation inside TiAlN:

μ_{Al} (in TiAlN) = 1101

μ_{Ti} (in TiAlN) = 42.

The equation x then gives:

F_a(for Al in TiAlN)/F_a (for Ti in TiAlN) = 1.5,

which is only 7% different from the value obtained for TiAl.

b.) Atomic number corrections (Z)

The atomic number effect controls the amount of incident energy from the electron beam that is actually put into the sample. This effect consists of two components: backscattering and electron-stopping power. Both are, to a reasonable approximation, a function of average Z and (to a lesser degree) the accelerating voltage.

Backscattering

Backscattered electrons leave the sample carrying energy without producing X-rays. The backscattering of electrons by solid targets is caused mainly by elastic scattering, in which incident electrons are deflected with negligible loss of energy. The deflection in this case exceeds 90°. Some electrons escape after experiencing single scattering event, more commonly however backscattered electrons suffer multiple deflections before emerging from the sample. Deflections associated with inelastic scattering are small. The fractional X-ray intensity loss due to electron backscattering η_x is defined as the

intensity loss divided by the total intensity that would be obtained with no backscattering. (In order to derive η_x it is necessary to calculate the X-ray intensity that the backscattered electrons would produce if they remained within the sample.) The backscattering correction factor F_b is given by:

$$F_b = 1/(1-\eta_x) = 1/R$$

The parameter R is a function of the atomic number of the material Z and of the ratio between the critical ionisation energy and the energy of the electron beam E_C/E_0 (denoted as parameter W_0); and can be determined experimentally. The values for Al and Ti radiation are (Table 14.1 in Reed, 1993):

R (for Al radiation in Al) = 0.920

R (for Al radiation in Ti) = 0.881

thus R (for Al radiation in TiAl) = (0.92 × 0.5) + (0.881 × 0.5) = 0.900

R (for Ti radiation in Al) = 0.935

R (for Ti radiation in Al) = 0.848

thus R (for Ti radiation in TiAl) = (0.935 × 0.5) + (0.848 × 0.5) = 0.891.

The backscattering correction factors F_b are then:

F_b (for Al radiation in TiAl) = 1/0.9 = 1.111

F_b (for Ti radiation in TiAl) = 1/0.891 = 1.122

The difference between the two radiations is small (about 1%).

Stopping power

The stopping power S relates the amount of incident energy to the amount absorbed by atoms of specific atomic number Z. Incident electrons lose energy through inelastic scattering, which includes various kinds of interaction with target atoms. The excitation of single atomic electrons gives rise to losses ranging from a few eV up to several keV. Large energy loss events, inner-shell ionisation or production of continuum X-rays, are infrequent. In most cases the number of inelastic collisions suffered by an incident electron having initial energy 20 keV is therefore large, and it is permissible to adopt the 'continuous slowing down approximation'. In this approximation, energy is assumed to be lost continuously and the stopping power can be obtained from the simplified form of Bethe's expression (denoted as Duncumb-Reed method):

$$F_S = (Z / A)\ln(1.166E / J),$$

where J is the mean ionisation potential and

$$E = (E_0 + E_C)/2.$$

For elements with atomic number Z between 10 and 25, the ionisation potential J can be to a good approximation calculated from very simple expression:

$$J = 11.5 \times Z.$$

First we calculate stopping power separately for each element:

S (Al in Al) = 13/27 × ln(1.166 × 10743/149.5) = 2.132

S (Al in Ti) = 22/48 × ln(1.166 × 10743/253) = 1.788

S (Ti in Al) = 13/27 × ln(1.166 × 12254/149.5) = 2.195

S (Ti in Ti) = 22/48 × ln(1.166 × 12254/253) = 1.849.

The stopping power correction corresponding to the alloy can be calculated using the mass concentration averaging (50% Al and 50% Ti):

S (for Al radiation in TiAl) = 1.960

S (for Ti radiation in TiAl) = 2.022.

The stopping power for the Ti radiation in TiAl is thus about 3% higher than that of Al-radiation in the same material.

c.) Fluorescence correction (F)

Fluorescence occurs when the characteristic radiation from an element A is excited by X-rays photons of energy higher than the critical excitation energy of A. Part of the continuous X-ray spectrum invariably satisfies this condition, hence 'continuum fluorescence' is always present. Fluorescence may also be excited by the characteristic radiation of other elements present in the material, if the energy criterion above is satisfied. This type of fluorescence is called 'characteristic fluorescence'.

Characteristic fluorescence

In order to apply a correction for characteristic fluorescence it is necessary to calculate the intensity of the fluorescence radiation of element A (I_f) excited by the characteristic

radiation of element B, and to obtain the ratio I_f/I_A, where I_A is the intensity of A radiation produced directly by electron bombardment. The fluorescence factor F_f is given by:

$$F_f = 1/[1+(I_f / I_A)]$$

In order to calculate I_f/I_A we have used the equation of Castaing (which refers to K-K fluorescence):

$$I_f / I_A = 0.5 c_B (\mu_B^A / \mu_B)[(r_A - 1)/r_A]\omega_K(B)(A_A / A_B)$$
$$\times[(U_B \ln U_B - U_B + 1)/(U_A \ln - U_A + 1)]$$
$$\times\{[\ln(1+u)]/u + [\ln(1+v)]/v\}$$

where: μ_B^A = mass attenuation coefficient for the absorption of B-radiation by pure A

μ_B = mass attenuation coefficient for the absorption of B-radiation by the sample $\omega_K(A)$ = the K-shell fluorescence yield of element B

r = 'the absorption edge jump ratio' (the mass attenuation coefficient on the high energy side of the K edge divided by that on the low energy side)

$U = E_0/E_C$

$u = \mu_A/(\mu_B \sin\psi)$

$v = \sigma/\mu_B$.

The parameter r can be calculated from the expression of Springer:

$$(r-1)/r = 0.924 - 0.00144 \times Z$$

The value of $\omega_K(A)$ is tabulated (Table A.6 in Reed, 1993) and σ is the same parameter as in the calculation of absorption correction. In the case of our AlTi alloy, the Al $K\alpha_1$ radiation can be excited by Ti $K\alpha_1$ radiation (the critical energy for Al $K\alpha_1$ radiation = 1.560 keV, the energy of Ti $K\alpha_1$ = 4.508 keV), but not vice-versa, hence a characteristic fluorescence correction is required only for Al. The correction can be calculated using the equations above with A = Al and B = Ti, which gives us:

μ_B^A = 264 (Ti in Al) , μ_A = 1300 (Al in TiAl), μ_B = 180 (Ti in TiAl)

$(r_A-1)/r_A = 0.924 - 0.00144 \times 13 = 0.905$

$\omega_K(Ti) = 0.214$ (table)

$A_{Al}/A_{Ti} = 27/48 = 0.562$

$U_A = 20/1.486 = 13.460$, $U_B = 20/4.508 = 4.436$

$u = 1300/(0.642 \times 180) = 11.24$, $v = 3254.7/180 = 18.08$.

Combining all this we obtain finally :

$I_f/I_A = 2.14e\text{-}3$, which gives:

F_{fl} (for Al in TiAl) = $1/(1 + 2.14e\text{-}3) = \underline{0.998}$.

The fluorescence correction for the X-ray intensity of Al is very small (~0.2%), which is related to the difference between the atomic numbers of Al and Ti (22-13 = 9). In general, the size of the K-K fluorescence correction decreases as the difference between the atomic numbers of A and B increases. For elements with Z < 20 the correction is always small.

Continuum fluorescence

Both Al and Ti $K\alpha_1$ X-rays can be also excited by the continuum radiation having energy between Ec and Eo. The fluorescence correction in this case can be calculated from:

$$I_f / I_A = D_A E_C[(\ln 1 + wU)/wU],$$

where:

$$D_A = 3.85 \times 10^{-6}[(r-1)/r]AZ \text{ , and}$$

$$w = \mu_A/(\mu_K \sin\psi).$$

The parameter μ_A is the mass absorption coefficient for $K\alpha_1$ radiation while μ_K is the mass absorption coefficient at the high-energy side of K absorption edge. (The corresponding values can be found in tables 15.2 and 16.1 in Reed, 1993.)

Let's consider Al radiation in Al and Ti radiation in Ti:

The ratio (r-1)/r can be calculated from Eq.x (previous section) which gives us:

D_A (Al in Al) = $3.85e\text{-}6 \times 0.0737 \times 26.98 \times 13 = 1.00e\text{-}4$

D_A (Ti in Ti) = $3.85e\text{-}6 \times 0.8923 \times 47.87 \times 22 = 3.62e\text{-}3$

w (Al in Al) = $398/(4276 \times 1.556) = 0.145$

w (Ti in Ti) = $108/(711 \times 1.556) = 0.236$

U_0 (for Al radiation) = 20/1.56 =12.820, U_0 (for Ti radiation) = 20/4.964 = 4.029

I_f/I_A (for Al radiation in Al) = 1.0e-4 × 1.560 × ln(1 + 0.145×12.820)/(0.145×12.82) = 8.8e-5

I_f/I_A (for Ti radiation in Ti) = 3.62e-3 × 4.964 × ln(1 + 0.236×4.029)/(0.236×4.029) = 0.013

We have checked that to a very good approximation these factors are similar to the corrections inside TiAl alloy (I_f/I_A (for Al in TiAl) = 8.1e-5, and I_f/I_A (for Ti in TiAl) = 0.011). These calculations are much more complicated as they include into consideration the effect of the absorption edges but because of the very small change are not shown here. The correction factors for the two radiation inside TiAl are then:

F_{f2} (Al in TiAl) ~ 1/(1 + 8.8e-5) = 1.000

F_{f2} (Ti in TiAl) ~ 1/(1 + 0.013) = 0.989

F_{f2} (Al)/ F_{f2} (Ti)= 1.011

d.) Total correction factor

The total correction factor F is the product of the individual factors derived above.

Fal = 1.496 × 1.111 × 1.961 × 0.998 × 1 = 3.253

Fti = 1.068 × 1.122 × 2.023 × 1 × 0.989 = 2.397

Fal/Fti = 1.357, Fti/Fal = 0.737

e.) The absorption correction for the substrate

The absorption of Al and Ti radiation when traversing the substrate material, was calculated using the same method as above but now taking Fe (≈ substrate) instead of TiAl. The corresponding mass absorption coefficients are:

μ (Al in Fe) = 3626

μ (Ti in Fe) = 188.

These values can be used to calculate the parameter χ. The values of σ are the same before, while the parameter h (calculated using the atomic number and atomic mass of Fe) is now:

h = 1.2 × (55.845/262) = 0.099.

The calculation gives us finally:

F_a (for Al radiation in Fe) = 2.362

F_a (for Ti radiation in Fe) = 1.074

$F_a(Al)/F_a(Ti)$ = 2.200,

which means that the absorption of Al radiation within the substrate material is more than 2-times higher than that of Ti radiation.